Master thesis
Marine Technology - Ship Hydromechanics

TU Delft, 3mE

Research report

The influence of dynamic flow behaviour on T-foils

Yves de Block

Delft University of Technology

January 11, 2023

Student number:	4342003
Supervisors:	Ido Akkerman
	Alex Ashworth Briggs
Graduation committee:	Ido Akkerman
	Alex Ashworth Briggs
	Daniele Fiscaletti

Thesis for the degree of MSc in Marine Technology in the specialisation of Ship Hydromechanics

The influence of dynamic flow behaviour on T-foils

By

Yves de Block

Performed at

TU Delft

This thesis MT.22/27.017.M is classified as confidential in accordance with the general conditions for projects performed by the TUDelft.

January 11, 2027

Supervisors
Responsible supervisor: Ido Akkerman

Daily Supervisor(s): Ido Akkerman, Alex Ashworth Briggs
E

Thesis exam committee
Chair/Responsible Professor: Ido Akkerman
Staff Member: Alex Ashworth Briggs
Staff Member: Daniele Fiscaletti

Author Details
Studynumber: 4742007

Preface

This study comprises, not only a way to fulfil the graduation requirements of Maritime Engineering at the Technical University of Delft, but most of all, from my perspective as a moth sailor, it has been a journey to learn more about hydrofoils.

My friend Iain Jensen, who finished second at the 2021 Moth Worlds, agrees that sailing in flat water is very different from sailing in choppy conditions. The demand for innovation of the control system for T-foil is what inspired me for this research. Combining the knowledge acquired in this study and my experience in composite technology, I want to contribute to the next step in the professional sailing sports industry.

This research broadened my knowledge of towing tank research, both in ways how to and how not to. I am used to Matlab but for this research, I broadened my coding skill set with Python. I made an extensive effort to improve my academic writing skills. It taught me patience and to listen carefully before acting.

I would not have learned these lessons without my two supervisors. Ido Akkerman provided me with challenges, maximising the learning opportunity with enriching questions as well as his Python expertise. Alex Ashworth Briggs, my non-European supervisor, shares my passion for sailing and hydrofoiling. He shared his profound experience in towing tank research, while keeping the practical application on course. Alex was always there to listen and motivated me to strive for excellence. I am grateful for both my supervisors; they have taught me valuable lessons, both professionally and personally.

Not least of all, I want to thank my family and friends for their patience and motivation to persevere. I would also wish you, my reader, joy on this inquisitive journey into the learning process of foil behaviour in dynamic conditions. I hope you may learn as much as I did.

Yves de Block

Lisse, January 11, 2023

Abstract

This research thesis focuses on conducting experimental research into the hydrodynamic properties of a NACA 0012 T-foil in dynamic conditions. An aerodynamically smooth surface was created and used for all dynamic experiments. For exploratory research into the effect of surface finish on the performance of a T-foil in steady state conditions, a second, unfinished but structurally equal, T-foil was made using .15 *mm* 3D printing layers aligned with the flow.

The hydrodynamic properties were determined by conducting experiments in steady state conditions using conventional towing tank methods. Combining all steady state experiments, the lift and drag coefficient on the foil are expressed as a function of angle of attack, freestream velocity and submergence for a Reynolds number of $1.5 \cdot 10^5$. The surface finish of the second, raw printed, T-foil resulted in a lower critical Reynolds number of $3.3 \cdot 10^5$ compared to $4.5 \cdot 10^5$ for the aerodynamically smooth foil.

Dynamic flow conditions were simulated in experiments where the setup was subjected to either: sinusoidal pitch motion, sinusoidal heaving motion or waves. As a result of the imposed motions, the static forces on the setup change and inertial forces occur. To compensate for this, a function was made from all static measurements. The inertial forces are compensated by applying a mass/inertia matrix.

Using this new method of towing tank research, the steady state behaviour of a T-foil is described using dynamic experiments. The novel method to determine steady state characteristics includes two angle sweeps, one positive and one negative. The rate of change proves to be sufficiently slow at $0.8\ ^\circ\ s^{-1}$ for $v_\infty = 2\ ms^{-1}$, producing more accurate results while towing tank time can be reduced by 78%.

From the steady state results a model is created. Because this model is limited to $Re = 1.5 \cdot 10^5$, it is enriched with a prediction model based on X-foil which is compensated for induced drag, finite foil shape and free surface effects.

The prediction shows good correlation with the results in z-direction for both imposed sinusoidal heaving and pitching motions. During sinusoidal heaving, flow remains attached longer leading to higher and more stable lift and drag at higher absolute angles. In pitching a similar effect can be seen leading to increased fluctuations and slightly higher average lift compared to the prediction models. For both imposed motions, lower drag is measured with respect to both the predictions and the measurement in steady state conditions. An additional component to the drag occurs during a sinusoidal pitching motion. This additional component has a sinusoidal behaviour equal to the imposed motion which suggests that it is caused by induced drag.

When the freestream velocity was increased from 2 to 6 ms^{-1} in similar waves, it was found that the sinusoidal response of the hydrodynamic forces shifted by $\pm\ \pi\ rad$. Similar to the imposed dynamic motions, predictions show larger values for drag. It was found that the wave height can be related to the drag. When wave height is increased, the drag is reduced.

Contents

Nomenclature

Symbol	Description	Unity
a	acceleration	ms^{-2}
A_{foil}	relevant surface area of the foil	m^2
$A_{horizontal}$	relevant surface area of the horizontal part of the foil	m^2
$A_{vertical}$	relevant surface area of the vertical part foil	m^2
AR	aspect ratio	$-$
c	speed of sound in the medium	ms^{-1}
c	chord length	m
c_m	mean chord length	m
c_r	chord length at the root	m
c_t	chord length at the tip of the horizontal	m
$c_{vertical}$	chord length of the vertical	m
C_L	lift coefficient finite wingspan	$-$
C_l	lift coefficient infinite wingspan	$-$
C_{l0}	section lift coefficient for AoA = 0	$-$
C_D	drag coefficient	$-$
C_{D_i}	induced drag coefficient	$-$
D	drag force	N
e	Oswald efficiency factor	$-$
EI	flexual rigidity	Nm^2
F	force	N
$F_{dynamic}$	dynamic force	N
$F_{stationary}$	stationary force	N
F_{total}	force acting on the setup	N
Fn	Froude number	$-$
g	gravitational acceleration	ms^{-2}
h	submergence	m
I	inertia	kgm^2
k	wave number	m^{-1}
l	characteristic linear dimension	m
L	lift force	N

Symbol	Description	Unity
m	mass	kg
M	Mach number	$-$
M	moment	Nm
N_{crit}	boundary layer transition point	$-$
p	static pressure	Nm^{-2}
p_∞	static pressure in the freestream	Nm^{-2}
r	lever length	m
Re	Reynolds number	$-$
s	wing span	m
t	time	s
$t_{vertical}$	width of the strut	mm
u	flow velocity	ms^{-1}
v_f	stream velocity at foil	ms^{-1}
$v_{induced}$	induced motion due to movement of vertical	ms^{-1}
$v_\infty = v_{inf}$	freestream velocity	ms^{-1}
Whm	wave height measurement	mm
α	angle of attack (AoA)	$^\circ$
ζ	wave height	m
ζ_a	wave amplitude	m
λ	wave length	m
ν	kinematic viscosity of the medium	m^2s^{-1}
ϕ	wave potential	m^2s^{-1}
ρ	density	kgm^{-3}
ϕ	phase shift	rad
ω	angular velocity	$rads^{-1}$

1 Introduction

Since the beginning of the 20^{th} century, scientists have explored the concept of hydrofoiling. This concept entails the rising of a vessel by a foil shaped body in order to reduce drag otherwise created by wetted surface area and wave resistance. The modern potential of hydrofoils is demonstrated in the America's Cup where 2 similar boat race each other (figure 1.1). Once these boats are foiling, the resistance is dramatically reduced, allowing seventy-five feet or 22.86 m long hydrofoiling monohulls, weighing almost six tons, to race at over three times the true wind speed. Many innovations, including the hydrofoils and their control systems, have led to these spectacular performances. The potential for this technology is immense, in the shipping industry for example, hydrofoiling could lead to reduced shipping times and less fuel consumption. Yet, the level of hydrofoiling activated in the America's Cup is to be developed to a stage where it can be applied to the marine industry. Looking at the challenges, the potential and the supporting literature, a gap emerges. This study contributes to the innovation of hydrofoils by describing the properties of a T-foil in dynamic conditions.

Figure 1.1: Team New Zealand in America's Cup 2021 (Borlenghi, 2020)

1.1 The principle and evolution of hydrofoiling

Conventional vessels float due to their buoyancy. However, other methods are available and can be described by the lift triangle (Stapersma et al., 2000). According this theory, one of the following forces should be present to prevent a structure from sinking: static forces such as buoyancy, powered static lift and/or dynamic forces. Hydrofoiling is an increasingly popular example where a dynamic force due to lift and drag, lifts a body out of the water. Based upon this theory, hulls with appendages in the shape of hydrofoils were designed. The hull guarantees buoyancy when the vessel is sailing at low speed while at higher velocity, the hydrofoils create an upwards force referred to as lift. This force rises the vessel out of the water reducing the drag due to wave making resistance and wetted surface area (Von Karman & Gabrielli, 1950).

Literature distinguishes between two conditions in which a hydrofoil is operated, namely steady state and dynamic. In steady state conditions freestream velocity, depth and or angle of attack remain constant. In dynamic conditions the foil is subjected to changing flow conditions. In reality, hydrofoils are always subjected to dynamic conditions due to waves. The degree of the dynamic condition varies with the size and period of the waves in which the vessel is operated.

1.2 Two concepts: surface piercing versus fully submerged

Scientists have investigated the idea of adding hydrofoils to conventional displacement ships since the 19^{th} century (Acosta, 1973). Starting in 1908, Bell & Baldwin were pioneering researchers to develop a powered hydrofoil vessel. With their fourth model in 1919, they reported an 'on water' speed of 60 knots (Neilson Bonikowsky, 2009).

After Bell & Baldwin, the development of hydrofoils accelerated. Many theories were developed, all of which needed to meet the following criteria stated by W.A. Graig in response to "Canadian Advances in Surface-Piercing Hydrofoils": *"Hydrofoil craft are distinguished by the method they use to maintain the vertical component of their lift force at equilibrium with their weight, without allowing draft to fluctuate beyond narrow permissible limits. The method also insures longitudinal stabilisation, since otherwise the lift could not be controlled"* (Graig, 1974). In order to meet this criteria the lift of the hydrofoils must be controlled. This is achieved by either varying the lifting area, changing the shape and/or changing the angle of attack (AoA) of the foils. Over the past century, two concepts meeting this requirement were developed. The two concepts can be distinguished based on their working principles.

The first concept is a surface piercing foil. As the speed of the vessel increases, the lift increases. Due to the increased lift, the vessel rises out of the water. The foils are designed in such a way, that when the vessel rises, the part of the foil providing lift reduces. As a result, the overall lift remains constant and the ride height becomes directly related to the velocity of the vessel. Two examples of surface piercing foils are given in figure 1.2.

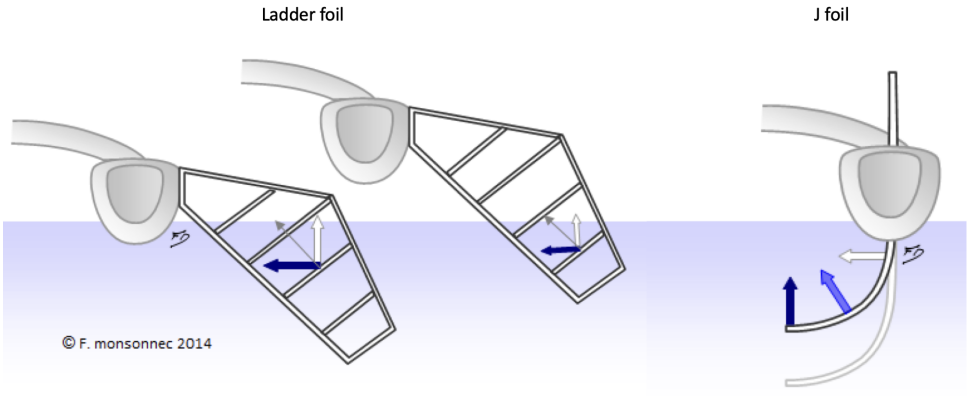

Figure 1.2: Foil Types (Monsonnec, 2014)

The left example of a surface piercing foil presented in figure 1.2, also referred to as stepwise foil, is the Ladder-foil developed by Bell & Baldwin (Acker, 1999). It is based on the same working principle as J-foils, the second and right example in figure 1.2. A disadvantage of the 'surface piercing' concept is that, when compared to the second concept, these surface piercing hydrofoils have a higher resistance. For J-foils, the increased resistance is a result of a thicker foil shape, enabling a broader range of angle of attack. For a Ladder-foil, the resistance is higher due to the presence of multiple lifting interfaces between the verticals. Another disadvantage of these surface piercing foils is that ventilation occurs quicker due to the pressurised interface piercing the surface. The self-controlling behaviour, where an equilibrium between ride height and velocity is maintained and thus no active control system is required, is the advantage of these foils. To change ride height, the setting of the pitch is changed. Examples where surface piercing foils are used include catamarans, commercial vessels and monohull sailing classes such as the Imoca60. In the Imoca60, foils are used for semi-foiling purposes. Here, the foils increase righting moment and reduce the displacement and wetted surface area. For these boats it leads to higher speed and a more pitch stable behaviour in waves, which increases both safety and comfort.

The second concept is a fully submerged T-foil which consists of a vertical strut and a horizontal lifting surface. For zero heel, the foil's vertical (the term used to refer to the vertical component of the foil), functions as a strut and daggerboard to prevent the boat from moving sideways. The horizontal provides a dynamic force to lift the vessel out of the water. In contradiction to other foils the lift of a T-foil is not related to the draught of the foil but to the shape, velocity and angle of attack ($h/c > 3$). Therefore T-foils require an active control system which is either a mechanical system or a computer provided with sensor data. The control system actively changes the angle of attack and/or shape of the foil. Typically, this is achieved by changing the orientation of a flap on the trailing edge of the horizontal. The active control system is both an advantage and a disadvantage of the T-foils. With an active control system a wider range in lift can be achieved. Also the drag is less than the first 'surface piercing' concept. The disadvantage is that it is a more delicate system and therefore only used for high performance applications, such as Moth sailing and the latest America's Cup (AC75). In figure 1.3, the working principle of a T-foil its control system is explained.

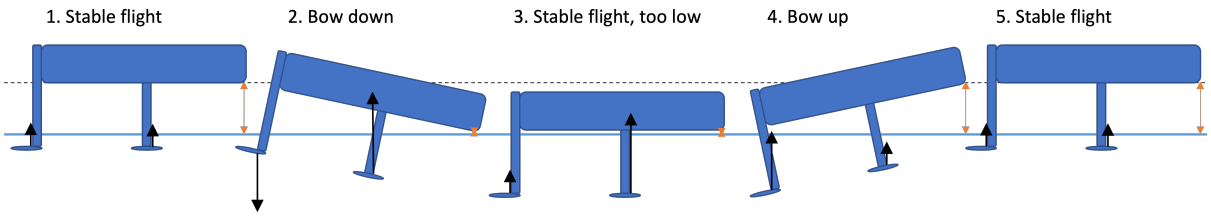

Figure 1.3: Pitch control

Starting with a stable flight (step 1) the boat is subjected to a disturbance which makes the bow go down. In step 2, the control system which is located at the bow of the vessel, responds with positive lift on the front T-foil. Due to the boat being now bow down, the rudder foil is subjected to a negative angle of attack resulting in a lift pointing downwards which leads to zero pitch depicted in step 3. The lift by the main foil is still high because the boat is still flying low. In step 4, the response is shown by the bow going up, giving the rudder increased angle of attack and thus lift. Due to the upwards lift on the rudder, a pitch equilibrium and a stable flight is achieved in step 5.

When it comes to the control system, which for T-foils in particular is very important, innovations can be made. This is highlighted by Iain Jennsen, who finished second in the Moth Worlds 2021 and noted that the limitations of the Moth's wand make it difficult to achieve stable flight in dynamic conditions. The wand is the device at the bow which measures the distance to the water. The wand is connected to the flap of the main foil through a set of systems that can be set to change the behaviour of the control system. On flat water the lever connecting the wand to the flap of the main foil is shortened which leads to an increased flap response and thus more flap movement. Flap movement may lead to additional resistance, but the added drag of the vertical in the water is much higher than having less flap response at lower ride heights. The flap response is considered essential to keep the foil as close to, but below the surface. In choppy conditions however, the settings are based on safety rather than reduced drag. If you can keep the hull out of the water and maintain a stable pitch, speed is increased with the ride height. Finding the highest yet safe height is difficult due to the limited capabilities of the

Moth's wand. This applies in particular for wave lengths which are equal to the distance from the front foil to the wand. The wand is then responding to the trough of the wave when the foil is at the top of the wave and vice versa. A better understanding of the forces in dynamic conditions may enable the development of an improved control system that can cope with incoming waves by predicting the response to the wave and compensating for the distance between the measurement and foil position.

1.3 Research into hydrofoils

This section gives an investigative overview of present-day research into the phenomena that influence the performance of hydrofoils. It concludes by highlighting the gap in existing literature and how this study contributes to and fits within, current state-of-the-art research.

The phenomenon of shape has been the focus of many studies. The aerodynamics of four distinct geometric flapping wing planforms (rectangular, Zimmerman, inverse Zimmerman and elliptical) with seven aspect ratios varying from 0.50 to 2.00 at various Reynolds numbers were examined and used for a genetic algorithm optimisation program (Mueller & Torres, 2004). The flexibility of a foil may affect the formation of leading edge vortex, trailing edge vortex and tip vortex and has been frequently considered in both spanwise (Cleaver et al., 2016) and chordwise (Dewey et al., 2013) directions. Other properties that influence the dynamic performance of a foil include the chord length (Alben et al., 2012), thickness (Wang et al., 2016) and camber (J.W. Chang & Yoon, 2015).

Spray is a form of drag where energy is dissipated in the deformation of the water. It occurs when a moving foil rises water at the back of the foil, causing it to deviate from the surface. An example is of this can be seen in figure 3.11. Attempts were made to harness the energy lost in the creation of spray by adding fences. However, the influence of spray on lift was proven to be insignificant (Binns et al., 2008).

Another factor that influences the performance of a foil is surface finish. The research into surface finish is limited and requires attention because the consensus in the Moth class is that surface finish of hydrofoils makes a significant difference, certainly on the field of ventilation. For example, the direction and grid of sanding are altered depending on the water temperature. Also, any sort of grease on the surface of hydrofoils must be prevented at all times.

A T-foil is operated in an incompressible medium. For high submergence, the flow conditions are limited to the medium itself. When foils are operated close to the surface with depth to chord ratio smaller than 2.5 ($h/c < 2.5$), surface proximity effects start to act. The incompressible medium around the foil can be deformed changing the shape of the surface. This results in decreased efficiency of the foil. Kenneth L. Wadlin tested two rectangular T-foils (NACA 66-012 and a NACA 64-A412) where the velocity varied between 4.6 ms^{-1} and 10.6 ms^{-1}, angle of attack between 0° and 3° and h/c between 0.44 and 5. Wadlin found that the lift over drag ratio decreased with the submergence of the foil. He also found that the value of C_L at which the highest ratio of L/D is found increases with the submergence of the foil (K. L. Wadlin et al., 1950). The influence of surface proximity is also investigated for heel. At a h/c ratio of 3.3, no change in efficiency is measured when the heel angle of foil is changed between 0° and 30°, however surface proximity effects are noted when the tip vortex starts interacting with the surface (Binns et al., 2008).

Wadlin published a second paper in which he researched the waves by the bound vortex of the hydrofoil. Wadlin compared the effect of sub-critical speeds ($v < \sqrt{gh}$) with super critical speeds ($v > \sqrt{gh}$). Above this transition velocity, transverse waves no longer accompany the foil. Theory predicted an abrupt increase of drag, however tank experiments showed a gradual increase in drag as the critical speed is approached from the super critical range (K. Wadlin et al., 1952).

The research by Binns was continued by A. Briggs, who investigated the mechanisms surrounding the inception of the tip vortex ventilation of T-foils. Particle Image Velocimetry (PIV) was used in the experimental research into the free surface effects of T-foils in the towing tank of the University of Tasmania. Apart from the effect of the endcap on the hydrodynamic properties, indications of high risk regions in the tip wake of a T-foil were found (Ashworth Briggs et al., 2018).

Ventilation is the occurrence of an air sheet on the foil which leads to a change in hydrodynamic performance. This expresses itself in an abrupt loss of lift which is destructive for a boat's sailability. Ventilation is caused when air is sucked onto the low pressure side of the foil via, for example the strut of the foil. Therefore,

the probability of this occurrence increases when the foil is operated closer to the surface. Another phenomena with similar behaviour is cavitation which occurs at high speed when the pressure drops below the vapour pressure. Yin Lu Young extended a 3D boundary element method to model effects of cavitation, ventilation and their hydrodynamic response. He found that cavitation and ventilation behaviour depend on angle of attack, submergence, relative inflow velocity, the difference between the absolute ambient and vapour pressure and hysteresis effects. Yin Lu Young distinguishes three stages of flow separation: Fully Attached, Transitional and Fully Ventilated (Young et al., 2013). The behaviour of the foil differs in these three stages.

Harmonically oscillating foils were tested for wave energy harvesting. The tests were performed using digital PIV at Reynolds numbers between 1100 and 40000. The experiments were compared to analytical and numerical non-viscous theory. During the experiments the foil was subjected to both pitch and heave. PIV experiments show that high efficiency of the propulsive system is accompanied with the generation of moderately strong leading edge vortices, which subsequently amalgamate with trailing-edge vorticity leading to the formation of a reverse Karman street (Anderson et al., 1998). This supports the theory that hysteresis effects, thus a phase shift and amplitude difference, occur at pitching and heaving motion. It has not been tested at higher Reynolds numbers, nor has it been tested for a T-foil.

Table 1.1 sketches an overview of the present day research.

Research	Condition	Reynolds number	Surface effect	Foil
Binns	steady state	$4.6 \cdot 10^5$	for heel angles	NACA 0012
Wadlin	steady state	$0.18 \cdot 10^6 - 1.64 \cdot 10^6$	yes	NACA 66-012 & NACA 64-A412
Briggs	steady state	$2.4 \cdot 10^5 - 1.4 \cdot 10^6$	yes	NACA 0012
Anderson	Oscillating heave and pitch	$1100 - 40000$	no	NACA 0012
This research	steady state and dynamic	$1.5 \cdot 10^5 - 4.6 \cdot 10^5$	yes	NACA 0012

Table 1.1: Comparison of similar research

In a review paper of foils in dynamic conditions Wu stated: *"Due to the complexities of three-dimensional flow, the studies of foils are still focused on two-dimensional structures at low or moderate Reynolds number. This has been far from the real applications, where the effects of three-dimensionality, freestream turbulence and high Reynolds numbers should be considered. The foil always has limited aspect ratio so its flow mechanism could be more complex and its end effect may influence the performance of propulsion and energy extraction. Therefore, a focus should be put on the study of flow characteristics of three-dimensional oscillating foils and the simulations based on real environment parameters in future."* (Wu et al., 2020). It can be concluded that research into the effects of dynamic behaviour on the application of lifting surfaces for energy harvesting has been initiated, however it is far from conclusive. As Wu stated, there is a need for further study into three dimensional oscillating foils. From others' research it can be concluded that a phase shift and modulus change can be expected according to Von Karman theory. However, no experimental results substantiate this expectation.

1.4 Goals and objective

This research will conduct experimental research into the hydrodynamic properties of a foil in dynamic conditions. To define the hydrodynamic properties, experiments in steady state conditions will be performed. In steady state conditions the foil remains in a stationary position. Combining all steady state experiments, the lift and drag on the foil are expressed as a function of angle of attack, velocity and submergence. For dynamic conditions, which are simulated in a non stationary or wave experiments, it is expected that the motion of the foil adds an additional component to lift and drag, due to hysteresis effects of the vortices. Using the function of the steady state experiments the difference between dynamic and steady state conditions will be described. This investigation will inform an improved representation of the properties of a hydrofoil, which in turn can form the basis for a predictive control system for a T-foil in waves. The prospective control system will use the wave pattern as an input to calculate the expected velocity and angle of attack in the wave. The expected velocity and angle of attack will then be used to calculate the force in z-direction using, not only the conventional hydrodynamic representation of a foil, but also the dynamic influences. The objective is to provide the foundation to establish an improved version of T-foil control systems that will enable a constant force in z-direction.

This research is motivated by the fact that the ability to establish a constant force in z-direction on working hydrofoils will have a positive impact on the use of hydrofoils in the marine transport industries. Establishing constant lift will lead to increased passenger comfort onboard hydrofoiling transport vessels. Additionally, drag will be reduced by reducing flap motions. This will presumably lead to a small increase in fuel efficiency. Such improvements will facilitate a more extensive application of hydrofoiling in the short to medium distance passenger transport. Ultimately, if alternatives in the marine sector arise, which are proven to be more fuel efficient than the present options for high speed transport, the ecological footprint of humanity can be reduced without limiting its desires.

1.5 Research questions

The research question of the thesis is:

How does the performance of a T-foil in steady state conditions compare to the performance of the same T-foil in dynamic conditions?

The different approaches to characterise a foil in steady state conditions require reflection in the research. As well as the exploratory research into the surface finish. All together, the following list of sub-questions arises:

- How does the behaviour of a T-foil in waves compare to the performance in steady state conditions?
- How does the behaviour of a T-foil in sinusoidal heave compare to the performance in steady state conditions?
- How does the behaviour of a T-foil in sinusoidal pitch compare to the performance in steady state conditions?
- Can the conventional towing tank procedure used to characterise a T-foil be simplified by applying a dynamic approach?
    - Can the conventional towing tank procedure be used to characterise a T-foil be simplified by a stepwise angle sweep?
    - Can the conventional towing tank procedure be used to characterise a T-foil be simplified by an angle sweep?
- How does the performance of a RAW 3D printed foil compare to an aerodynamically smooth and flat surface?

1.6 Plan of approach

To achieve the research goals, experiments will be conducted in the Towing Tank at TU Delft. A prediction of the hydrodynamic forces will be made using the mathematical software X-foil compensated for 3D effects. A test matrix will be made prior to the towing tank research. This matrix will be used as a guideline during the tests and as a tool to define and specify the test equipment.

For the experimental research to be a reliable representation of the hydrodynamic behaviour in steady state conditions, a standard methodology will be applied. The experimental setup will be calibrated component wise and a zero run will be made before starting an experiment. No changes will be made to the setup for the duration of the experiment. The average of the resulting force will then be subtracted by the zero run. To validate the experimental setup, the results will be compared with other publications. This emphasises the importance of the foil choice; results can be compared to other studies using the NACA 0012 foil.

Although the influence of surface finish is not the main focus of this study, some exploratory research into the steady state performance of a RAW 3D printed versus an aerodynamically smooth and flat surface will be conducted.

This research in the towing tank at the TU in Delft will be innovative in that the orientation of the foil will be changed during a run. The depth and pitch will also be changed. This raises questions about the applicability of conventional towing tank procedures because, where only hydrodynamic forces are desired, the buoyancy

and gravitational forces change. Therefore, new towing tank procedures will need to be explored and optimised. One of the questions that arises is, whether a different method of characterising a foil in steady state conditions can be used. There are two propositions for this method. The first is a stepwise angle sweep, the second is a continuous angle sweep.

For the experimental research in dynamic conditions a different approach is required whereby the orientation of the setup changes during the test. This leads to a change static force which contains buoyancy and gravity of the setup beow the load gauge. Also, due to the accelerations in the setup, inertial forces occur. To find the actual hydrodynamic forces, the measured signal must be compensated for static and inertial forces. The setup is subjected to heave and pitch in order to map hysteresis effects that may occur when operating a foil in dynamic conditions. To compare the dynamic results with the steady state results, a model of all the steady state results will be made. This model will be plotted in conjunction with the results in dynamic conditions to find correlation, differences and to draw conclusions regarding the influence of dynamic behaviour. Finally, the setup will be subjected to waves in the negative x-direction. The experiments in waves will be compared with the steady state prediction model to value the differences.

1.7 Novel aspects

Through experiments in the towing tank at TU Delft, the behaviour of a T-foil in dynamic conditions will be compared to the behaviour in steady state conditions. Wu et. al. made an observation in their review on available research about the need for research *"into flow characteristics of three-dimensional oscillating foils and real environment parameters"* (Wu et al., 2020). This study will add to the literature by describing the properties of a T-foil in waves instead of flat water, approaching the true environmental parameters by implementing innovative towing tank research.

1.8 Reading guide

Following this introduction, the used mathematical methods are discussed in chapter 2, where the theoretical background and an initial calculation of the influence of waves on foils is detailed. The experimental setup is described in chapter 3. This includes the choice and description of the T-foils used in this research and a force prediction. Furthermore, the design of the experimental setup is explained. To conclude, the script for the experiments is provided. Chapter 4 includes preliminary calculations and data preparations. Chapter 5 follows with analyses of steady state conditions. The foil characterisation is given and compared with the prediction and other research. The chapter concludes with an interpolation function of the hydrodynamic coefficients in steady state conditions. Using the calculation method made for the dynamic measurements, new methods to characterise a T-foil are discussed in chapter 6. In chapter 7, the behaviour due to an oscillating movement is compared to the behaviour in steady state conditions. The same is done for waves in chapter 8. The conclusion, limitations and recommendations of the research can be found in chapter 9.

2 Theoretical background

This chapter elaborates on the theories applied within the research. To start, an explanation of theory concerning coefficients such as Reynolds number, hydrodynamic coefficients, Froude number and Mach number is given. Afterwards, the most common calculation method to calculate the lift and drag coefficient for a wing is discussed. This method includes thin airfoil theory, lifting line theory, compensation for finite wingspan, compensation for free surface effects and compensation for T-joint interference. Next, Theodorsen's model which introduces a way to calculate the change in performance in dynamic conditions is given. This is followed by a discussion potential flow theory which is used to define particle velocity and direction in waves, which is required for calculating the angle of attack velocity at the foil. A discussion of two methods to filter the signal is presented in which an attempt is made to explain the equations and provide a better understanding. The theoretical background is concluded with definitions of common laws and methods. Newton's laws and an outline of the theory used to make surface fits of the measurements are also discussed.

2.1 Dimensionless numbers for boundary conditions and scaling

In this section four dimensionless numbers used for boundary conditions and scaling are introduced.

2.1.1 Reynolds number

The dimensionless Reynolds number provides an indication of the level of turbulence and is therefore a valuable unit in fluid mechanics. For many applications, such as X-foil, it is used for scaling. X-foil is a numerical program which will be used in section 3.1.1 to make a prediction of the hydrodynamic forces by the hydrofoil.

The concept named after Osborne Reynolds was found by George Stokes and can be calculated as follows (Stokes, 1851).

$$Re = \frac{v_\infty \, c_m}{\nu} \tag{2.1}$$

In which v_∞ is the freestream velocity, c_m the mean chord length and ν the kinematic viscosity of the medium.

The level of turbulence influences the hydrodynamic performance of a foil. Figure 2.1 emphasises the influence on the lift and drag coefficient of a NACA 0012 section at an angle of attack of 4 $^\circ$. A considerable reduction in drag is noted up to $Re \pm 2 \cdot 10^5$. Lift in contradiction reduces almost linearly. Physically this is the point where flow becomes turbulent and is therefore referred to as the critical Reynolds number. The point where flow becomes turbulent is different for different geometries and is not yet fully understood.

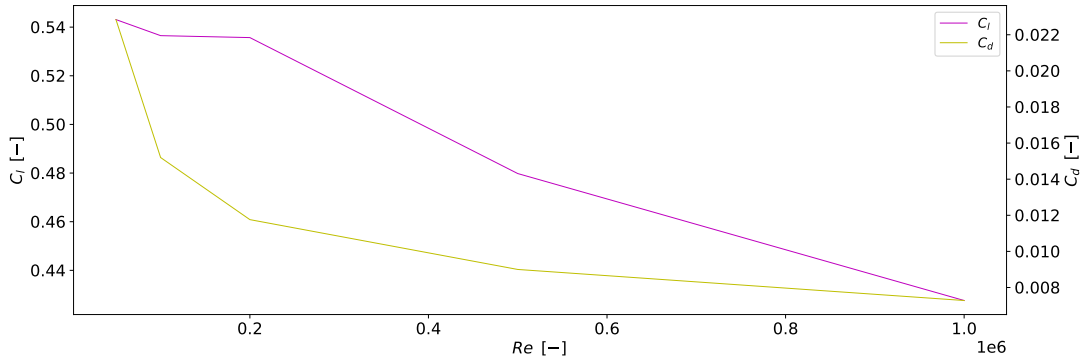

Figure 2.1: The influence of Reynolds number on the lift and drag coefficient of a NACA 0012 section at: $AoA = 4\,^{\circ}$

2.1.2 Hydrodynamic coefficients

The hydrodynamic forces are made dimensionless to compare foils of different shape. The following equations are used to calculate the coefficients of lift and drag.

$$C_L = \frac{2\,L}{{v_\infty}^2\,\rho\,A_{foil}} \tag{2.2}$$

$$C_D = \frac{2\,D}{{v_\infty}^2\,\rho\,A_{foil}} \tag{2.3}$$

In which L is the lift, D the drag, v_{inf} the freestream velocity, ρ the fluid density, A_{foil} the relevant area of the foil. The coefficients remain dependent on the shape, angle of attack and flow conditions after non-dimensionalisation of the lift and drag. It requires attention, as even though the force is divided by the velocity squared, the flow condition, which can be described by the Reynolds number, remains dependent on the velocity (equation 2.1). The influence of the Reynolds number on the hydrodynamic coefficients is emphasised and discussed in section 2.1.1 and figure 2.1.

2.1.3 Froude number

The Froude number (Fn) describes the relation between the force due to inertia and the force due to gravitation. For towing tank research, in which it is widely used, it quantifies the influence of gravity on the motion of the fluid. The Froude number can be expressed as the length of the bow wave. If the length of the bow wave is equal to the length of the ship, the critical Froude number of 0.4 is reached. For higher speeds, wavemaking resistance is increased dramatically until planing behaviour is achieved. For $Fn >> 0.5$, the ship is planing and wavemaking resistance is decreased.

The equation for the Froude number holds:

$$Fn = \frac{v}{\sqrt{gl}} \tag{2.4}$$

In which v equals the velocity of the ship, g gravitational acceleration and l the length of the ship.

The Froude number is often not mentioned in experimental research into hydrofoils because they are usually operated at high Froude numbers. In chapter 3, the properties of the foil and the script for the experiments are discussed. To calculate the lowest Froude number for the experiments, $v = 2\,ms^{-1}$ and $l = c_{vertical} = 92.4 \cdot 10^{-2}\,m$. Using equation 2.4, $Fn = 2.1 >> 0.5$. It is chosen to neglect the Froude number in this research because the influence of the wavemaking resistance of the strut is expected to be insignificant.

2.1.4 Boundary layer transition point

The boundary layer transition point N_{crit} is a measure for free flow turbulence and is used to simulate the transition location when no location is given. Smith and Gamberoni concluded that an N-factor of 9, was similarly effective across correlating experiments (Smith & Gamberoni, 1956). In a historical review of work at TU Delft, Van Ingen concluded the N-factor is allowed to grow to 9. Above this threshold, the method loses its validity due to highly turbulent flows (Van Ingen, n.d.). The highest N-factor; $N_{crit} = 9$ is chosen because turbulence is expected in the tank setup.

2.1.5 Mach number

The Mach number, invented by Ernst Mach, is used in fluid dynamics to describe the relative flow velocity past a boundary with respect to the speed of sound in that medium. It is a measure of the compressibility of the medium and described by the following equation:

$$M = \frac{v_\infty}{c} \tag{2.5}$$

In which v_∞ is the freestream velocity with respect to the boundaries and c the speed of sound in the medium.

For the experiments the highest Mach number is found at $v_m = v_\infty = 6\ ms^{-1}$. Using a speed of sound in water at $20°C$ of $1481\ ms^{-1}$, a Mach number of 0.004 is found. A Mach number this small is considered irrelevant for this study.

2.2 Calculation of lift and drag

The hydrodynamic properties of a hydrofoil entail the entire spectrum of lift and drag coefficients produced by a defined surface. Modern day technology provides numerical software packages to analyse and develop foils. One of the first and most recognised programs is X-foil, which calculates the hydrodynamic properties of a foil section in a viscous environment for low Reynolds numbers (Drela, 1989). The software primarily uses potential flow theory, which is expanded with superimposed source distributions on the foil and wake, to permit modelling viscous layer influence (Drela, 1989). After the development of X-foil, more numerical packages for calculating the performance of hydrofoils became available. The modern numerical packages enable the calculation of 3D effects. An example of such a package is XFLR5, which has now been succeeded by a paid version named Flow 5. Flow 5 is able to calculate 3D effects taking into account the presence of a hub, hull or any other objects near the foil. This section will discuss the theoretical foundation of these numerical packages in order to give a better understanding of the phenomena influencing the lift and drag of a hydrofoil.

2.2.1 Thin airfoil theory

When a body is placed in a moving medium, depending on the shape, angle of attack and freestream velocity, a hydrodynamic force is created. The component perpendicular to the freestream velocity is called lift. To calculate the lift, thin airfoil theory is applied. This method was invented by Max Munk and further developed by Ackroyd & Riley (2011). It relates angle of attack to lift, for an incompressible and non-viscous flow, past an airfoil section. The fundamental method behind the theory is to replace an airfoil with a vortex sheet along the chord line, which has the condition to be a streamline. In other words; the flow is idealised as a 2-dimensional flow around an airfoil of zero thickness and infinite wingspan. The distribution of vortices can then be used to find the lift, moment and pressure over the airfoil section.

The lift per unit span can be described by the theoretical lift equation:

$$C_l = C_{l0} + 2\,\pi\,\alpha \tag{2.6}$$

In this equation C_l equals the lift coefficient for infinite wingspan and C_{l0} the section lift for zero angle of attack. For non-cambered foils, C_{l0} equals zero. α is the angle of attack relative to the chord line.

Thin airfoil theory concludes another important property for airfoils in 2-dimensional, non-viscous flow. Namely that the aerodynamic centre lies exactly one quarter behind the leading edge. For non-cambered foils the centre of pressure coincides with the aerodynamic centre while for cambered foils, the centre of pressure moves when the angle of attack is changed. The centre of pressure is the location where the total sum of the pressure field is acting. The aerodynamic centre is the location from where lift and drag force exert no moment on the foil.

2.2.2 Lifting Line theory

Thin airfoil theory is limited to calculating the lift around a section. To move from a section to a 3D body, lifting line theory is applied. This is developed by Prandtl (1936) and Lanchester (1907) based on an unswept elliptical wing.

It was concluded that vortices developed as a result of inwash on the top side of the foil and outwash on the bottom side of the foil. As a result of these vortices downwash occurs behind the foil, leading to a change in angle of attack and consequently a variation of lift across the span of the foil.

The change in lift angle is expressed as induced drag (C_{D_i}) which can be calculated as follows for an elliptical wing:

$$C_{D_i} = \frac{C_L^2}{\pi AR} \tag{2.7}$$

In which the aspect ratio:

$$AR = \frac{s^2}{A} \tag{2.8}$$

In this equation s equals the wingspan and A the surface area of one side of the foil.

So far, only an approximation for elliptical wings has been made. To calculate the influence of induced drag for non-elliptical wings, Helmbold (1957) introduced an intermediate step.

$$C_L = \frac{AR}{AR+2}\, C_l \tag{2.9}$$

This approximation of C_L for finite wingspans is used subsequently in equation 2.7 to calculate the contribution of induced drag.

2.2.3 Calculation of drag

Lifting line theory introduced a drag component due to a change in the angle of attack. However, the object itself is also due to drag which can be attributed to two main components: skin friction and pressure drag. Skin friction is due to the viscosity of the medium and pressure drag is a result of the collisions between the object and the medium. To calculate the drag as a result of these two components, the following equation can be used (Dobes & Kozubková, 2014):

$$\int_{surface} C_f \, \frac{\rho v_{\inf}^2}{2} \, dA \tag{2.10}$$

In this equation C_f is a function of the Reynolds number. Turbulent flow will create more drag than laminar flow. This is amplified in figure 2.1 where the influence of turbulence is discussed. Depending on this flow condition a different function of the Reynolds number is used.

The function for $C_{f-laminar}$ is determined for the laminar flow across a sphere. For hydrofoils, up to the critical Reynolds number, flow is laminar. The equation to calculate C_f holds as follows:

$$C_{f-laminar} = \frac{24}{Re} + \frac{4}{\sqrt{Re}} + 0.4 \tag{2.11}$$

To calculate C_f for the turbulent regime, Prandtl's Power Law is used (Prandtl, 1936). The transition to this regime often happens around an AoA of ± 13 ° for foils.

$$C_{f-turbulent} = \frac{24}{Re} + \frac{4}{\sqrt{Re}} + 0.4 \tag{2.12}$$

2.2.4 Compensations for 3D effects

Apart from the lifting line theory, more methods to compensate for 3D effects are available. These methods are used to compare wingshapes which are more distinct to the elliptical shape. To compare these methods, the Oswald efficiency factor (e) which represents the losses of a wing compared to an idealised wing having the same aspect ratio and an elliptical lift distribution, is introduced. Approaches to calculate different wings are compared in figure 2.2.

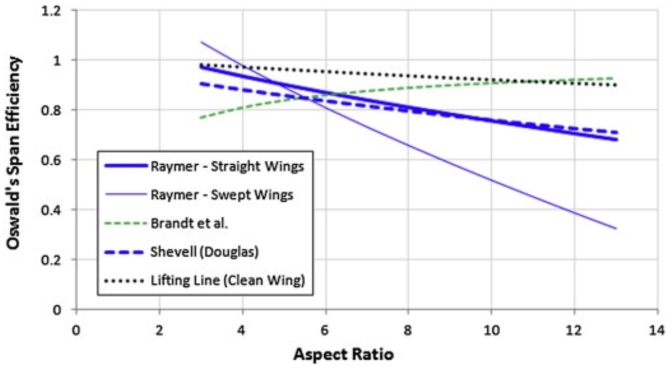

Figure 2.2: Comparison of four methods estimating the Oswald span efficiency factor vs. the aspect ratio (Kundu et al., 2016)

2.2.5 Compensation for free surface effects

As a result of close proximity to the surface and the strut of the foil piercing through the surface, surface effects occur.

The strut piercing the surface creates spray. This spray is lost energy and can thus be expressed as a component to the drag. A relation between $C_{D_{spray}}$ and the width and chord length of the strut is expressed in equation 2.13 (Chapman, 1971).

$$C_{D_{spray}} = 0.009 + 0.013 \left(\frac{t_{vertical}}{c_{vertical}} \right) \tag{2.13}$$

In this equation $t_{vertical}$ equals the width and $c_{vertical}$ the chord length of the strut.

When the proximity to the surface is decreased, the horizontal of the foil starts to interfere with the surface resulting in an additional viscous drag component. Patterson & Binns (2021) researched this effect in experimental research where the asymptote for C_L and C_D for increasing h/c was compared with the entire spectrum. The comparison was made by introducing the correction factor ($K1$) for viscous drag which can be described as a function of h/c and Fn. Figure 2.3 depicts his findings.

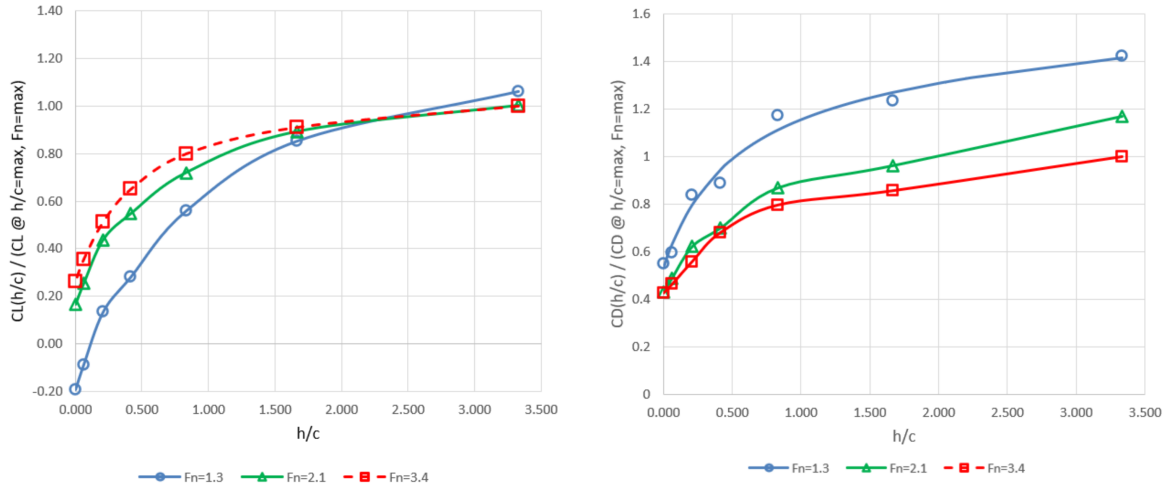

Figure 2.3: Free surface effect on steady state lift and drag for T-foil ($AR = 5$) at: $AoA = 6$ °, and maximum $h/c = 3.33$ (Patterson & Binns, 2021)

In addition the results were compared to XFLR5 which concluded that $N_{crit} = 7$ and $K1 = 1.45$ give the most suitable replication of the experimental data. The correction $K1$ was implemented in the drag equation as follows:

$$C_{D_{total}} = C_{D_i} + K_1 \left(C_{D_{horizontal}} + C_{D_{vertical}}\right) + C_{D_{spray}} + C_{D_{int}} \tag{2.14}$$

In this equation $C_{D_{int}}$ is a compensation for the interference between the vertical and horizontal which will be discussed in section 2.2.6.

2.2.6 Drag due to interference of flows in the T-junction of vertical and horizontal

In the T-junction, where the vertical and the horizontal of the foil connect, flow around both wings interferes. A method to compensate for the drag due to the interference in the junction is proposed by Hoerner (1965). The relative thickness $t' = \sqrt{t_{vertical}\ t_{horizontal}}$ is used to calculate the drag due to the interference in the junction:

$$D_{int} = 0.5\ \rho\ t'\ c_{vertical}\ v_{knots}^2\ C_{D_{int}} = 0.5\ \rho\ t'\ c_{vertical}\ (1.94\ v_\infty)^2\ C_{D_{int}} \tag{2.15}$$

In which $C_{D_{int}}$ is to be extracted from the figure presented in figure 2.4.

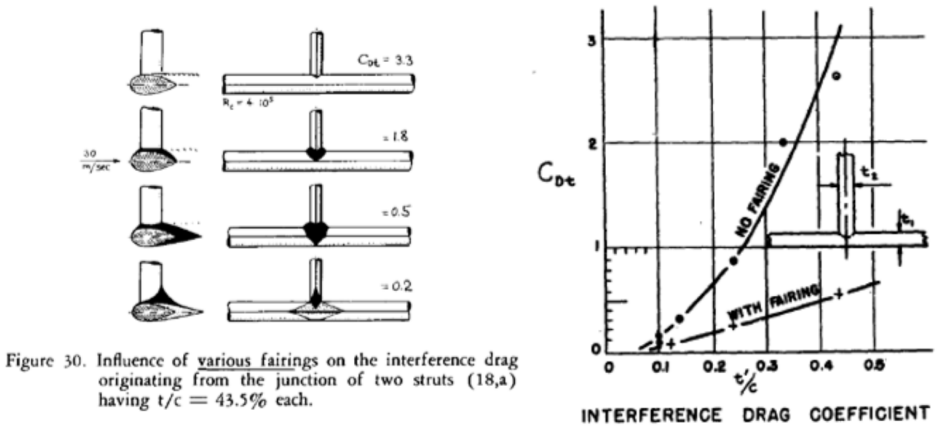

Figure 2.4: Interference drag coefficients for T-foil with various fairings (Hoerner, 1965)

2.2.7 Theodorsen's Model

Above theories provide an estimation for quasi steady state conditions. Theodorsen's model extents this estimation by including the effect of added mass and wake vorticity (Theodorsen & Mutchler, 1935). An estimation for the lift in these dynamic motions can be made in case of rapid motions. Theodorsen adds a component of added mass to the quasi steady state lift and multiplies by a transfer function.

$$C_L = \left(C_L^{QS} + C_L^{AM}\right)\ C(k) \tag{2.16}$$

The additional lift created by the accelerated mass of fluid around the foil is accounted for by the term of added mass (C_L^{AM}) which is is calculated as follows:

$$C_L^{AM} = \pi\ \left(\ddot{h} + \dot{\alpha} - a\ \ddot{\alpha}\right) \tag{2.17}$$

Theodorsen's model describes a transfer function $C(k)$ to account for lift attenuation by the wake vorticity as a function of Hankel functions (Theodorsen & Mutchler, 1935).

$$C(k) = \frac{H_1^{(2)}(k)}{H_1^{(2)}(k) + i\, H_0^{(2)}(k)} \tag{2.18}$$

2.3 Phenomena in waves

The flow direction rotates with the wave (figure 2.5) and therefore has an influence on the lift and drag of a hydrofoil. In this section an overview of the phenomena in waves will be given based on potential flow theory described in the course paper for Hydromechanica 4 by Gerritsma (2015). For the application of this theory, it is assumed that the fluid is non-viscous, homogeneous and incompressible.

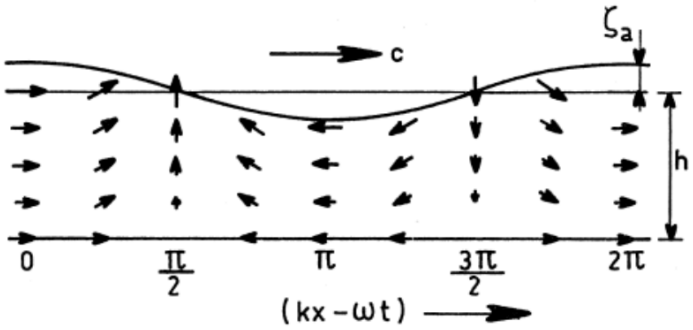

Figure 2.5: Motion field in a cylindrical wave at limited depth (Gerritsma, 2015)

.

2.3.1 Particle velocity and direction in waves

A wave can be described by waveheight (ζ) as a function of location (x) and time (t):

$$\zeta = \zeta_a\ \cos\left(k\, x - \omega\, t\right) \tag{2.19}$$

In this function the wave amplitude equals ζ_a, the wave number k and the angular velocity ω. The wave number is calculated using the dispersion relation in which the wave length λ is related to the wave number:

$$k = \frac{2\pi}{\lambda} = \frac{\omega^2}{g} \tag{2.20}$$

Assuming that the medium is non-viscous, homogeneous and incompressible, the Laplace and Bernoulli equation can be used to form the equation for the wave potential:

$$\phi = \frac{\zeta_a \, g}{\omega} \, \frac{\cosh(k \, (h+z))}{\cosh(k \, h)} \sin(k \, x - \omega \, t) \tag{2.21}$$

Integrating the wave potential gives the motion of the particles in u and w-direction which correspond to the x and z-direction:

$$u = \frac{\delta\phi}{\delta x} = \zeta_a \, \omega \frac{\cosh(k \, (h+z))}{\sinh(k \, h)} \cos(k \, x - \omega \, t) \tag{2.22}$$

$$w = \frac{\delta\phi}{\delta z} = \zeta_a \, \omega \frac{\sinh(k \, (h+z))}{\sinh(k \, h)} \sin(k \, x - \omega \, t) \tag{2.23}$$

The equations of the particle motions can be used to calculate the angle of attack and stream velocity at the foil as follows:

$$AoA = \tan\left(\frac{w}{u + v_\infty}\right) \tag{2.24}$$

$$v_f = \sqrt{(u - v_\infty)^2 + w^2} \tag{2.25}$$

2.3.2 Waves-foil interaction for a Moth

With the above equations, the phenomena experienced by Moth sailors can be substantiated. To do so, a typical conditions in which Moths sail is chosen.

This condition corresponds with a wave amplitude of 0.15 m and a wave length of 5 m. The boat is sailed at a boat speed of 18 $knots \approx 9 \, ms^{-1}$ at a submergence of 0.20 m which corresponds to $h/c \approx 2$. Using equation 2.20, k and ω are found: $k = 1.26$, $\omega = 3.5$.

If equation 2.24 and 2.25 are simplified using the above parameters, the resulting functions lead to the graphs shown in figure 2.6. In the top graph, the quiver depicts the particle velocity and direction at foil height, the red dot represents the foil position and the blue line shows the wave. The bottom graph shows the angle of attack and stream velocity experienced by the foil.

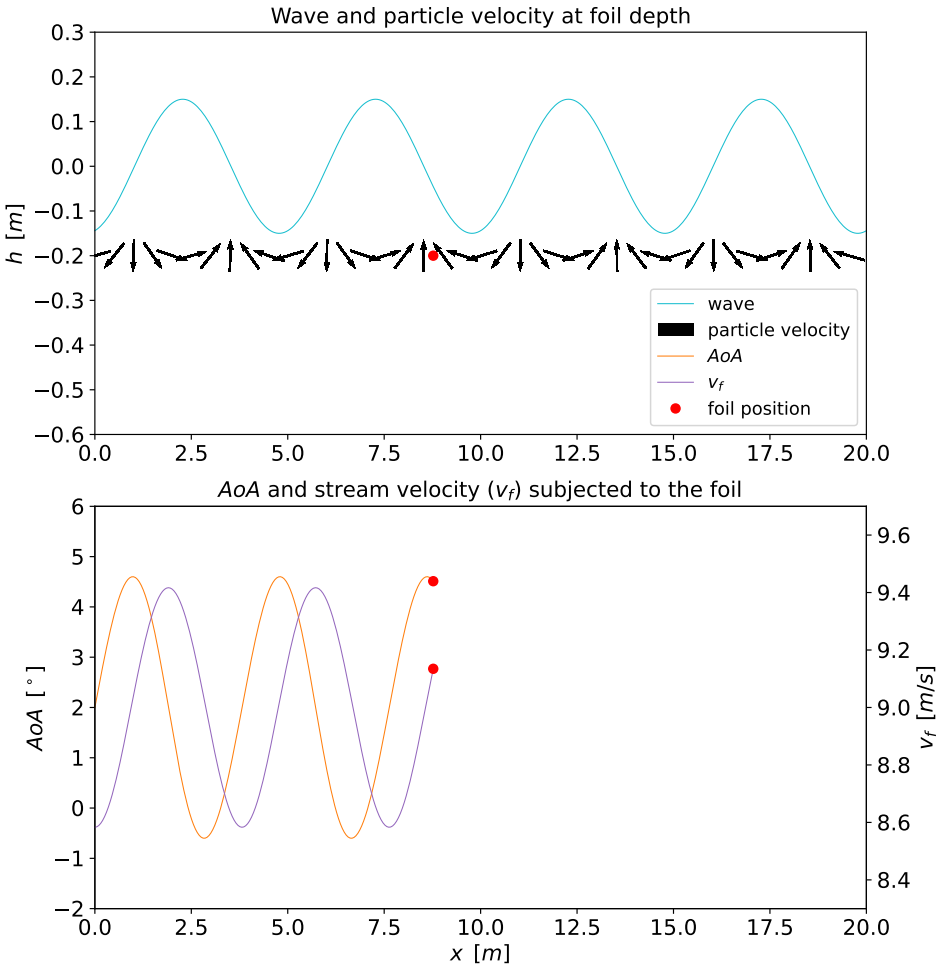

Figure 2.6: Simulation of velocity and direction at foil in waves at: $h/c = 1.5$ and $v_\infty = 2\ ms^{-1}$

It can be seen that for the given conditions, the angle of the flow varies between -0.6 ° and $+4.6$° and that the velocity of the incoming flow varies with $\pm 0.6\ ms^{-1}$. The flow velocity lags the flow angle by exactly a quarter period. Combining all these observations, considerably high fluctuations in hydrodynamic forces can be expected at the given conditions. From the figure it can be concluded that the fluctuations have a sinusoidal character.

2.4 Filter methods

Filters are commonly used tools to process signals in experimental research. A filter removes undesired components from the signal depending on its settings. Two filters that show promising features are examined on their performance. Firt the Butterworth band filter will be discussed which is a linear continuous-time filter able to remove frequency bands. Afterwards, the digital Savitsky Gollay filter its ability to remove noise from a signal is analysed.

2.4.1 Butterworth band filter

A bandwidth filter is a commonly used filter which divides the signal into multiple sinusoidal functions. Depending on the settings of the filter, a bandwidth of sinusoidal functions is extracted from the original signal. The Butterworth filter is an extended application of the bandwidth filter (Butterworth, 1930). The order in which the signal is to be approximated can be controlled. This enables a more accurate approximation of the signal. A

disadvantage of the Butterworth filter is a high roll-on and roll-off period. To reduce this period, a higher order is required. The disadvantage of a higher order is that, presumably undesired, ripples occur in the approximation.

Before applying the Butterworth band filter, analysis of the signal is required. This is done using a Fast Fourier Transform (FFT) spectrum which attributes the impurities in the measurement to specific sources in the test setup of which the frequency is known. Combining this with the expected frequency of the measurement, an estimation of the bandwidth can be made.

2.4.2 Savitsky Golay filter

A different approach to filter data is the Savitsky Golay (SavGol) filter (Savitzky & Golay, 1964). This digital filter increases the precision without distorting the overall shape of the signal. The process used is known as convoluting. Successive sub-sets of data are fitted with a polynomial using the least squares method. For a data set with equal spacing, in this case the time domain, an analytical solution can be found. This analytical solution is presented as a single set of convolution coefficients that can be applied to all sub-sets of the signal. The advantage of this approach is that it uses the entire data set and predicts what has happened, using the data from before and after the point.

For the Savitsky Golay filter a Python library named Savgol is available. In this filter, the following parameters have to be set:

- Y-values; this is the signal that requires filtering.
- Window size; this is the size of the domain of the sub-set, over which the least squares method is to be applied.
- Order; this is the degree of the polynomial that is fitted over the sub-set.
- Derivative; this is an option to find the filtered derivative of the input signal.
- Delta; this is the spacing of the x-axis which is in this case the time domain.

2.5 Other used methods

This section will elaborate on the methods and principles used in this thesis which have not yet been discussed in the above sections. It comprehends Newton's laws, a method to make a surface function fit and the mathematical method to rotate vectors.

2.5.1 Newton's laws

Mass, velocity, acceleration and force are related. This is expressed in three law's commonly known as Newtons Law's of motion.

1. A body remains at rest, or in motion at a constant velocity in a straight line, unless acted upon by a force.
2. When a body is acted upon by a force, the time rate of change of its momentum equals the force.
3. If two bodies exert forces on each other, these forces have the same magnitude but opposite directions.

Newton's second law translates into the following equation:

$$F = m\,\vec{a} \tag{2.26}$$

2.5.2 Surface function fit

Multiple parameters were changed during the experiments. In this way, their influences could be investigated. Following the experiments, a plot could be made of the results as a function of the chosen variables. To express the influence of the parameters, a surface fit was made. The surface fit was made using a Bernstein polynomial which was constructed by a linear combination of Beziér curves (Lorentz, 1953). The Beziér curves are defined by the following equation:

$$b_{v,n}(x) = \binom{n}{v} x_v (1-x)^{n-v} \tag{2.27}$$

Using the above curves in a linear combination, a curve with degree n can be described by the following summation of functions:

$$B_n(x) = \sum_{v=0}^{n} \binom{n}{v} (x_{min} - x)^v (x_{max} - x)^{n-v} \tag{2.28}$$

In this function x_{min} and x_{max} are defined by the beginning and end of the domain. The order n can be chosen manually. In the case of experimental research, the order is chosen according to the expected result.

Two of these Bernstein polynomials are used because a 3D surface is to be replicated. They are computationally more efficient and lead to smoother and more stable descriptions than traditional polynomials (Nava et al., 2012). They are constructed as follows:

$$f_j = \sum_{j=0}^{n} \binom{n}{j} (x_{min} - x)^j (x_{max} - x)^{n-j} \tag{2.29}$$

$$g_j = \sum_{k=0}^{n} \binom{n}{k} (y_{min} - y)^k (y_{max} - y)^{n-k} \tag{2.30}$$

$$z_{jk} = f_j \cdot g_k \tag{2.31}$$

2.5.3 Rotation and translation

Rotation and translation of vectors was required because multiple reference frames were used. The rotation of a vector is done using Euler's rotation theorem (Euler, 1776). A vector $[x, y, z]$ is rotated by angles $[\phi, \theta, \psi]$

$$\begin{bmatrix} x' \\ y' \\ z' \end{bmatrix} = R_x(\phi)\, R_y(\theta)\, R_z(\psi) \begin{bmatrix} x \\ y \\ z \end{bmatrix} = A(\phi, \theta, \psi) \begin{bmatrix} x \\ y \\ z \end{bmatrix} \tag{2.32}$$

3x3 matrix A is a real, orthogonal matrix, hence each of its rows or columns represents a unit vector.

$$A(\phi, \theta, \psi) = \begin{bmatrix} \cos\theta\cos\psi & -\cos\phi\sin\psi + \sin\phi\sin\theta\cos\psi & \sin\phi\sin\psi + \cos\phi\sin\theta\cos\psi \\ \cos\theta\sin\psi & \cos\phi\cos\psi + \sin\phi\sin\theta\sin\psi & -\sin\phi\cos\psi + \cos\phi\sin\theta\sin\psi \\ -\sin\theta & \sin\phi\cos\theta & \cos\phi\cos\theta \end{bmatrix} \tag{2.33}$$

3 | Experimental setup

This chapter starts by detailing the design choices for the T-foil. With these properties an estimation of the hydrodynamic forces is calculated and presented. The estimation of the total load was used to design the experimental setup. Every element of this setup is discussed in order to explain the working principle, calibration and accuracy. At the end of the chapter, the script containing the tests used to achieve the objective is presented.

3.1 Properties of the T-foil

The TU Delft developed and has made available a platform to develop the science of hydrofoil engineering, which is named Hydrofoil Education and Research Platform (HEARP). The platform can be used to investigate control systems, T-foil configurations and foil behaviour. Therefore the foil had to fit the HEARP. It was chosen to use a T-foil because of their requirement for an active control system and their higher potential in terms of efficiency compared to other foil types. The requirement to fit the platform, introduced a limitation to the span of 400 *mm*. Another reason to choose this size of foil are the properties of the hexapod, which controls the pose of the foil during experiments. If larger foils were used, the effects of surface interaction would be hard to distinguish. The review paper on the fluid dynamics of flapping foils by Wu et al. (2020) provides an overview of research into foils which states that over 40 studies use the NACA 0012 profile for their experiments. Binns has used a NACA 0012 section to study vortices and surface interaction (Binns et al., 2008). It was decided to scale the foil geometry to fit the maximum span of 400 *mm* because Binns' research gives clear dimensions and can partly be used to benchmark experiments in steady state conditions. Figure 3.1, shows the chosen foil and its properties. Properties such as the surface area are extracted using the tools from the 3D drawing application Rhino 7.

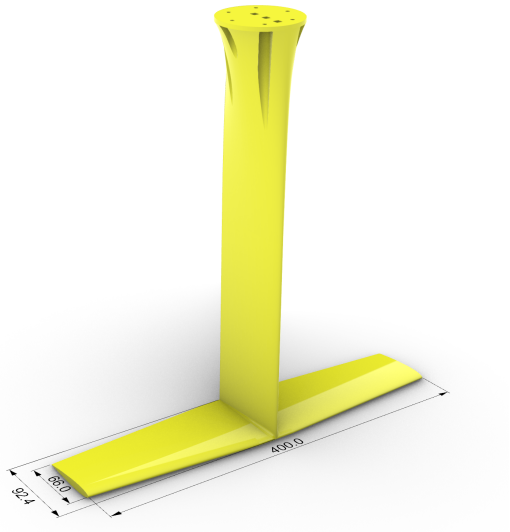

Horizontal		
span	$s = 400$	mm
chord - root	$c_r = 92.4$	mm
chord - tip	$c_t = 66.0$	mm
chord - mean	$c_m = 80.5$	mm
area	$A = 32212$	mm^2
Vertical		
chord	$c = 92.4$	mm
area per h/c	$\frac{Ac}{h} = 8538$	mm^2

Figure 3.1: NACA 0012 dimensions

For the majority of the experiments, a foil finish pursuant to an aerodynamically smooth and flat surface was chosen. This foil, which will be referred to as NACA 0012, is finished using several layers of spray filler, primer and paint to remove pin holes and roughness from the 3D print. To remain the foil shape as printed in the 3D printer, the foil was sanded until the plastic of the 3D print became visible after each layer of spray paint. From the 3D printer a maximum deviation of 0.3 *mm* can be expected. The roughness of a surface can be expressed with the last and thus finest grid of sanding paper which for the model T-foil is P2000. For exploratory research into the effect of surface finish, a second foil was used which had no surface finish. Both foils were built the same way using a carbon reinforced 3D print. The raw printed foil has 0.15 *mm* 3D printed layer aligned chordwise with the foils. A 3D drawing providing the location of the reinforcements is presented in figure 3.2.

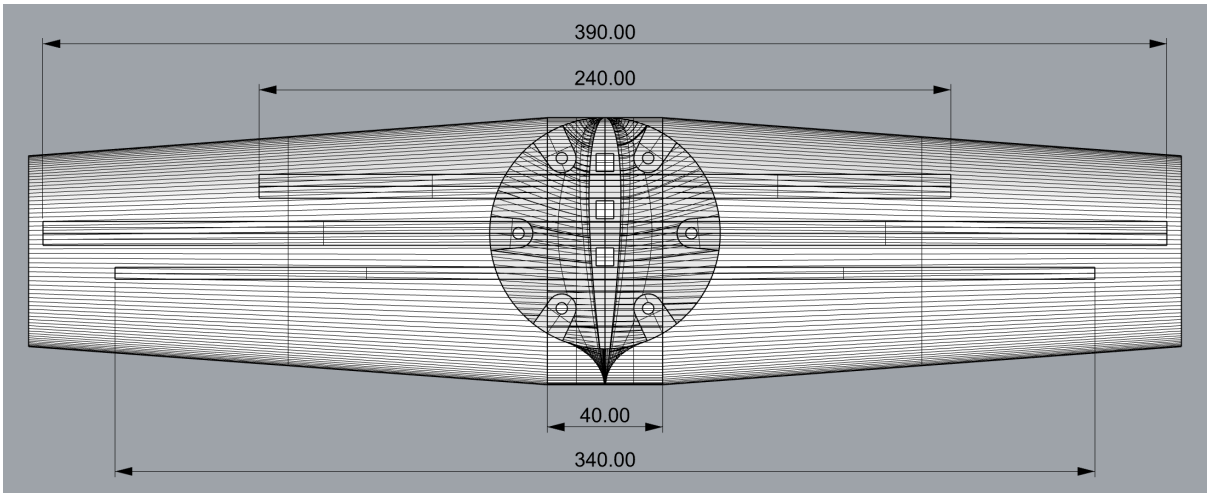

Figure 3.2: Carbon reinforcement rods in the NACA 0012 which was used in the experiments

For the vertical, the carbon reinforcement consists of three 6×6 *mm* pultrusion square rods which support the entire length providing sideways stiffness. The flexual rigidity around the x-axis provided by this carbon reinforcement is calculated using a Young's Modulus (E_1) of $135 \cdot 10^9$ and equals:

$$EI_{vertical} = E_1 \; 1/12 \; b \; h^3 = 43.73 \; Nm^2$$

The horizontal is supported by a 40 *mm* 12×2 *mm* strip in the back, a 340 *mm* 4×4 *mm* square rod in the middle and two 8×4 *mm* rectangular rods in the front with a length of 390 *mm* and 240 *mm*. At a quarter of the span, where 3 of the 4 reinforcement rods are located, the flexual rigidity around the x-axis by the reinforcement equals:

$$EI_{horizontal} = E_1 \; 1/12 \; b \; h^3 = 14.4 \; Nm^2$$

The second foil does not have any surface finish and is therefore named NACA 0012 RAW. Lines are added on both foils to clarify h/c and position on the chord. Figure 3.3 shows a picture of both foils.

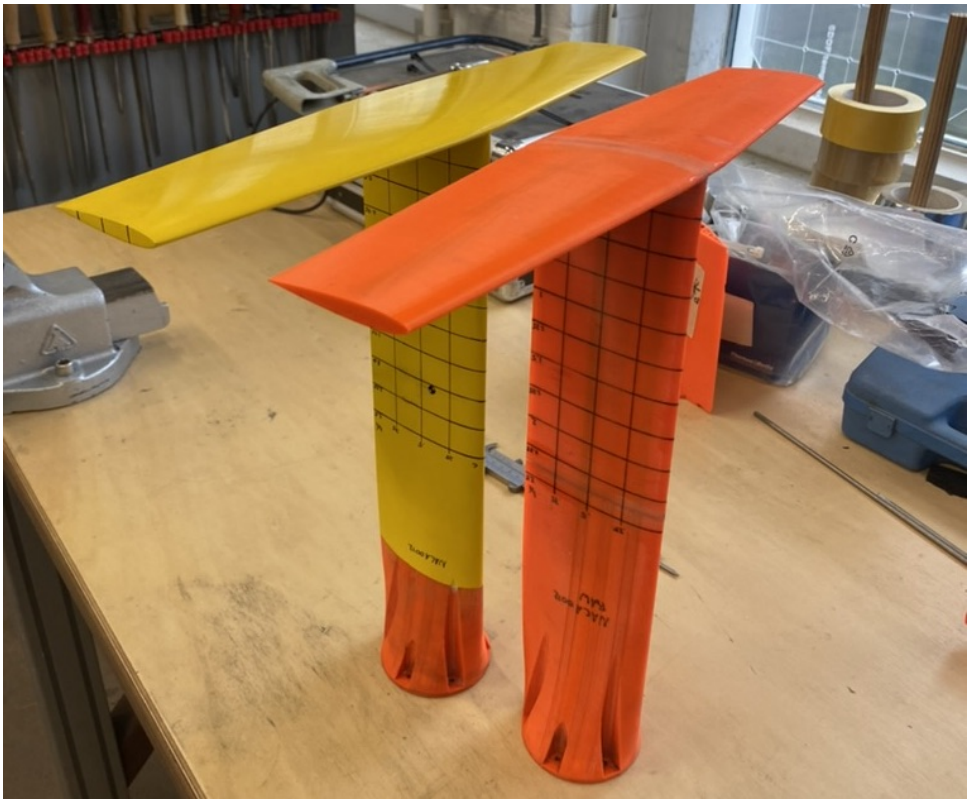

Figure 3.3: NACA 0012 foils used in the experiments

3.1.1 Force prediction

To design the towing tank setup, estimations of the hydrodynamic forces were required. The estimation of the forces was used to define and specify the load gauges. This paragraph will elaborate on the calculations for the chosen T-foil in steady state conditions based on the discussed methods in section 2.2. X-foil's prediction of the hydrodynamic coefficients for a NACA 0012 foil was used because X-foil is used in similar research and is publicly available. A compensation for the 3D effects was made afterwards. An estimation of the contribution of the vertical is given at the end of the paragraph.

The experiments were ran at model velocities of 2, 4 and 6 ms^{-1}. For the conditions in the TU Delft Towing tank and the properties of the chosen foil, the Reynolds number was calculated using equation 2.1. The Reynolds number for the given model velocities corresponds to respectively 1.5, 3.1 and $4.6 \cdot 10^5$.

Secondly, the boundary layer transition point setting should be chosen. As described in section 2.1.4, an N-factor of 9 correlated with similar experiments (Smith & Gamberoni, 1956). $N_{crit} = 9$ because turbulence was expected in the towing tank.

To make a precise estimate of the sectional hydrodynamic coefficients, an interpolation function was applied to a data set from X-foil to find C_l and C_d as a function of Re and AoA. This data set includes $Re = [0.5,\ 1,\ 2,\ 5,\ 10] \cdot 10^5$ and $AoA = [-13 - 13]\ ^\circ$. The resulting interpolation fits are shown in figure 3.4. The data set is given in appendix A.

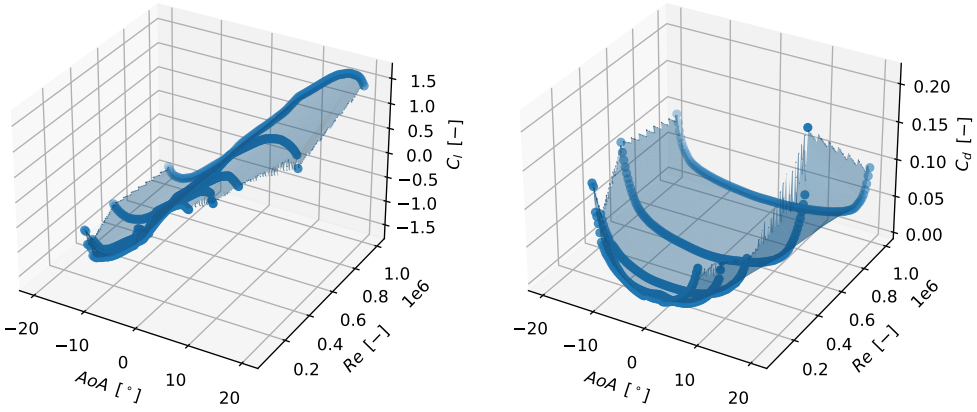

Figure 3.4: X-foil interpolation function

A compensation for the finite wingspan was made using the lifting line theorem as discussed in section 2.2.2 using equation 2.9. The 3D lift coefficient (C_L) was used in equation 2.2 to find the lift. The simplified equation for C_L holds:

$$C_{L.xfoil} = C_l(AoA, Re)\ \frac{AR}{AR+2} \tag{3.1}$$

and:

$$L_{xfoil} = 1/2\ C_{L.xfoil}\ v_\infty^2\ \rho\ A_{horizontal} \tag{3.2}$$

The horizontal has an angle of attack and is thus subjected to induced drag. The effect of induced drag (C_{D_i}) was added to the drag coefficient of the horizontal coming from X-foil using equation 2.7. The drag of the horizontal can then be calculated using equation 2.3. The simplified equation for $D_{horizontal}$ holds:

$$D_{horizontal} = 1/2\ \left(C_d(AoA, Re) + C_{D_i}\right)\ v_\infty^2\ \rho\ A_{horizontal} = 1/2\ \left(C_d(AoA, Re) + \frac{C_L^2}{\pi\, AR}\right)\ v_\infty^2\ \rho\ A_{horizontal} \tag{3.3}$$

In both of the above equations 3.1 and 3.3:

$$AR = \frac{s^2}{A_{horizontal}} = \frac{0.4^2}{32212 \cdot 10^{-}6} = 5.0 \tag{3.4}$$

In this equation s equals the wingspan and $A_{horizontal}$ the surface area of one side of the foil horizontal.

The foil is not subjected to yaw, hence no induced drag will act on the vertical. The loss of energy in spray is expressed in the component $C_{D_{spray}}$ which is calculated using equation 2.13. If this is combined with the sectional drag coefficient from X-foil, the equation for the component of drag by the vertical is found:

$$D_{vertical} = 1/2\ \left(C_d(AoA, Re) + C_{D_{spray}}\right)\ v_\infty^2\ \rho\ A_{vertical} = 1/2\ \left(C_d(AoA, Re) + 0.01056\right)\ v_\infty^2\ \rho\ A_{vertical} \tag{3.5}$$

In this equation the area of the vertical is calculated using the following equation derived from figure 3.1:

$$A_{vertival} = 8538 \cdot 10^{-6}\ \frac{h}{c} \tag{3.6}$$

At last the compensation for the interference in the T-joint was made by introducing the interference drag (D_{int}). This is calculated using equation 2.15. $C_{D_{int}}$ is estimated 0.15 using figure 2.4.

$$D_{int} = 1/2\ \rho\ t'\ c_{vertical}\ (1.94\ v_\infty)^2\ C_{D_{int}} \tag{3.7}$$

The total drag is calculated by adding the three terms together:

$$D_{xfoil} = D_{int} + D_{horizontal} + D_{vertical} \tag{3.8}$$

The total drag is used in equation 2.3 to calculate the drag coefficient from X-foil ($C_{D.xfoil}$ which will be used in chapter 5 and 7 as follows:

$$C_{D.xfoil} = \frac{2\ D_{xfoil}}{v_\infty^2\ \rho\ A_{horizontal}} \tag{3.9}$$

Yet, no compensation for free surface proximity was made to the lift and drag since this will only decrease the approximation and will not be relevant at deeper submergence. An estimation of a free surface proximity compensation will be made in chapter 5 and used in chapter 7.

The theoretical prediction using X-foil shows the lift and drag in steady state conditions for $h/c = 2.5$ and is presented in figure 3.5. The lift was calculated for 2 and 6 ms^{-1}. The majority of the tests were conducted at 2 ms^{-1} so that partly defines the load gauges for the test setup. As the load gauges should not be damaged at $v_\infty = 6\ ms^{-1}$, the prediction of the forces should not exceed the limit of a load gauge.

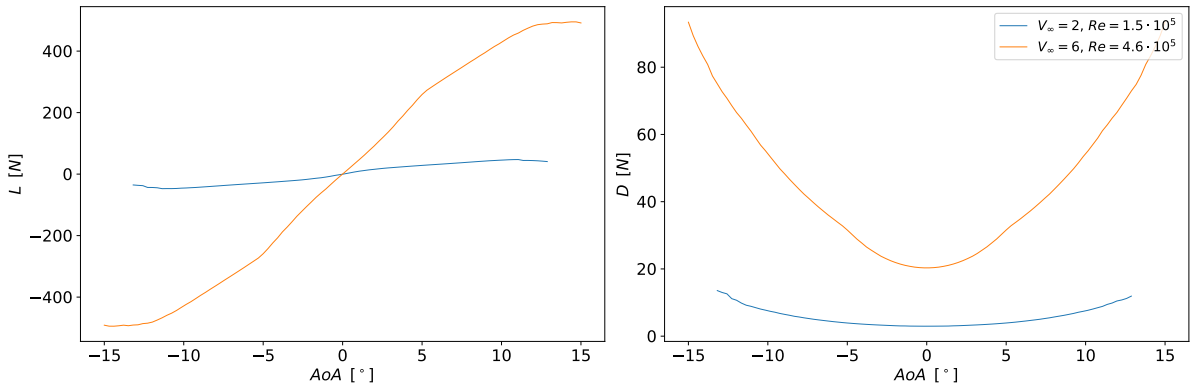

Figure 3.5: Estimation of lift and drag vs. angle of attack for NACA 0012 at: $h/c = 2.5$

The prediction of the hydrodynamic forces was used to make a prediction of the forces on the sensor. First, the mass of the foil and the bottom plate of the 6DOF sensor ($m = 15\ kg$) were extracted from the lift force. Then, a rotation was performed to change to the coordinate system of the 6DOF sensor.

$$F_{z_{6DOF}} = (L_{xfoil} - m\ g)\ \cos(\alpha) - D_{xfoil}\ \sin(AoA) \tag{3.10}$$

$$F_{x_{6DOF}} = (L_{xfoil} - m\ g)\ \sin(\alpha) + D_{xfoil}\ \cos(AoA) \tag{3.11}$$

For each steady state test scenario (table 3.1), a prediction of the maximum force and moment on the setup was calculated. The most extreme load case was found for the experiment at a velocity of 6 ms^{-1}, an angle of attack of $-5\ ^\circ$ and a submergence of $h/c = 2.5$. The weight of $\approx 15\ kg$ below the gauges makes a notable contribution to the overall forces. The expected forces on the 6DOF load gauge are: $M_y = -6.8\ Nm$, $F_z = -401\ N$ and $F_x = 36.6\ N$. The results from this maximum load case are used in section 3.2.5 to calculate the forces on the individual load gauges and choose which size of load gauge was to be used in the setup.

It was decided to limit the calculations to steady state conditions because no higher forces were expected for the dynamic test scenarios. The highest expected forces during an experiment where waves are induced to the surface ($v = 6$, $AoA = 5\ ^\circ$, $h/c = 2.5$) were expected to be: $M_y = -6.8\ Nm$, $F_z = 108\ N$ and $F_x = 7.6\ N$. Precise prediction of the forces in waves was not made as these estimates predict forces well below the limits of the load gauges.

3.2 Design of the experimental setup

The TU Delft manned towing tank carriage was used to perform experiments. A Hexapod was mounted on the carriage allowing free movement in six degrees of freedom. Underneath the Hexapod a 6DOF force sensor was installed. This sensor measures the forces by the foil which is mounted underneath it. The next sections will elaborate on these and other components to measure and execute the desired experiments.

3.2.1 Towing tank facility

The towing tank, located in the faculty building of 3mE, has a total length of 142 m, width 4.22 m and a maximum depth of 2.5 m. During the experiments, the water depth varied between 2183 and 2197 mm.

The carriage facilitates experiments up to 7 ms^{-1}. Wadlin introduced the critical velocity for a towing tank. At higher velocities, transverse waves no longer accompany the foil (K. Wadlin et al., 1952). For the TU Delft towing tank this critical velocity is calculated; $v_{crit} = \sqrt{gh} = 4.6\ ms^{-1}$. During the experiments a velocity ranging from 2 to 6 ms^{-1} was used. Tests above 4 ms^{-1} were used for exploratory research.

To control the carriage one dedicated computer was used. In the carriage application, the velocity and acceleration could be set. To control the carriage a separate control system was used. This control system is located behind the model and thus has an overview of the model, the tank and the surroundings for safety. Figure 3.6 shows an overview of the experimental setup.

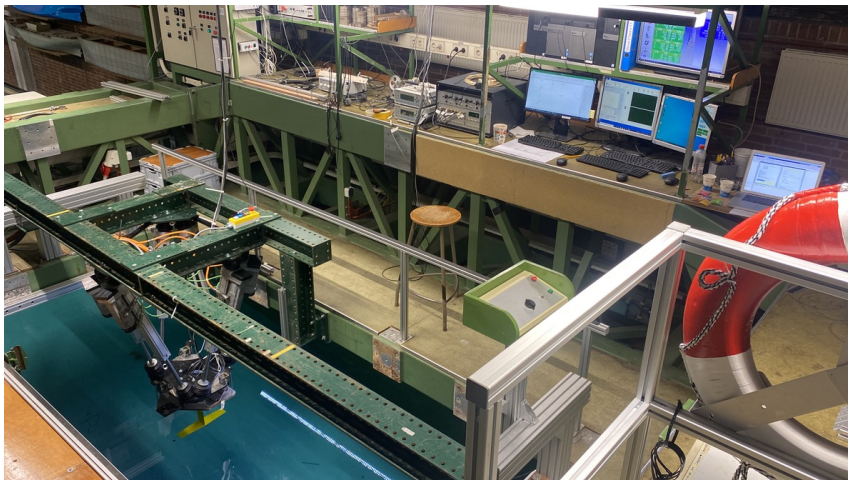

Figure 3.6: Overview of the experimental setup

3.2.2 Reference frames

For comparison of hydrodynamic forces, the foil reference frame was introduced. This frame was located on half a chord length in the middle of the foil's horizontal and corresponds with its orientation.

The standard coordinate system used by the Towing Tank of the TU Delft, which is referred to as the carriage reference frame, has been used, with the x-axis corresponding with the driving direction of the carriage. Looking from the back, the y-direction is pointing towards the left. The z-direction is pointing upwards. This reference frame is measured from the carriage and thus moves with the carriage. The origin of the carriage reference frame corresponds with the foil reference frame when the foil is located at $h/c = 0$ and $roll$, $pitch$ and yaw are zero. To facilitate maximum freedom, the location in x and y-direction is located in the middle of the Hexapod. Hence, the location and orientation of the foil reference system can be expressed with respect to the carriage.

In section 3.2.4 the settings of the Hexapod are discussed. The settings enable for the Hexapod to rotate the setup depicted in figure 3.7 around the foil reference frame. For calculation purposes, the location of the other reference frames, namely 6DOF and Certus, is depicted in the figure as well.

Location	x	y	z
$6DOF^{Foil}$	0	0	488
$Certus^{Foil}$	−78	280	424

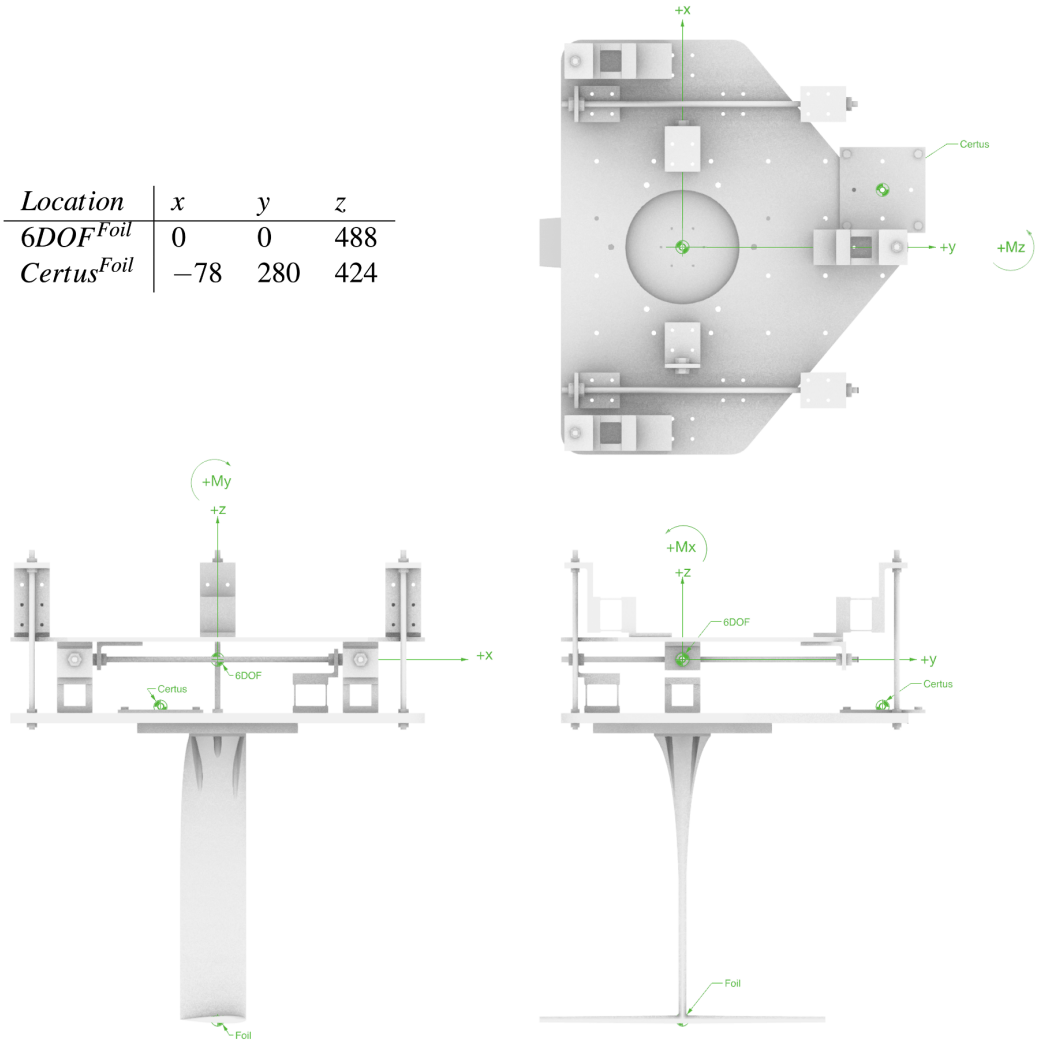

Figure 3.7: Experimental setup below hexapod showing reference frames: Foil, Certus and 6DOF

The position and orientation of the setup were measured by Certus. A reference plate located on the bottom plate of the 6DOF was used to calculate the orientation of the foil. The reference frame of the plate is referred to as the Certus reference frame.

The forces were measured using a 6DOF sensor mounted underneath the Hexapod. As a result, the forces measured by the 6DOF were rotated with the orientation of the Hexapod. Therefore the 6DOF had its own reference frame which is referred to as the 6DOF reference frame.

Another reference frame was introduced because the forces of the foil with respect to the carriage were desired. The location of this reference frame corresponds with the foil frame. However, the orientation corresponds with the carriage frame. This reference frame will be referred to as the foil-global reference frame and will be used in section 4.2.1 to translate and rotate the forces.

In equations, the reference frame will be denoted with superscript. The location to which the point refers to will be denoted with subscript. For example, the x location of the foil reference frame with respect to the carriage reference frame will be referred to as $x_{Foil}^{Carriage}$.

3.2.3 Data acquisition

In order to register the signals and control the setup, the carriage was equipped with four computers. The measurement computer was used to measure and log the data from the experiments. The analog signals, with

a frequency of 1000 Hz, were filtered using a bandwidth filter at 100 Hz. The size of this filter is default by the TU Delft Towing Tank and is chosen such because in general vibrations above 100 Hz are never attributed to measurements. The digital signals were saved directly without filtering. After each run the data could be cut based on the time trace. Three files were made after each run: a configuration file and a data file for each frequency. The 100 Hz data was saved in a separate file from the 1000 Hz data.

3.2.4 Hexapod

The Hexapod is a six-legged robot mounted at a central location to the carriage. The legs of the robot are linear motors which are controlled electrically by a computer program. The six legs allow the robot to move a plate in six degrees of freedom.

The computer program allows for advanced positioning. It can simulate movements around a specific point which corresponds to the middle of the chord and span of the foil's horizontal. This point simplifies the control of the foil by maintaining x and y zero during the tests. Another advantage of the program is that it can follow a scheme which defines time and coordinates. This allows to preset a motion and play it during an experiment.

The Hexapod was calibrated using the Certus system. The Certus system can read the location with an accuracy of 0.01 mm. The location of the Hexapod can be set to a location using an accuracy of 0.001 mm. Therefore the Hexapod settings correspond with the Certus reading with an accuracy of 0.1 mm in x and y-direction, 0.5 mm in z-direction and 0.1 deg for all rotations.

3.2.5 6DOF load gauge

The 6DOF load gauge used for the experiments was build by the TU Delft Towing tank. It consists of two stiff plates which are connected by six load gauges. The load gauges can be chosen accordingly to the expected loads. This way the 6DOF sensor can be built specifically tailored to the experiment. Figure 3.8 shows an overall view of the sensor.

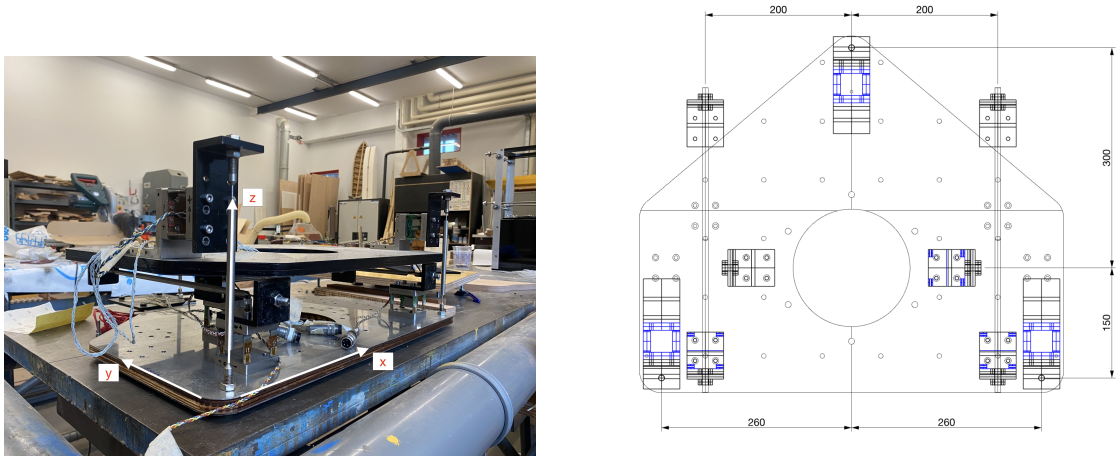

(a) (b)

Figure 3.8: 6DOF sensor

Figure 3.8a shows how the two plates are connected. The steel rods are thin near the connections to constrain the transmission of forces to one direction - the direction in which the load gauge, to which it is connected, measures. One load gauge measures in the x-direction (F1X), the second and the third measure in the y-direction (F2Y and F3Y) and the fourth, the fifth and the sixth measure in the z-direction (F4Z, F5Z and F6Z). The output of these sensors was used to calculate the forces and moments between the two plates as follows:

$$\begin{bmatrix} Fx \\ Fy \\ Fz \\ Mx \\ My \\ Mz \end{bmatrix}_{6DOF} = A\ f_{6DOF} = \begin{bmatrix} 1.0 & 0.0 & 0.0 & 0.0 & 0.0 & 0.0 \\ 0.0 & 1.0 & 1.0 & 0.0 & 0.0 & 0.0 \\ 0.0 & 0.0 & 0.0 & 1.0 & 1.0 & 1.0 \\ 0.0\ m & 0.0\ m & 0.0\ m & 0.15\ m & 0.3\ m & 0.15\ m \\ 0.0\ m & 0.0\ m & 0.0\ m & 0.26\ m & 0.0\ m & 0.26\ m \\ 0.0\ m & 0.2\ m & 0.2\ m & 0.0\ m & 0.0\ m & 0.0\ m \end{bmatrix} \begin{bmatrix} F1X \\ F2Y \\ F3Y \\ F4Z \\ F5Z \\ F6Z \end{bmatrix} \tag{3.12}$$

From the most extreme load case presented in 3.1.1 we can expect the following maximum forces: $F_x = 36.6\ N$, $F_z = -401\ N$ and $M_y = -6.8\ Nm$. If this load case is used in the inverse of equation 3.12, the forces per gauge can be calculated:

$$\begin{bmatrix} F1X \\ F2Y \\ F3Y \\ F4Z \\ F5Z \\ F6Z \end{bmatrix} = A^{-1} \begin{bmatrix} Fx \\ Fy \\ Fz \\ Mx \\ My \\ Mz \end{bmatrix}$$
$$= \begin{bmatrix} 1.0 & 0.0 & 0.0 & 0.0\ m^{-1} & 0.0\ m^{-1} & 0.0\ m^{-1} \\ 0.0 & 0.50 & 0.0 & 0.0\ m^{-1} & 0.0\ m^{-1} & -2.5\ m^{-1} \\ 0.0 & 0.50 & 0.0 & 0.0\ m^{-1} & 0.0\ m^{-1} & -2.5\ m^{-1} \\ 0.0 & 0.0 & 0.33 & -1.1\ m^{-1} & 1.9\ m^{-1} & 0.0\ m^{-1} \\ 0.0 & 0.0 & 0.33 & 2.2\ m^{-1} & 0.0\ m^{-1} & 0.0\ m^{-1} \\ 0.0 & 0.0 & 0.33 & -1.1\ m^{-1} & -1.9\ m^{-1} & 0.0\ m^{-1} \end{bmatrix} \begin{bmatrix} 36.6\ N \\ 0\ N \\ -401\ N \\ 0\ Nm \\ 0\ Nm \\ -6.8\ Nm \end{bmatrix} = \begin{bmatrix} 37\ N \\ 0\ N \\ 0\ N \\ -147\ N \\ -134\ N \\ -121\ N \end{bmatrix} \tag{3.13}$$

From equation 3.13, we learn that the highest load can be expected on the front Z load gauge. Although the maximum load is expected to be 165 N, load gauges of 100 N were selected. Above 100 N, the accuracy decreases, until 170 N the gauge measures, above 200 N the gauge deforms plastically and thus shows different readings. It can be concluded that a small margin during high velocity experiments. Monitoring of the forces is therefore required to correct reading throughout all the experiments. As explained in section 3.2.1, research at velocities above 4 ms^{-1} is considered exploratory, hence lower accuracy is allowed at 6 ms^{-1}. To maintain high accuracy at low velocity, where forces drop below 5 N, it was decided to use load gauges of 100 N. The same load gauges for all sensors were used, which enabled for quick switching of gauges if required and increased simplicity of the system. No forces in the lower region are expected important, therefore the value of smaller gauges was negligible and were thus not used.

The chosen load gauges show a linear relation between voltage and load. To find this relation, each gauge was calibrated using a setup where the gauge was loaded in steps of 0.5 kg. The resulting relation between voltage and force was saved in the measurement computer and enabled it to translate the Voltage to Newton.

The load gauges were build in house at the towing tank. A maximum measurement spread of 0.3% can be expected. During the calibration the load gauge was subjected to a stepwise increasing force. Each step, a mass of 0.5 kg was added. This was done both ways to ensure no hysteresis effects occurred. The masses are accurate to 0.001 kg. Therefore the accuracy of the calibration is 0.01 N. Combining this with the spread, a combined accuracy of 0.013 N is found.

The accuracy is different for each direction because gauges are combined to find the forces and moments in different directions. The accuracy per direction can be calculated using equation 3.12. Absolute values are used for matrix A because the absolute accuracy is desired.

$$\begin{bmatrix} E_{Fx} \\ E_{Fy} \\ E_{Fz} \\ E_{Mx} \\ E_{My} \\ E_{Mz} \end{bmatrix} = \begin{bmatrix} 1.0 & 0.0 & 0.0 & 0.0 & 0.0 & 0.0 \\ 0.0 & 1.0 & 1.0 & 0.0 & 0.0 & 0.0 \\ 0.0 & 0.0 & 0.0 & 1.0 & 1.0 & 1.0 \\ 0.0\ m & 0.0\ m & 0.0\ m & 0.15\ m & 0.3\ m & 0.15\ m \\ 0.0\ m & 0.0\ m & 0.0\ m & 0.26\ m & 0.0\ m & 0.26\ m \\ 0.0\ m & 0.2\ m & 0.2\ m & 0.0\ m & 0.0\ m & 0.0\ m \end{bmatrix} \begin{bmatrix} 0.013\ N \\ 0.013\ N \\ 0.013\ N \\ 0.013\ N \\ 0.013\ N \\ 0.013\ N \end{bmatrix} = \begin{bmatrix} 0.013\ N \\ 0.026\ N \\ 0.039\ N \\ 0.0074\ Nm \\ 0.0068\ Nm \\ 0.0052\ Nm \end{bmatrix} \tag{3.14}$$

After the calibration and assembly of the gauges in the 6DOF, the entire 6DOF was tested on interference of the load gauges also referred to as cross talk. To quantify the cross talk, the 6DOF was subjected to a similar experiment as the load gauges. The direction x and y were examined consecutively after which no significant influence to other directions than the one subjected to the force was found. It can be concluded that the force balance was assembled correctly and that all components were aligned.

3.2.6 Certus

To measure the orientation of the foil with respect to the carriage reference frame, Certus was used. This system works based on three infrared cameras, which interpolate the location of four infrared lights. The reference plate with these lights is mounted on the bottom plate of the 6DOF sensor as illustrated in figure 3.9.

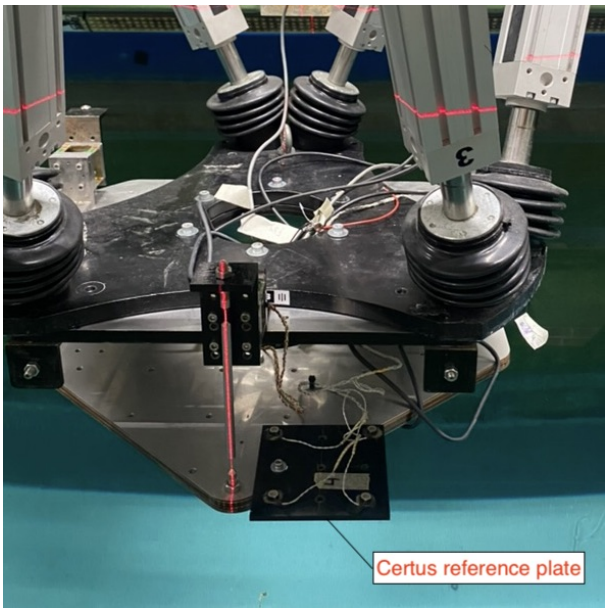

Figure 3.9: Certus reference plate

The translation from the measured location, which is the reference plate, to the foil reference frame will be explained in chapter 4. For the translation, the vector from the Certus reference frame to the foil reference frame is required. This vector was measured and equals: $\vec{Foil} - \vec{Certus} = [80,\ -280,\ -423.9]\ mm$.

The 6DOF sensor was calibrated before mounting. To calibrate the orientation of Certus, the pitch and yaw are defined first. This was done by placing the plate on a pole which stands on the bottom of the tank. By moving the carriage forward over a distance of $\pm$ 500 mm, a movement in the negative x-direction was measured. This defined the pitch and yaw-axis. Then, the roll-axis was defined by changing the location of the pole on the bottom of the tank. The reference plate should be located in the same x,y plane as the first measurement because the bottom of the tank is close to flat. A maximum misalignment of 5 mm on the wheels of the carriage can occur. Over a distance of 5 m, which is the distance between front and aft wheels, this can be translated to a maximum deviation of 0.1 °. The pole was moved over a distance of 300 mm, over which the bottom of the tank does not differ more than 0.5 mm from the water surface. That being the case, a maximum deviation of 0.1 ° on the roll axis is expected. As a result, the accuracy of the orientation can be assumed $\pm$ 0.1 ° in all axes.

The origin of the Certus reference frame was set when the rotations were zero and the foil reference frame coincided with the surface. The x and y position were chosen in such a way that the Hexapod was in its central position to allow for maximum freedom. Each day, the foil height was compensated by sight for water evaporation. Given that the evaporation remained constant at $0.5 - 1$ mm per day throughout the week, an accuracy of 0.5 mm can be assumed.

3.2.7 Wave sensors

To measure the wave height, three wave sensors were used, which are referred to as Whm. The first wave sensor was located at $x = 0$. This sensor provided accurate reading of the actual wave at the foil. The other two sensors were placed in front of the foil at $x = 1155$. Measuring the wave in front of the foil provides the foundation for a predictive control system as it provides time to find a description of the wave pattern and calculate the expected foil response.

The wave sensors were made by General Acoustics, the type is UltraLab ULS Advanced - Lab Wave Gauge. They do not require calibration and have the following specifications (Acoustics, n.d.):

Measurement range	$25,\ 35,\ 120\ cm$
Resolution	$0.18\ mm$
Sample rate	$100\ Hz$

3.2.8 Cameras

Multiple cameras were used during the experiments to capture disturbances. Two Nikon cameras capture the surface disturbance of the wake and the surface above the foil. A GoPro was used to capture effects on the top of the foil.

The first Nikon camera was placed behind the foil to check for lateral movement and to film the wake of the foil. Figure 3.10 shows a screenshot of this view.

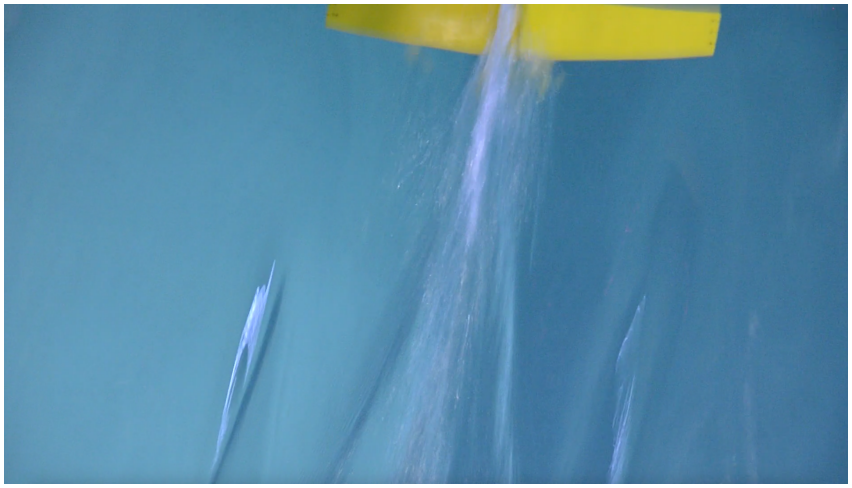

Figure 3.10: Nikon wake view of NACA 0012 T-foil

A second Nikon camera was used to provide side view. The camera suffered from vibrations which were solved throughout the duration of the experiments. It was employed to show the spray and bow wave induced by the foil. It could also check the submergence of the foil. Figure 3.11 shows a screenshot of this view.

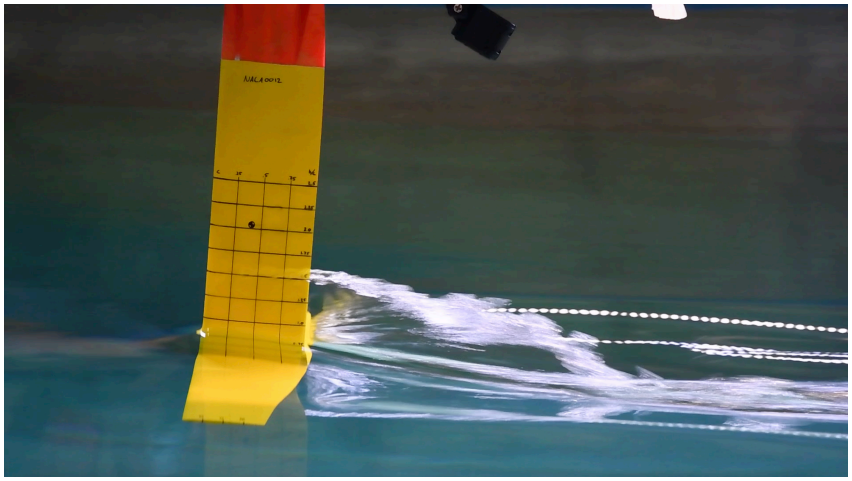

Figure 3.11: Nikon side view of NACA 0012 T-foil

Finally a GoPro camera was mounted on the bottom plate of the 6DOF. This camera provided a top view of the foil. Although it was less reliable for shape analyses, it captured local phenomena on the wing. Figure 3.12 shows a screenshot of this view.

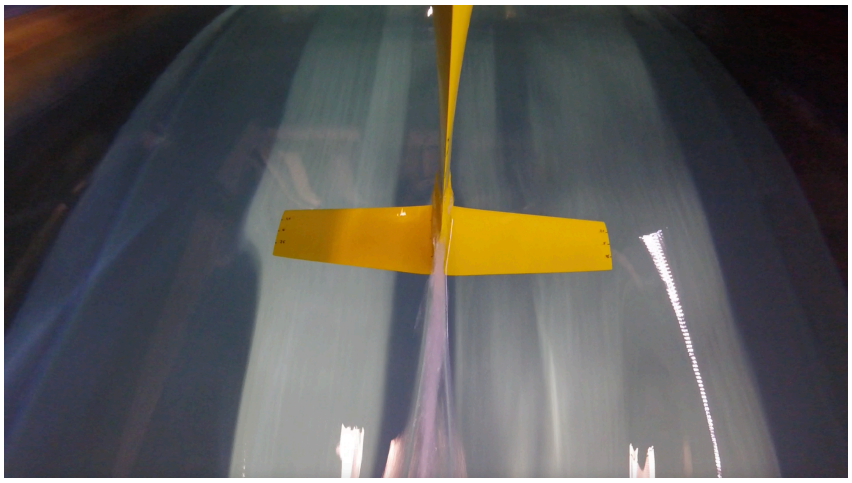

Figure 3.12: GoPro top view of NACA 0012 T-foil

3.2.9 Pecos signal conditioning

The strain in the gauges is quantified by the resistance which is measured by Pecos. The signal conditioner, named Pecos, interprets this into a Voltage between -10 and 10 V which is then sent to the measurement computer. The resistance in the gauges changes linearly with the force. The offset of this linear relation was zeroed each morning on the Pecos device.

The mass of the setup was not measured due to the zeroing. In section 4.4 the forces measured in the static experiments are used to make a surface function. Lacking the component of mass in this force vector, the resulting figures could not be explained.

A correction was made to all measurements to make these figures comprehensible. The mass of the setup below the 6DOF gauges was extracted from the forces in z-direction for all runs. The following equation was used:

$$\begin{bmatrix} F4Z \\ F5Z \\ F6Z \end{bmatrix}_{actual} \approx \begin{bmatrix} F4Z \\ F5Z \\ F6Z \end{bmatrix}_{measured} + \begin{bmatrix} 1/3 \\ 1/3 \\ 1/3 \end{bmatrix} m\,g \tag{3.15}$$

A mathematical study is presented to assure the influence on the compensated results is nil. For this, additional force notations were introduced. The total force on the setup during the experiments is referred to as F_{total} and can be written as the sum of two elements. The first element is the one of interest, namely the dynamic force due to lift and drag on the foil ($F_{dynamic}$). The second element is the static force which contains buoyancy, gravity and tensional forces within the 6DOF. This force is referred to as F_{static} and can be split in one part which is zeroed by the Pecos and another part which is either measured before a steady state experiment or extracted from the static function as will be explained in section 6.1.

$$F_{total} = F_{dynamic} + F_{static} \tag{3.16}$$

Due to the zeroing of Pecos, F_{static} can be written as:

$$F_{static} = F_{static-pecos} + F_{static-measured} \tag{3.17}$$

Equation 3.16 was rewritten in function of $F_{dynamic}$. Also equation 3.17 was included.

$$F_{dynamic} = F_{total} - F_{static} = F_{total} - (F_{static-pecos} + F_{static-measured}) \tag{3.18}$$

As a result of the zeroing of Pecos, the force measured is F_{6DOF}, which is F_{total} compensated by $F_{static-pecos}$.

$$F_{total} = F_{6DOF} + F_{static-pecos} \tag{3.19}$$

By replacing F_{total} in equation 3.18 by the result from equation 3.19, the following is found:

$$F_{dynamic} = F_{6DOF} + F_{static-pecos} - (F_{static-pecos} + F_{static-measured}) \tag{3.20}$$

The above equations hold when the orientation of all forces is equal. This is only the case if all rotations are zero. Therefore the equation is expanded with rotations and reference frames.

$$F^{global}_{dynamic} = R_{6DOF \to global}(F^{6DOF}_{6DOF} + F^{6DOF}_{static-pecos}) - R_{6DOF \to global}(F^{6DOF}_{static-pecos} - F^{6DOF}_{static-measured}) \tag{3.21}$$

With the introduction of equation 3.15, $F_{static-pecos}$ is added to both equation 3.17 and equation 3.19. $F_{static-pecos}$ in equation 3.21 is multiplied by the same rotational vector and expressed in the same reference frame so it can be eliminated from equation 3.21:

$$F^{global}_{dynamic} = R_{6DOF \to global}(F^{6DOF}_{6DOF} - F^{6DOF}_{static-measured}) \tag{3.22}$$

The above equation confirms that the zeroing of Pecos does not influence F_{hydro} regardless of rotations.

3.2.10 Measurement accuracy

This section will elaborate on the estimates of the measurement accuracy. An overview of the previously named estimates will be given in the following table.

Component	Calibration accuracy	Measurement accuracy
6DOF	1 N	$F_x = 1\ N$, $F_y = 2\ N$, $F_z = 3\ N$, $M_x = 0.6\ Nm$, $M_y = 0.52\ Nm$, $M_z = 0.4 Nm$
Certus	0.1 mm in x and y, 0.5 mm in z and 0.2 $^\circ$ in roll, pitch and yaw	0.001 mm
Carriage velocity	0.01 ms^{-1}	0.001 ms^{-1}
Wave sensor	0.01 mm	0.0001 mm

Looking at the accuracy of all the components, it can be assumed that the accuracy of the measurements falls within the range of the markers used in the graphs. This is confirmed in figure 6.4 where the lift coefficient is calculated using three methods.

3.3 Script for experiments

All test scenario's are described in the experimental test matrix. Table 3.1 provides an overview of the executed tests. The total test matrix can be found in appendix C.

Condition	$h/c[-]$	$AoA[^\circ]$	$v_\infty[ms^{-1}]$	**Goal**
				Calibration of the experimental setup
Steady state	0.5, 1, 1.5, 2, 2.5	-15 – 15	2	Characterisation NACA 0012
Steady state	0.25, 0.5, 1, 1.5, 2, 2.5	5	2, 4, 6	Characterisation NACA 0012
Steady state	1, 2, 2.5	5	2, 4, 6	Characterisation including yaw
Dynamic	0.25 – 2.5	5	2, 4, 6	Heave one way
Dynamic	2	-15 – 15	2, 4	Angle sweep one way
Dynamic	2	-8 – 8	6	Angle sweep one way
Dynamic	0.5 – 2.5	10 – -16, -10 – 16	2	Angle sweep both ways
Dynamic	0.5 – 2.5	10 – -13, -10 – 13	2	Stepped angle sweep both ways
Dynamic	1 ± 75 *mm*	5	2, 3	Sinusoidal heave
Dynamic	1	0 ± 8	2, 3	Sinusoidal pitch
Waves	1	5	2, 4, 6	Investigate relation ζ_a, v_∞ and ω
Steady state	2.5	$-15 - 15$	2	Characterisation NACA 0012 RAW
Steady state	0.5, 1, 1.5, 2, 2.5	5	2, 4, 6	Characterisation NACA 0012 RAW
None				Sinusoidal movements for inertia

Table 3.1: Test matrix

4 Preliminary calculations

This chapter will elaborate on the calculations made in order to make the experimental results usable and accessible for further analyses. To visualise the steps that were taken to transform the experimental data, the flowchart in figure 4.1 is created. The experimental data is gathered using the method described in chapter 3. After, the data is manipulated in the coloured rectangles. The plain hexagons represent input or output. In-consequences in the experiments are compensated in the first coloured box. Afterwards, the data is filtered and re-sampled to reduce measurement noise and to reduce the file size to allow for faster calculation. Plots from the resulting data are exported in pdf format to be able to quickly investigate filtered time traces. The next manipulation is the translation of reference system to the foil reference frame. The resulting time traces are exported and compared with the export from the filtered data. The next step is to calculate the results for the steady state experiments. These are discussed in chapter 5 where figures are presented showing the hydrodynamic properties in steady state conditions. Furthermore the hydrodynamic properties of this foil are compared to others.

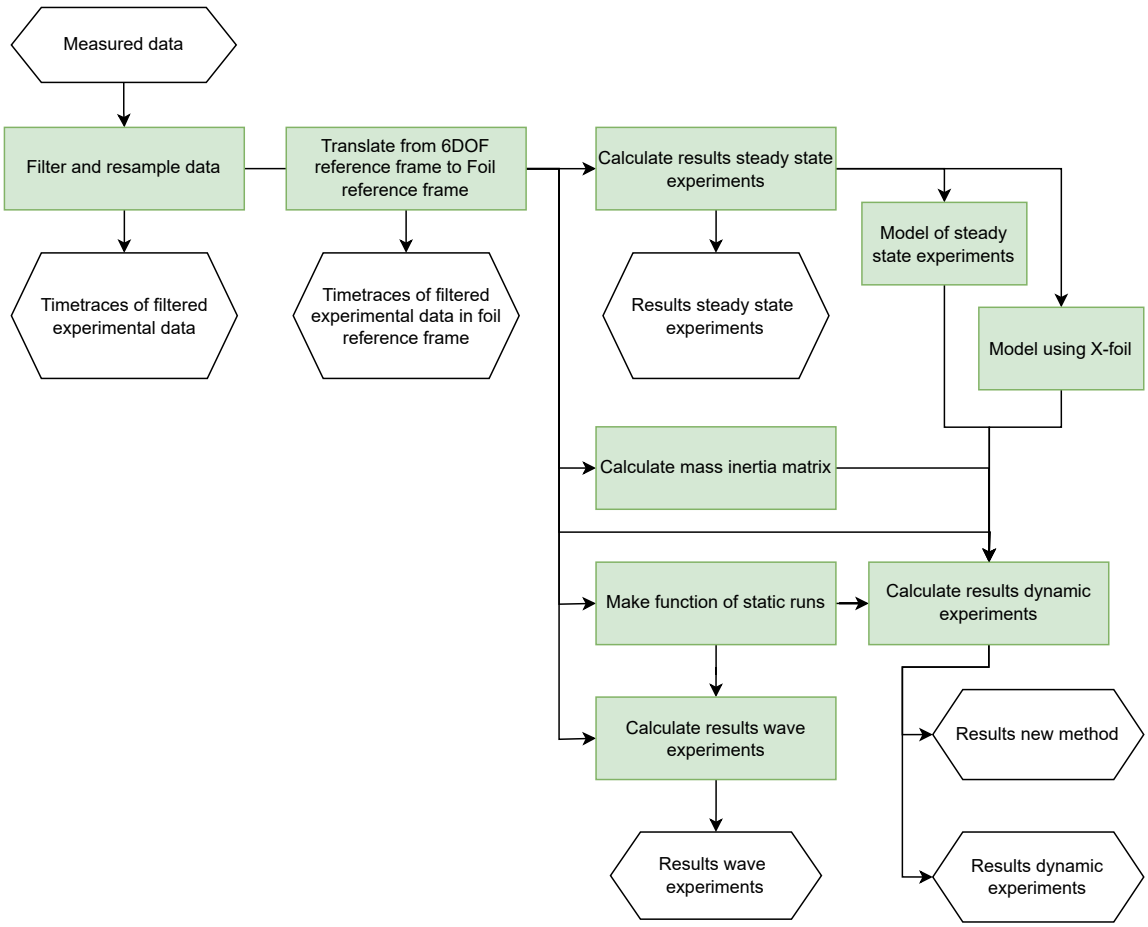

Figure 4.1: Flow chart overall process

For the calculations of dynamic experiments two compensations are required. The first is a mass inertia compensation. The second is a compensation for the hydro static and gravitational forces acting on the foil. With these components, the hydrodynamic results can be calculated. These are described in chapter 7. The final step is to calculate the results for the wave experiments which are presented in chapter 8.

4.1 Filtering and resampling

Phenomena occur at lower frequencies ($< 5Hz$), therefore the raw signal could be resampled to allow for faster calculation. Depending on the signal it was resampled from either 1000 Hz or 100 Hz to 20 Hz.

In section 2.4, the quality of the Savgol filter is compared against others. For the Savgol filter, highest smoothing without distorting the overall shape of the signal is expected. The settings used to filter the signal are depicted in table 4.1 for each raw signal. The setting of the window size was chosen as small as possible while removing spikes from the signal. The order was chosen as large as possible without creating strange behaviour in the signal. The derivative is not necessary and thus 0. Delta was calculated using the frequency of the signal of 20 Hz.

Measurement	Y-values	Window size	Order	Derivative	Delta
Force	$[F1X, F2Y, F3Y, F4Z, F5Z, F6Z]$	31	5	0	0.05
Location	$[x, y, z, roll, pitch, yaw]^{certus}$	31	5	0	0.05
Wave	$[Whm1, Whm2, Whm3]$	31	5	0	0.05

Table 4.1: Savgol filter settings for force, location and wave measurement

The velocity of the carriage is very constant. Therefore, it was decided not to filter the velocity. To amplify this statement a look the signal is investigated. On a run the signal shows a maximum deviation of 0.005 ms^{-1} which is thus considered very constant.

4.2 Translation and rotation

Translation and rotation of reference frames are required because several measurements are made in different locations. In figure 3.7, all reference frames are illustrated in a schematic drawing. In this figure a table is included, giving the location of the reference frames that are fixed to the foil frame.

4.2.1 Forces

The forces due to hydrodynamic effects are desired in the foil-global reference frame. As described in section 3.2.5, the 6DOF consists of six gauges. In section 4.1 the filtering of the data per gauge is described. After filtering, the forces measured by the gauges are combined using equation 3.12. The resulting force vector is described as follows: $F = [F_x,\ F_y,\ F_z,\ M_x,\ M_y,\ M_z]^{6DOF}$. To find the force vector in the foil-global frame, translation and rotation are required.

The first step in this process is to translate the forces and moments to the foil reference frame. The forces can easily be translated because they remain the same.

$$\begin{bmatrix} Fx \\ Fy \\ Fz \end{bmatrix}^{foil} = \begin{bmatrix} Fx \\ Fy \\ Fz \end{bmatrix}^{6DOF} \tag{4.1}$$

An additional moment due to the arm acting on the forces is added to the moments. For this $M = \vec{r} \times \vec{F}$ is applied in the following equation:

$$\begin{bmatrix} Mx \\ My \\ Mz \end{bmatrix}^{foil} = \begin{bmatrix} Mx \\ My \\ Mz \end{bmatrix}^{6DOF} + \begin{bmatrix} rx \\ ry \\ rz \end{bmatrix}^{foil}_{foil \to 6DOF} \times \begin{bmatrix} Fx \\ Fy \\ Fz \end{bmatrix}^{6DOF} \tag{4.2}$$

In this equation $r^{foil}_{foil\rightarrow 6DOF} = [0,0,488]\ mm$. This location vector is visualised in figure 3.7.

The forces are expressed in the foil axis system. Thus, the orientation of the forces still corresponds with the orientation of the foil. It is necessary to rotate the forces to the foil-global reference frame. To find the forces and moments the rotation matrix A discussed in section 2.5.3 are applied to the force vector:

$$\begin{bmatrix} Fx \\ Fy \\ Fz \end{bmatrix}^{foil\_global} = A(roll, pitch, yaw)^{carriage}_{6DOF} \cdot F^{foil} \tag{4.3}$$

$$\begin{bmatrix} Mx \\ My \\ Mz \end{bmatrix}^{foil\_global} = A(roll, pitch, yaw)^{carriage}_{6DOF} \cdot M^{foil} \tag{4.4}$$

4.2.2 Location

It was necessary to express the orientation of the foil with respect to the carriage reference frame. As described in section 3.2.6, the location and orientation of a reference plate were measured by Certus and expressed in the carriage reference frame.

The measured location by the Certus reference plate was zeroed when the foil frame coincided with the carriage reference frame. The actual position of the Certus reference frame should thus be compensated for the location of the Certus reference plate with respect to the origin of the carriage axis system. This vector equals: $T^{carriage}_{carriage\rightarrow certus} = [-78,\ 280,\ -424]\ mm$.

$$\begin{bmatrix} x_{certus} \\ y_{certus} \\ z_{certus} \end{bmatrix}^{carriage} = \begin{bmatrix} x_{certus\_measured} \\ y_{certus\_measured} \\ z_{certus\_measured} \end{bmatrix}^{carriage} + \begin{bmatrix} -78 \\ 280 \\ -424 \end{bmatrix}^{carriage}_{carriage\rightarrow certus} \cdot 10^{-3} \tag{4.5}$$

The Certus and foil reference frame are rigidly connected. Hence, the location and orientation of the foil frame can be expressed as a sum of the location of the Certus reference frame plus a translation. The translation vector from the foil to the Certus frame was available in the foil reference frame so a rotation was required. Using equation 2.32, leads to the following:

$$T^{carriage}_{certus\rightarrow foil} = A(Roll, Pitch, Yaw)^{carriage}_{foil} \cdot T^{foil}_{certus\rightarrow foil} = A(Roll, Pitch, Yaw)^{carriage}_{foil} \cdot \begin{bmatrix} 78 \\ -280 \\ 424 \end{bmatrix}^{foil}_{certus} \cdot 10^{-3} \tag{4.6}$$

Combining both translations from equation 4.5 and 4.6 results in the equation for the location of the foil reference frame with respect to the global reference frame:

$$\begin{bmatrix} x_{foil} \\ y_{foil} \\ z_{foil} \end{bmatrix}^{carriage} = \begin{bmatrix} x_{certus\_measured} \\ y_{certus\_measured} \\ z_{certus\_measured} \end{bmatrix}^{carriage} + \begin{bmatrix} -78 \\ 280 \\ -424 \end{bmatrix}^{carriage} \cdot 10^{-3} + A(Roll, Pitch, Yaw)^{carriage}_{foil} \cdot \begin{bmatrix} 78 \\ -280 \\ 424 \end{bmatrix}^{foil}_{certus} \cdot 10^{-3} \tag{4.7}$$

4.3 Velocity and acceleration

With the location of the foil calculated in the carriage reference frame, the velocity and acceleration could be derived directly. The derived function within the Savgol filter was used (section 2.4.2) because previously unrecognisable disturbances in the signal became visible after derivation. The following settings were chosen for the derivation and filtering of velocity and acceleration:

Variable	Y-values	Window size	Order	Derivative	Delta
velocity	$[x, y, z, roll, pitch, yaw]_{foil}$	5	2	1	0.05
acceleration	$[x, y, z, roll, pitch, yaw]_{foil}$	5	2	2	0.05

Table 4.2: Savgol filter settings for velocity and acceleration

It is necessary to mention that the location has been filtered and rotated prior to calculating the velocity and acceleration by derivation and a second filter. An alternative method would be to derive the velocity and acceleration in the Certus frame and rotate location, velocity and acceleration afterwards. It was decided to use the first method in order to minimise the computational steps and thus save time. The advantage of the second method is that the filter is applied directly to the signal. Investigation of the results of both methods pointed out that no major difference was found.

4.4 Function of static measu

Due to the geometry of the 6DOF and the foil which is mounted underneath, static forces due to gravity and buoyancy act on the load gauges. As a result, the static force changes as a function of the orientation of the hexapod. Conventional towing tank research subtracts these static forces from the measurements by using the following method: Before a run, a static run is made of which the average is then subtracted from the measurements. The static run is also referred to as "nullrun" because it is used to null the setup. In this thesis static run is used, as it measures the static forces acting on the foil. This method was applied to the steady state experiments. In the experiments, where dynamic behaviour was simulated by changing the hexapod its orientation during a run, another solution was required.

Before every steady state run, a conventional static run was made. These static runs were used to make a point cloud of the forces and moments in function of $pitch$ and h/c. Afterwards, a surface function was made, as introduced in section 2.5.2. The expectation for the h/c curve is first order. The expectation for the AoA curve is second order. To make sure all effects were captured a 2^{nd} order curve fit was chosen for both $pitch$ and h/c direction.

During a static run only gravity and buoyancy act on the setup. Since during the experiments only h/c and pitch were varied, it was anticipated that only Fz and My would change as a function of depth and pitch. The scatter plots of all static runs including the static function and R^2 value are given in figure 4.2.

After the compensation made in section 3.2.9, the static run figures correspond with the expectations. In figure 4.2, Fz decreases as the depth increases, due to increased buoyancy. Also, for both small and large angles of $pitch$, Fz decreases with the extra submerged volume of the strut. Figure 4.2, confirms the expectation that moments around the y-axis change as a result of changing forces in z-direction.

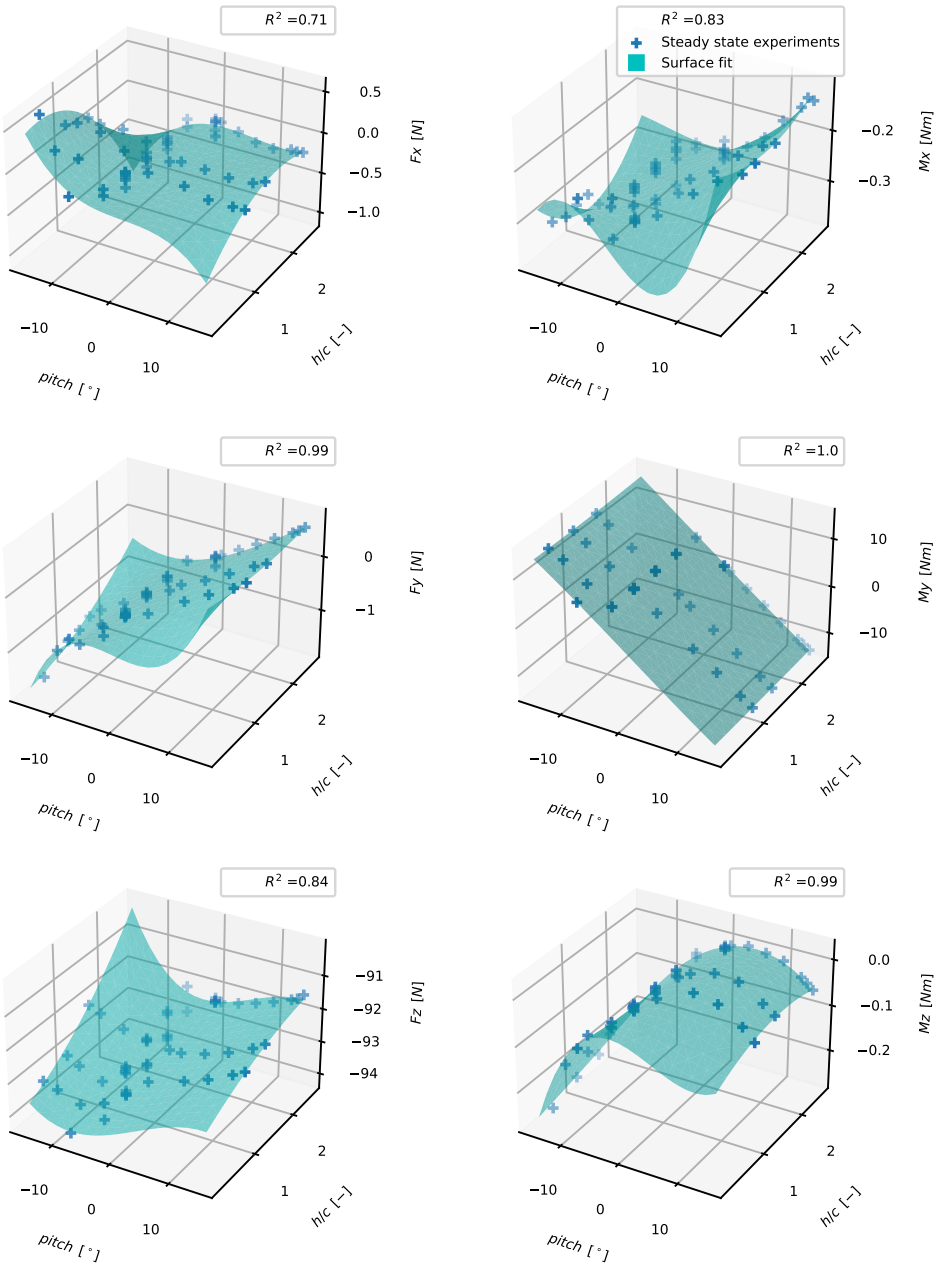

Figure 4.2: Static forces acting on setup in foil-global reference frame

4.5 Inertia analyses

During dynamic tests, the setup was accelerated to follow a prescribed motion. As a result of the acceleration, the force sensor was subjected to inertial forces. To compensate for these forces the mass and moment of inertia were calculated and used in further calculations. The weight of the setup underneath the load gauges was measured in the preparation of the experiments and was approximately 9.6 kg.

The method anticipated in order to calculate the inertia contribution, was to apply the following equation to each direction:

$$F = m\,a \;\rightarrow\; m = F\,a \tag{4.8}$$

Consequently, the setup has been subjected to sinusoidal motions above the water in each direction of the carriage reference frame. These motions could then be used to reverse engineer the mass (m) for each direction.

Another method was used because of its capability to take care of coupling and thus find the off-diagonal terms in the M-matrix depicted in equation 4.9.

$$\vec{F} = M\,\vec{a} \;\rightarrow\; M = \vec{F}\,\vec{a}^{-1} \tag{4.9}$$

The new method calculates the entire 6×6 inertia matrix (M). The least squares method was used because $\vec{a}$ and $\vec{F}$ contain numeral values for each component. All accelerations and resulting forces in the entire time domain of all movements were added. The resulting two $6 \times n$ vectors for $\vec{F}$ and $\vec{a}$ have the length of the domain of all movements together. Both sides of equation 4.9 were multiplied by $\vec{a}^T$. This resulted in the following equation:

$$\vec{F}\,\vec{a}^T = M\,\vec{a}\,\vec{a}^T \tag{4.10}$$

In this equation $\vec{F}\vec{a}^T$ and $\vec{a}\vec{a}^T$ are 6×6 matrices enabling to make the following step in the calculation:

$$M = \vec{F}\,\vec{a}^T\,\vec{a}\,\vec{a}^{T\,-1} \tag{4.11}$$

The resulting 6×6 inertia matrix M equals:

$$M = \begin{bmatrix} 9.0 & -5.4 \cdot 10^{-6} & 5.7 \cdot 10^{-5} & 1.9 \cdot 10^{-4} & 6.6 \cdot 10^{-2} & -2.0 \cdot 10^{-4} \\ -5.4 \cdot 10^{-6} & 8.3 & -2.7 \cdot 10^{-6} & 5.6 \cdot 10^{-2} & 9.7 \cdot 10^{-5} & -4.9 \cdot 10^{-4} \\ 5.7 \cdot 10^{-5} & -2.7 \cdot 10^{-6} & 1.1 \cdot 10 & -1.4 \cdot 10^{-4} & -3.0 \cdot 10^{-4} & 5.4 \cdot 10^{-6} \\ 1.9 \cdot 10^{-4} & 5.6 \cdot 10^{-2} & -1.4 \cdot 10^{-4} & -6.6 & 6.3 \cdot 10^{-5} & -9.2 \cdot 10^{-6} \\ 6.6 \cdot 10^{-2} & 9.7 \cdot 10^{-5} & -3.0 \cdot 10^{-4} & 6.3 \cdot 10^{-5} & -6.9 & 1.9 \cdot 10^{-5} \\ -2.0 \cdot 10^{-4} & -4.9 \cdot 10^{-4} & 5.4 \cdot 10^{-6} & -9.2 \cdot 10^{-6} & 1.9 \cdot 10^{-5} & 3.1 \cdot 10^{-1} \end{bmatrix} \tag{4.12}$$

At the diagonal of this matrix, a different mass was found for each direction. The expectation for the mass is 9.7 kg based on the weight of the elements. A difference of 2.7 kg occurs between the mass in y and z-direction which can be attributed to the geometry of the 6DOF. In figure 4.3 an attempt was made to clarify this. The red highlighted load gauges measure the forces in z-direction. However when a force in x or y-direction is applied, the bottom plate is free to bend and shear due to the steel support rod. The section in red will remain supported by only the z gauges and thus will not contribute to the mass in x and y direction.

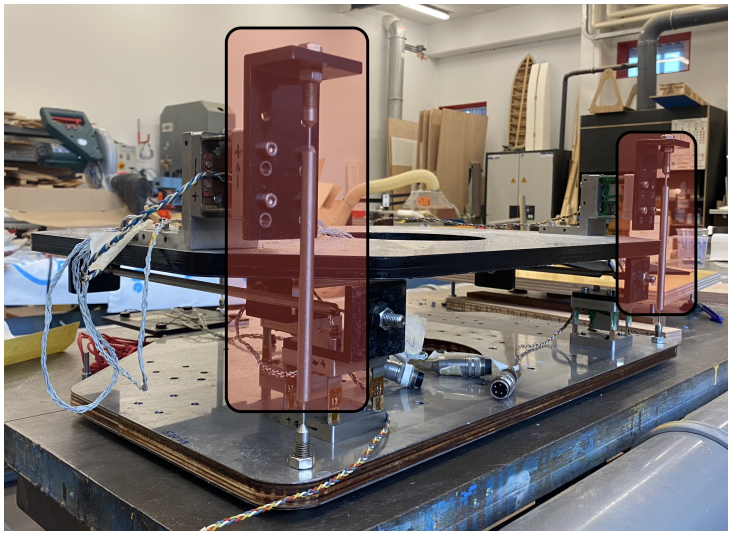

Figure 4.3: 6DOF mass

Verification of the inertial terms is more complicated. Rotating around the foil frame, the weight of the bottom plate of the 6DOF will be dominant for I_{xx} and I_{yy}. This is confirmed by the matrix. For I_{yy} the plate is again expected to be dominant due to its weight. However, due to the shorter arm, it is expected to be much smaller than I_{xx} and I_{zz}.

Figures showing the time trace of the motions, forces and calculated forces are included in appendix B. The forces are calculated using equation 4.9. In this equation the force is calculated in function of the found M matrix and the acceleration imposed to the setup. For the subjected motions good resemblance is found. The other forces can barely be predicted since the accelerations near zero.

5 Behaviour of NACA 0012 T-foil in steady state conditions

This chapter will elaborate on the first part of the experiments, namely the experiments in steady state conditions. Steady state conditions are simulated in experiments where the foil is towed through flat undisturbed water at a set velocity and orientation. First the calculation methods will be presented. Afterwards, the steady state results are discussed and compared to research in which a comparable setup was used.

5.1 Calculations

In figure 5.1, a flowchart provides an overview of the mathematical steps made to calculate the characteristics of the foils in steady state conditions. This flowchart fits in the "Calculate results steady state experiments" block of the overall flowchart presented in section 4.1. The flowchart is the foundation for section 5.1.1 which explains the blue elements and section 5.1.2 which discusses the yellow elements of the flowchart.

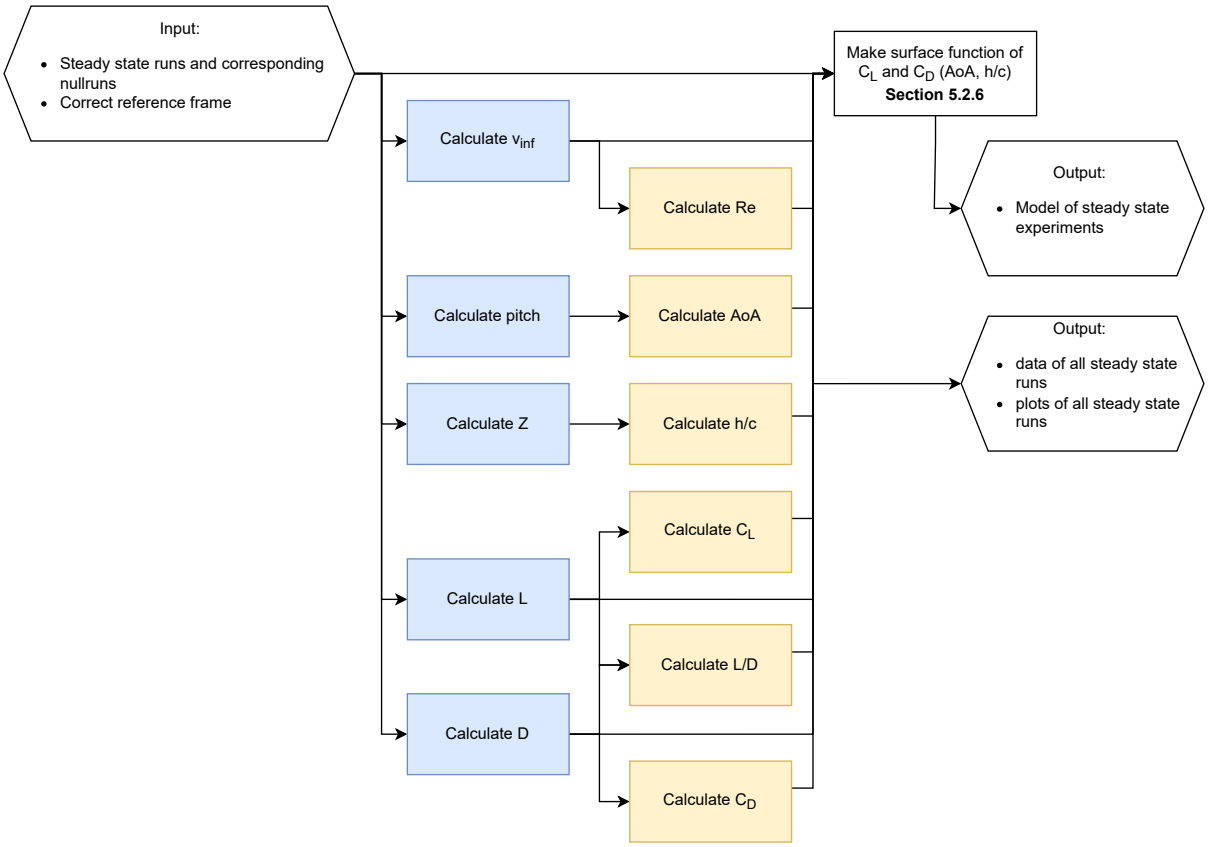

Figure 5.1: Flowchart of calculations for steady state conditions

5.1.1 Calculation of force, location and velocity from experiments

The characteristics were calculated using a traditional method applied to towing tank research. For every run, the average of the measurements was compensated with the average of a static run which was made before the run. This 30 s static measurement was made with the orientation of the foil identical to the run. After the run, the time domain was chosen such that velocity, forces and thus flow, were stabilised. From this domain, the average was taken. The mean of the static run was extracted to compensate for buoyancy and gravity. The results can then be attributed to hydrodynamic effects only. This method was applied to all mathematical manipulations highlighted in blue in figure 5.1 and calculates the velocity, pitch, height, lift and drag.

The velocity of the carriage equals the freestream velocity which can thus be obtained straight from the velocity signal. For steady state experiments, the stream velocity at the foil equals the freestream velocity.

5.1.2 Calculation of parameters and coefficients

With the velocity, pitch, height, lift and drag available from the blue elements presented in figure 5.1, the parameters and coefficients can be calculated using the elements highlighted in yellow.

From the velocity, the Reynolds number was calculated using equation 2.1. Where the kinematic viscosity (ν) at 18 $^\circ$ is $1.054 \cdot 10^{-6}\ m^2 s^{-1}$ and the mean chord length (c_m) is 80.5 mm as described in section 3.1. The resulting simplified equation for the Reynolds number holds:

$$Re = \frac{80.5\ \cdot 10^{-4}}{1.054\ \cdot 10^{-6}}\ v_\infty = 76.4\ v_\infty \tag{5.1}$$

The parameters AoA and h/c were calculated from the foil's position. The following equations were used:

$$AoA = -pitch^{foil-global} \tag{5.2}$$

$$h/c = -z^{foil-global}/c_m = -z^{foil-global}/0.0805 \tag{5.3}$$

The lift (L) and drag (D) were used to calculate the hydrodynamic coefficients C_L, C_D and L/D. C_L was calculated using equation 2.2, C_D was calculated using equation 2.3 and L/D was calculated by dividing the lift by the drag. In these equations $\rho = 1000\ kgm^{-3}$ and $A_{foil} = 32212\ mm^2$ as described in section 3.1.

Predictions from X-foil are used to compare the data. The calculation method of these predictions has been presented and elaborated in section 3.1.1.

5.2 Results

A full characterisation of the NACA 0012 foil, which was used for the research into foil behaviour in dynamic conditions, is presented. After, the resulting coefficients are compared to research where a similar foil was used. As exploratory research, the NACA 0012 foil was compared to a RAW 3D printed foil (NACA 0012 RAW) to study the effect of surface finish on the performance. The properties of both foils were discussed in section 3.1.

5.2.1 Hydrodynamic properties

This section presents the hydrodynamic properties of the T-foil in steady state conditions which are used as a reference for all further calculations. Figure 5.2 presents the lift coefficients versus the angle of attack, figure 5.3 the drag coefficients versus the angle of attack, figure 5.4 the lift over drag versus the angle of attack and figure 5.5 the lift coefficients versus the drag coefficients.

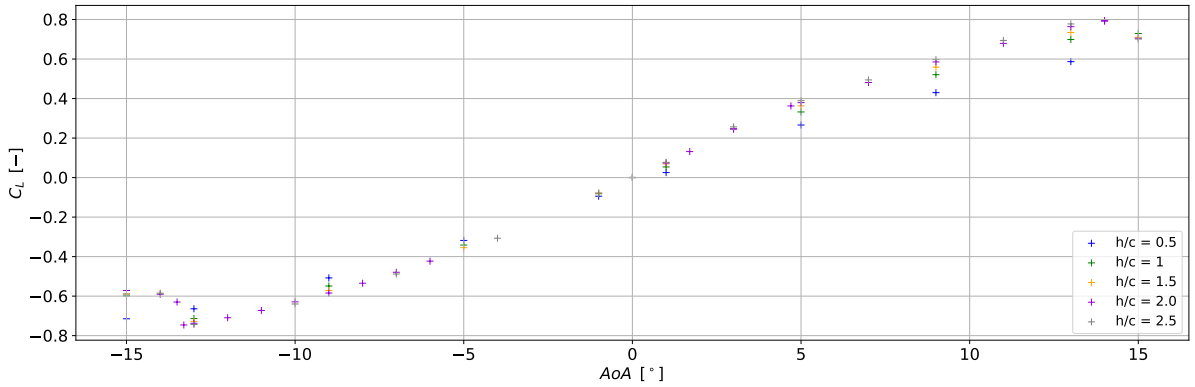

Figure 5.2: NACA 0012 T-foil ($AR = 5$) in steady state conditions, C_L vs. AoA at: $Re = 1.5$, $v_\infty = 2\ ms^{-1}$

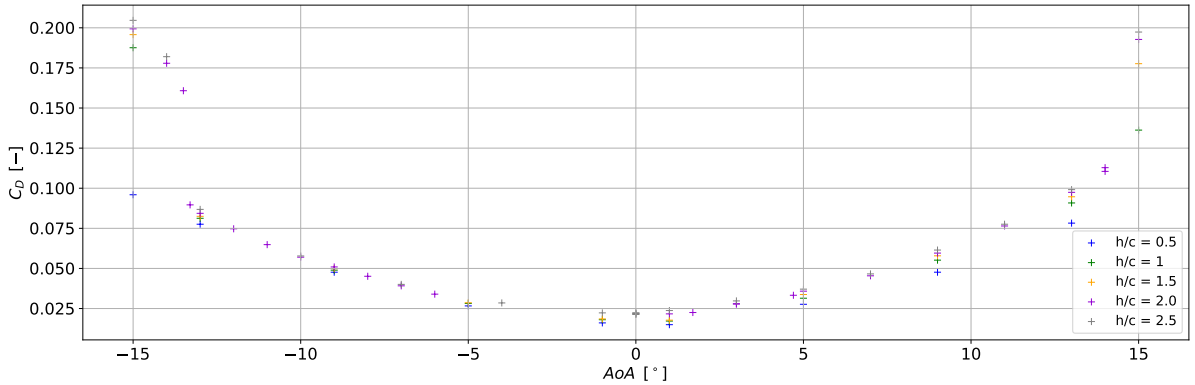

Figure 5.3: NACA 0012 T-foil ($AR = 5$) in steady state conditions C_D vs. AoA at: $Re = 1.5$, $v_\infty = 2\ ms^{-1}$

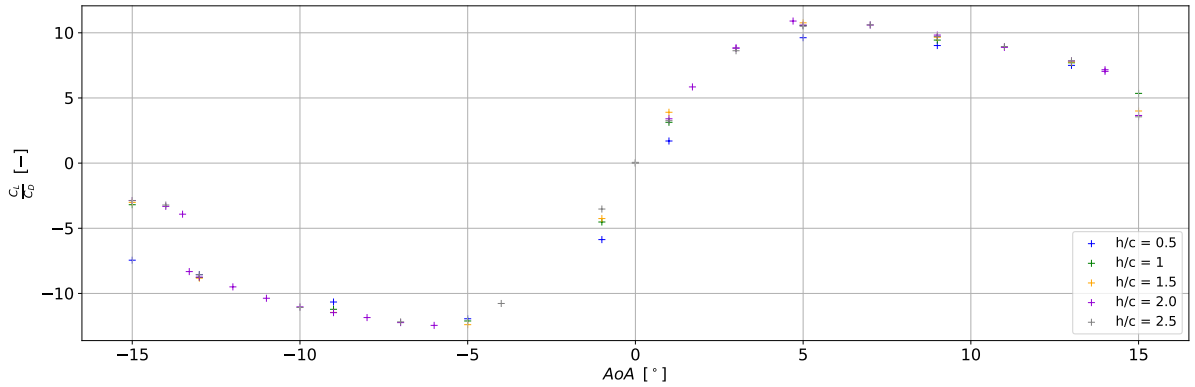

Figure 5.4: NACA 0012 T-foil ($AR = 5$) in steady state conditions C_L/C_D vs. AoA at: $Re = 1.5$, $v_\infty = 2\ ms^{-1}$

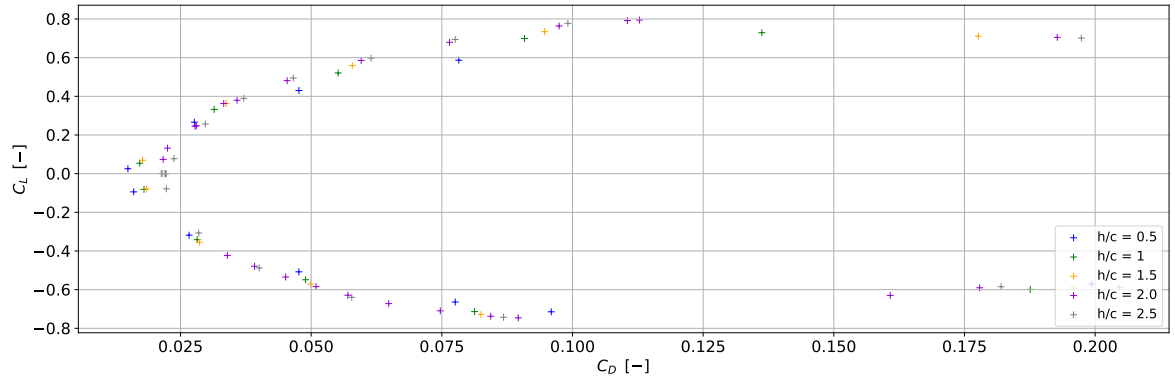

Figure 5.5: NACA 0012 T-foil ($AR = 5$) in steady state conditions C_L vs. C_D at: $Re = 1.5$, $v_\infty = 2\ ms^{-1}$

5.2.2 Comparison with initial force prediction

The initial force prediction made in section 3.1.1 was compared with the results from the experiments. In figure 3.5 the force prediction for 2 ms^{-1} and 6 ms^{-1} is shown for $h/c = 2.5$. Figure 5.6 shows the prediction and measurements in steady state conditions for lift and drag at 2 ms^{-1} and for $h/c = 2.5$. Both the experimental results and predictions are plotted in figure 5.6.

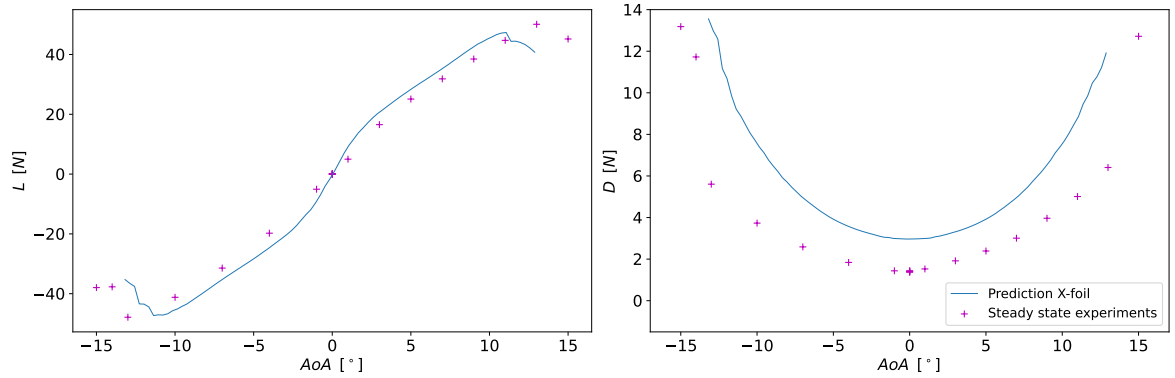

Figure 5.6: NACA 0012 T-foil ($AR = 5$) X-foil prediction vs. steady state experiments at: $h/c = 2.5$, $Re = 1.5$, $v_\infty = 2\ ms^{-1}$

The left graph in figure 5.6 shows the lift curve. A slight difference in stalling angle can be distinguished. No specific cause can be named due to it being such a small difference. Another difference can be distinguished by looking at the lift itself, the prediction of the lift is slightly higher. This difference can be attributed to free surface effects still acting at $h/c = 2.5$ for which no compensation was made in the prediction using X-foil. Also, the surface finish, which was idealised in the force prediction, influences the performance (Rawson & Tupper, 2001).

A more significant deviation can be distinguished when looking at the right graph of figure 5.6 showing the drag. The boundary layer transition point setting should be questioned for these results. All though research by Smith & Gamberoni (1956) suggested using an N_{crit} of 9, a smaller value would result in a lower curve for drag and thus a better fit for the actual measurements. This corresponds with research by Patterson & Binns (2021) which concluded $N_{crit} = 7$ and Drela (1998) which concluded $N_{crit} = 3$ corresponds best to experimental research. Also the prediction for drag due to the T-joint and spray contributes to the drag. The actual contribution might be lower due to the high course of sanding grid in which the foil was finished. Similar to the lift, the drag is expected to be influenced by surface effects. The asymmetry in the drag curve can be attributed to both the T-joint and the free surface effect.

In section 5.2.3, a method is proposed to compensate for the effects such as surface effect.

5.2.3 Comparison with existing data

Experiments by Binns et al. (2008) and Ashworth Briggs et al. (2018) were performed with a scaled version of the same T-foil. As described in section 2.1.2, foils with different dimensions can be compared using dimensionless coefficients C_L and C_D. From this point, it is chosen to use dimensionless coefficients as foils vary over various research. First the overall performance, then the influence of surface effect are compared. Finally, the influence of surface effect is compared for the prediction from X-foil.

Drag versus lift coefficient Binns

Figure 5.7 shows the results of the experiments undertaken in this study in conjunction with the results of the experiments by Binns et al. (2008).

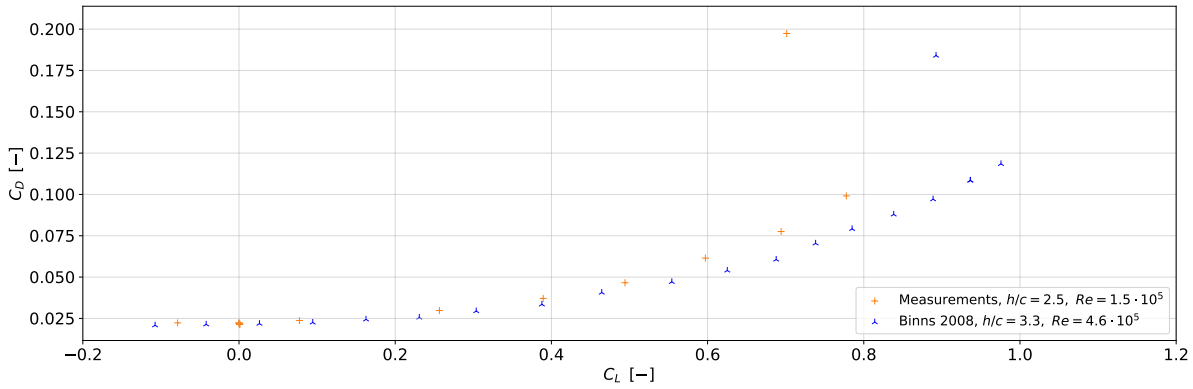

Figure 5.7: NACA 0012 T-foil ($AR = 5$) in steady state conditions C_D vs. C_L

Although dimensionless coefficients were used to compare the experimental results, the two scatters do not correspond perfectly. Binns experimented using a larger foil, at higher velocities and a higher Reynolds number. As described in section 2.1.1, results at a higher Reynolds number were expected to result in lower C_D vs. C_L. The influence is particularly large around the critical Reynolds number which was expected to lie somewhere around $4 - 4.5 \cdot 10^5$. Therefore a significant difference was expected for the results from Binns, in which the Reynolds number lies at $4.6 \cdot 10^5$. This hypothesis corresponds with the results. Finally, a small difference in surface effect was expected. In section 5.2.3 a method to compensate for the surface effect will be introduced. This method suggests that the difference equals 11 % for lift and $< 1\%$ for drag. This corresponds with the figure where the spread is relatively larger in C_L-direction.

Free surface effect by h/c Binns and Briggs

Figure 5.8 shows the results from the experiments, the results from Binns et al. (2008) and the results from Ashworth Briggs et al. (2018). Both were compared based on C_L and C_D vs. h/c.

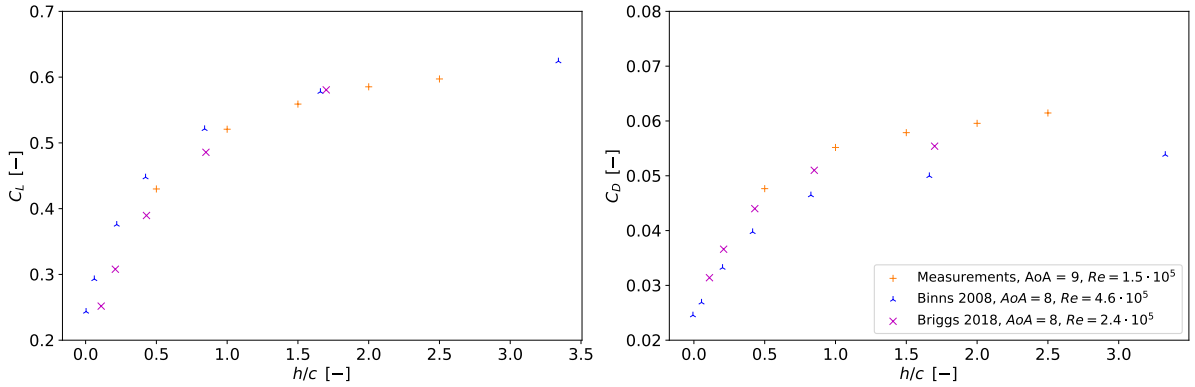

Figure 5.8: NACA 0012 T-foil ($AR = 5$) in steady state conditions C_L and C_D vs. h/c at: $AoA = 8\ ^\circ$& $9\ ^\circ$

Higher lift coefficients and lower drag coefficients were expected for both Binns and Briggs (Binns > Briggs), based on the Reynolds number. Experimental measurements were made at $AoA = 5\ ^\circ$ and $9\ ^\circ$, therefore experimental results for $AoA = 9\ ^\circ$ were plotted. Higher values were expected for both C_L and C_D as a result of this difference in angle of attack between the measurements and Binns and Briggs. It is interesting to note that the influence of the higher Reynolds number was larger at closer proximity to the surface.

Free surface proximity effect correction for X-foil

The calculation method for X-foil, as described in section 3.1.1, does not compensate for free surface proximity effects. As concluded from section 5.2.2, a correction would result in an enhancement of the prediction from X-foil. To amplify the influence of the surface effect, figure 5.9 shows the results from X-foil respectively to the experiments for various h/c, an angle of attack of 5 and $v_\infty = 2\ ms^{-1}$.

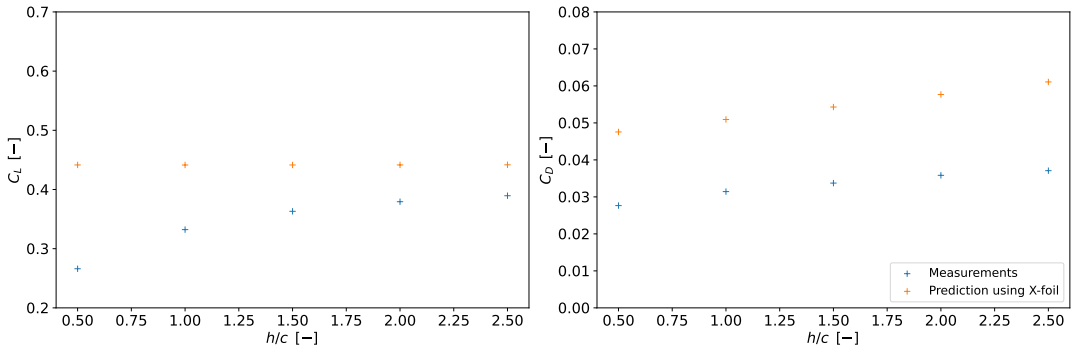

Figure 5.9: NACA 0012 T-foil ($AR = 5$) in steady state conditions C_L and C_D vs. h/c at: $AoA = 5\ ^\circ$, $Re = 1.5 \cdot 10^5$, $v_\infty = 2\ ms^{-1}$

Due to neglecting the free surface proximity effect, a large difference between $C_{L.measured}$ and $C_{L.xfoil}$ can be distinguished. A compensation is required because the prediction from X-foil is used in dynamic conditions in chapter 7. Patterson & Binns (2021) made a proposal for this correction by introducing the correction factor $K1$ which is discussed in section 5.2.3. For this research's application a slightly different approach was used. Instead of only compensating the sectional lift and drag as done in equation 2.14, the lift and drag coefficient compensated for 3D effects were compensated using the factor $K1$. It was decided to describe $K1$ as a function of h/c using the steady state results and steady state prediction from X-foil:

$$C_{measured} = K1(h/c)\ C_{xfoil} \rightarrow K1(h/c) = \frac{C_{measured}}{C_{xfoil}} \tag{5.4}$$

Equation 5.4 is applied to the results from figure 5.9. The results are illustrated in figure 5.10 for C_L and C_D.

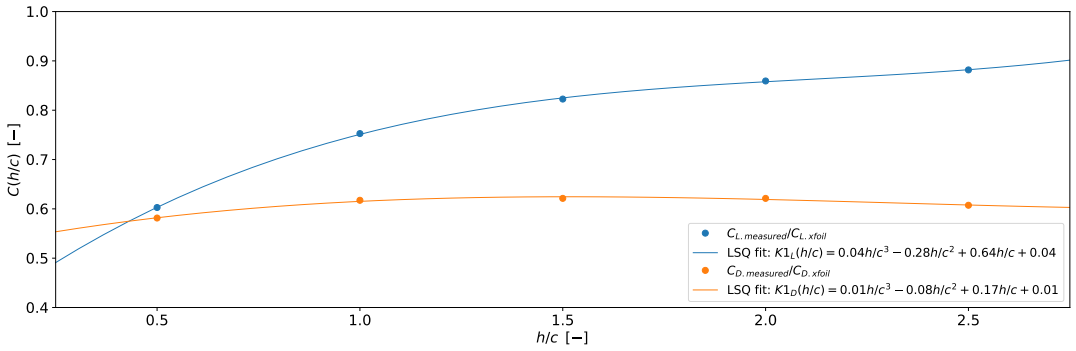

Figure 5.10: NACA 0012 T-foil ($AR = 5$) in steady state conditions $C_{h/c}$ vs. h/c at: $AoA = 5\,^\circ, AR = 5, Re = 1.5 \cdot 10^5$, $v_\infty = 2\ ms^{-1}$

A third order least squares fit was made, resulting in the following two functions for lift and drag.

$$K1_L = 0.044\ h/c^3 - 0.28\ h/c^2 + 0.64\ h/c + 0.35 \tag{5.5}$$

$$K1_D = 0.012\ h/c^3 - 0.08\ h/c^2 + 0.17\ h/c + 0.52 \tag{5.6}$$

Patterson & Binns (2021) found values for $K1_D$ of $1.2 - 1.5$ for $h/c = 3.33$. Using equation 5.6, the proposed method finds $K1_D = 0.6$. It is unclear where this difference comes from. It should be mentioned that this method creates a factor based on a mathematical and an experimental model. This method is preferred as it captures all differences which don't necessarily have to be attributed to free surface effects.

In chapter 7 the difference by Reynolds number is sought for. The above method leaves Reynolds number out of the equation since both inputs are given at the same Reynolds number. Consequently, this method is considered usable for the investigation of the influence of Reynolds number presented in chapter 7.

5.2.4 Model for steady state hydrodynamic coefficients

During the dynamic tests, h/c and AoA are changed over time. It is desirable to compare the results of the dynamic tests with the hydrodynamic properties of the hydrofoil in steady state conditions. Currently, only separate points are available for each run. Therefore, a surface function of the hydrodynamic properties C_L and C_D as a function of h/c and AoA is required. It was decided to make a 4^{th} order approximation in both the AoA-axis and the h/c-axis using the surface function as described in 2.5.2. The resulting plots for C_L and C_D are depicted in figure 5.11.

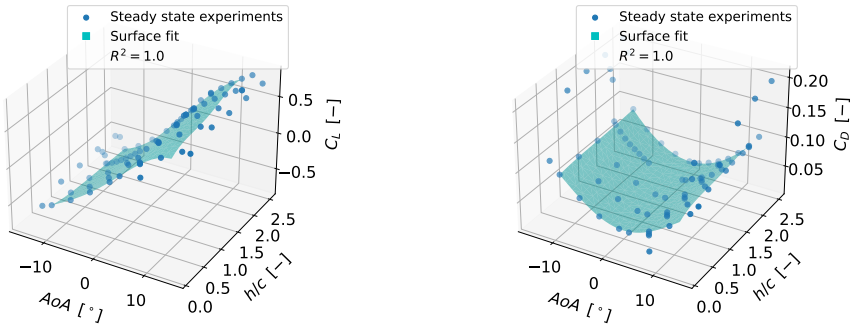

Figure 5.11: Model for steady state prediction at: $Re = 1.5 \cdot 10^5$, $v_\infty = 2\ ms^{-1}$

The resulting function for C_L and C_D can be used to interpolate steady state results. During dynamic tests, the angle of attack does not go outside the domain of $[-13, 13]$ °, hence the domain for the function fit was decreased in order to increase the quality of the fit. For dynamic experiments the angle of attack and submergence vary during a run. The calculation method is described in section 7.1.1 and allow the model to be used for prediction of dynamic experiments.

5.2.5 Comparison with NACA 0012 RAW

By conducting the same runs with both the NACA 0012 and NACA 0012 RAW, the influence of the surface finish can be investigated. It was decided to use a RAW finish because the foils of the HEARP are also RAW 3D printed. This way, an idea of the performance difference was created. As discussed in the introduction, surface finish was expected to make a difference in terms of ventilation. Although the test were not run in the ventilation regime, the influence on the turbulence was expected to be interesting. The steady state results of the NACA 0012 RAW foil were calculated similar to that of the normal NACA 0012 foil. In this section both results are compared and the influence of surface finish is discussed.

Figure 5.12 shows the foil characteristics for changing angle of attack at a submergence of $h/c = 2.5$. To compare the two foils with other foils, the characteristics are presented in coefficients C_L and C_D. The Reynolds number for these experiments is $1.5 \cdot 10^5$.

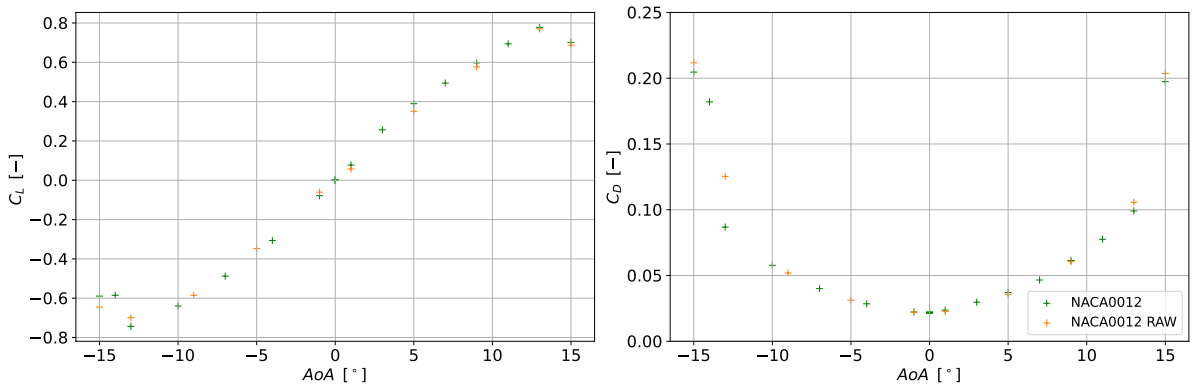

Figure 5.12: Foil characteristics NACA 0012 vs. NACA 0012 RAW at: $h/c = 2.5$, $Re = 1.5 \cdot 10^5$, $v_\infty = 2\ ms^{-1}$

A small advantage in C_L can be distinguished for the finished foil. However, the difference between the two foils is not significant.

Figure 5.13 shows the influence of h/c for different Reynolds numbers. Now, a clear difference can be distinguished.

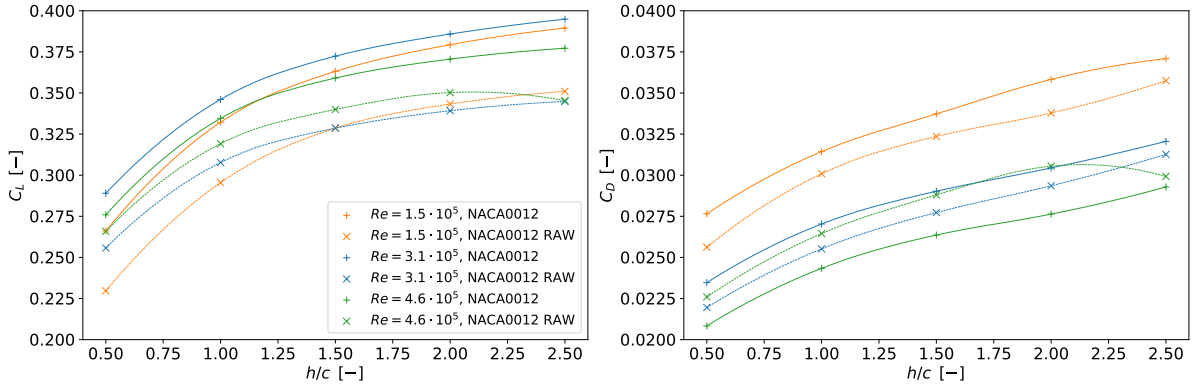

Figure 5.13: NACA 0012 vs. NACA 0012 RAW function fits for coefficients vs. h/c for various Reynolds numbers at: $AoA = 5$ °

To amplify the effect of the Reynolds number a plot of C_L and C_D vs. the Reynolds number is made and depicted in figure 5.14

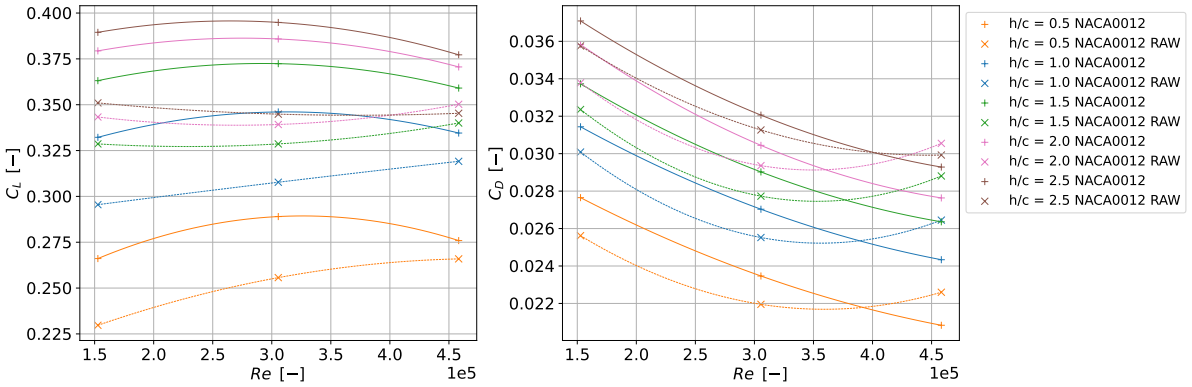

Figure 5.14: NACA 0012 vs. NACA 0012 RAW function fits for coefficients vs. Reynolds numbers at: $AoA = 5\ ^\circ$

While C_L still increases for the finished foil, C_L for the RAW foil decreases for higher Reynolds numbers. In the graph of C_D a similar effect can be seen. Where C_D is still decreasing for the finished foil, C_D for the RAW foil increases rapidly above $Re \approx 3.8$. This indicates a change in the flow conditions for the RAW foil, while the other foil still behaves normally. It can therefore be expected that the critical Reynolds number for the RAW foil lies in the region of $Re = 3.5 \cdot 10^5$. With the critical Re for a flat plate being $5 \cdot 10^5$ according to Rawson & Tupper (2001), it can be expected that the finished foil will show a similar change in properties when Re is increased above $Re = 4.5 \cdot 10^5$.

6 Changing orientation for faster foil characterisation

The experimental setup has been designed to oscillate the foil during experiments which allows for the investigation of a new method to determine steady state foil behaviour. This research's hypothesis is that high rates of change will result in delayed establishment of wake vorticity which will be discussed in the next chapter 7. At decreasing rate of change, the steady state behaviour is approached. This chapter questions the point where sufficient convergence is found and discusses two methods based on these findings. First the calculation method to find the hydrodynamic forces on the foil during a movement is discussed. This method is the mathematical foundation for this and the next two chapters. After, two new approaches to characterise the hydrodynamic performance of hydrofoils will be introduced and reviewed using the steady state results.

6.1 Calculation

The flowchart in figure 6.1 provides an overview of the preparatory calculations used for the analyses of the dynamic conditions. This flowchart fits in "Calculate results dynamic experiments" box presented in figure 4.1.

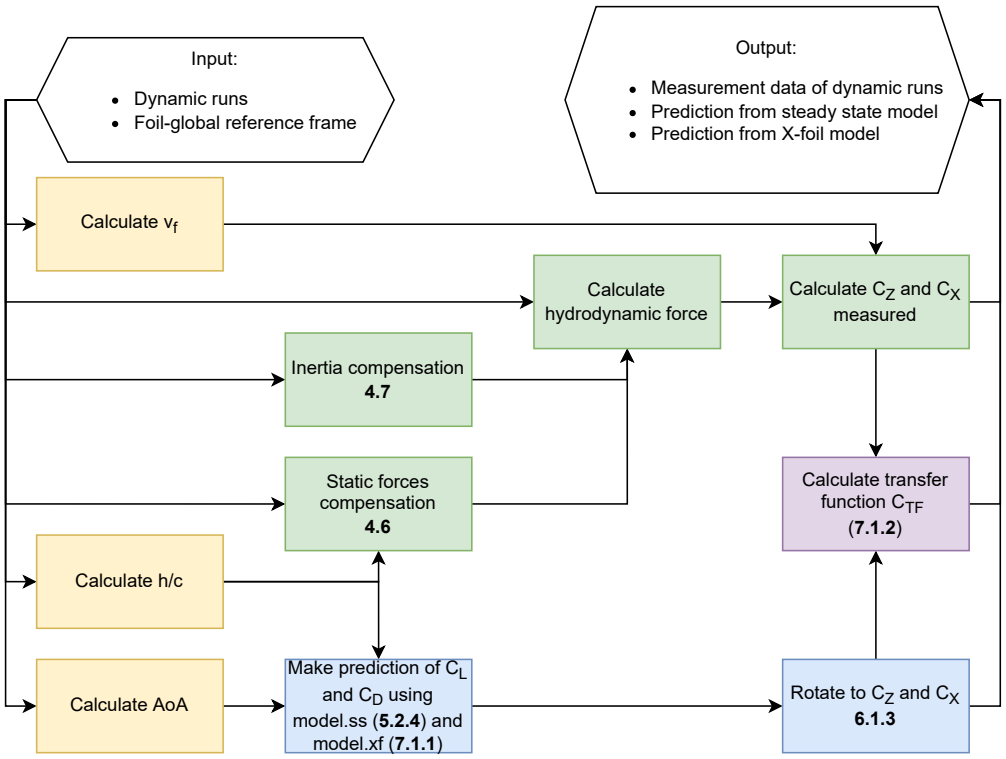

Figure 6.1: Flowchart of calculations dynamic conditions

For the dynamic analyses, the calculations were made for every step in the time domain of a run. This was done for all runs in which the orientation was changed during the experiment. The calculation of the desired parameters and coefficients will be discussed in the following paragraphs.

6.1.1 Preliminary calculations

In the next paragraphs changing foil properties are applied in functions and equations. The flowchart in figure 6.1 shows these properties highlighted in yellow. The static function described in section 4.4 uses h/c and AoA as input. In dynamic conditions the AoA and h/c change during the movement, so this is the first step in the calculations.

$$h/c = -z_{foil}/c \tag{6.1}$$

$$AoA = \alpha_{imposed} - \alpha_{motion} \tag{6.2}$$

α_{motion} equals the induced flow angle due to the motion of the foil. A vector representation of the calculation of α_{motion} is shown in figure 6.2. This figure explains how the freestream velocity (v_∞) and the flow due to the motion, which is opposite to the motion of the foil, influence the angle of attack and stream velocity at the foil. In this figure the change from imposed velocity to stream velocity at foil is made by drawing the arrows against the direction of the coordinate system.

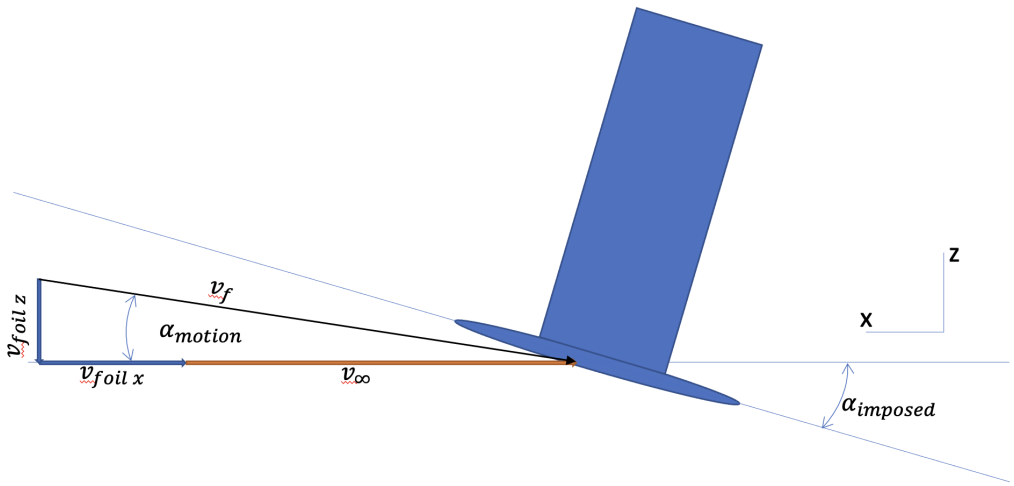

$$\alpha_{motion} = \tan^{-1}\left(\frac{v_{foil\,z}}{v_{foil\,x} + v_\infty}\right) \qquad v_f = \sqrt{v_{foil\,z}^2 + \left(v_{foil\,x} + v_\infty\right)^2}$$

Figure 6.2: Calculation of v_f and α_{motion}

In dynamic conditions, the angle of attack is not equal to the imposed angle ($\alpha_{imposed}$). This angle is introduced to comply with hydrodynamic conventions where the angle of attack is defined positive when the lift is pointing upwards.

$$\alpha_{imposed} = -pitch_{foil} \tag{6.3}$$

From the figure, the equations for α_{motion}, v_f and AoA can be derived. α_{motion} is derived using the law of tangents:

$$\alpha_{motion} = \tan^{-1}\frac{v_{foilz}}{v_{foilx} + v_\infty} \tag{6.4}$$

Using Pythagoras, the stream velocity at the foil is derived from the schematic representation given in figure 8.2:

$$v_f = \sqrt{(v_{foilx} + v_\infty)^2 + v_{foilz}^2} \tag{6.5}$$

With α_{wave} and the imposed angle known, the AoA is calculated using equation 6.2.

6.1.2 Force in x and z-direction compensated for buoyancy and inertia

The forces measured by the 6DOF sensor were compensated for the weight and buoyancy of the setup. Also, the inertia influence of the movement required to be taken into account. The compensation was calculated for every time step, so that the entire motion was compensated for correctly. In the flowchart presented in figure 6.1 these steps are highlighted in green.

Depending on the orientation, the measurement of the static run changes. In section 4.4 the source and construction of the static function is explained. Using h/c and AoA as an input of this static function, the value of the compensation for gravity and buoyancy can be calculated for every time step.

To calculate the force due to the movement, the inertia matrix M calculated in section 4.5, is used in Newton's second law:

$$\vec{F} = M\,\vec{a} \tag{6.6}$$

With all the components available the actual force caused by hydrodynamic force can be calculated:

$$F_{z.measured} = F_{z.sensor} - F_{z.staticfunc}(h/c,\, AoA) - F_{z.inertia} \tag{6.7}$$

$$F_{x.measured} = F_{x.sensor} - F_{x.staticfunc}(h/c,\, AoA) - F_{x.inertia} \tag{6.8}$$

The forces are made dimensionless using equations 2.3 and 2.2. It was decided that calculating the forces in the direction of the global coordinate system provided a better understanding of the forces acting on the vessel. Whereas the commonly used C_L and C_D, which are perpendicular and tangential to the flow direction, would be changing direction for each time step due to the induced angle of attack caused by the motion of the foil. Note that for steady state conditions, where the foil does not move, $C_L = C_Z$ and $C_D = -C_X$.

$$C_{Z.measured} = \frac{2\,F_{z.measured}}{v_f^2\,\rho\,A_{foil}} \tag{6.9}$$

$$C_{X.measured} = \frac{2\,F_{x.measured}}{v_f^2\,\rho\,A_{foil}} \tag{6.10}$$

During the simulations of dynamic conditions, the foil was induced to a motion. As a result the stream velocity at the foil (v_f) had to be compensated. The calculation of this compensation is explained in equation 2.25 and figure 6.2.

6.2 Results

For the experiments into dynamic conditions, it was necessary to move the foil during the tests. From this requirement, the idea of characterising the hydrofoil by changing its orientation during a run arose. In this chapter two approaches for characterising the hydrodynamic performance of hydrofoils will be introduced and reviewed. As described in section 3.2.4, the foil is rotated around the centre of the horizontal. As a result the foil horizontal is solely subjected to rotation.

The first approach was a stepwise angle change. From these findings, an experiment into the effect of the rate of change during an angle sweep was investigated and is illustrated in figure 6.9. Then, the second approach which was a positive and a negative continuous angle sweep, was used to describe the hydrodynamic performance of the hydrofoil for a set of different h/c settings.

6.2.1 Changing angle of attack stepwise

Figure 6.4, 6.5, 6.6 and 6.7 present the results for the stepwise angle sweeps for $h/c = 0.5$ and 1.5. To prevent turbulent flow remaining attached to the foil, the experiment for the positive run was started at an angle of attack of -11 °. Next, the foil was held in position for 3 s at $AoA = [-11,\ -9,\ -5,\ 0,\ 5,\ 9,\ 11,\ 13]$ °. The time to change the settings was 2 s. For the negative stepwise sweep the exact opposite was done, resulting in $AoA = [11,\ 9,\ 5,\ 0,\ -5,\ -9,\ -11,\ -13]$ °. This is presented in figure 6.3.

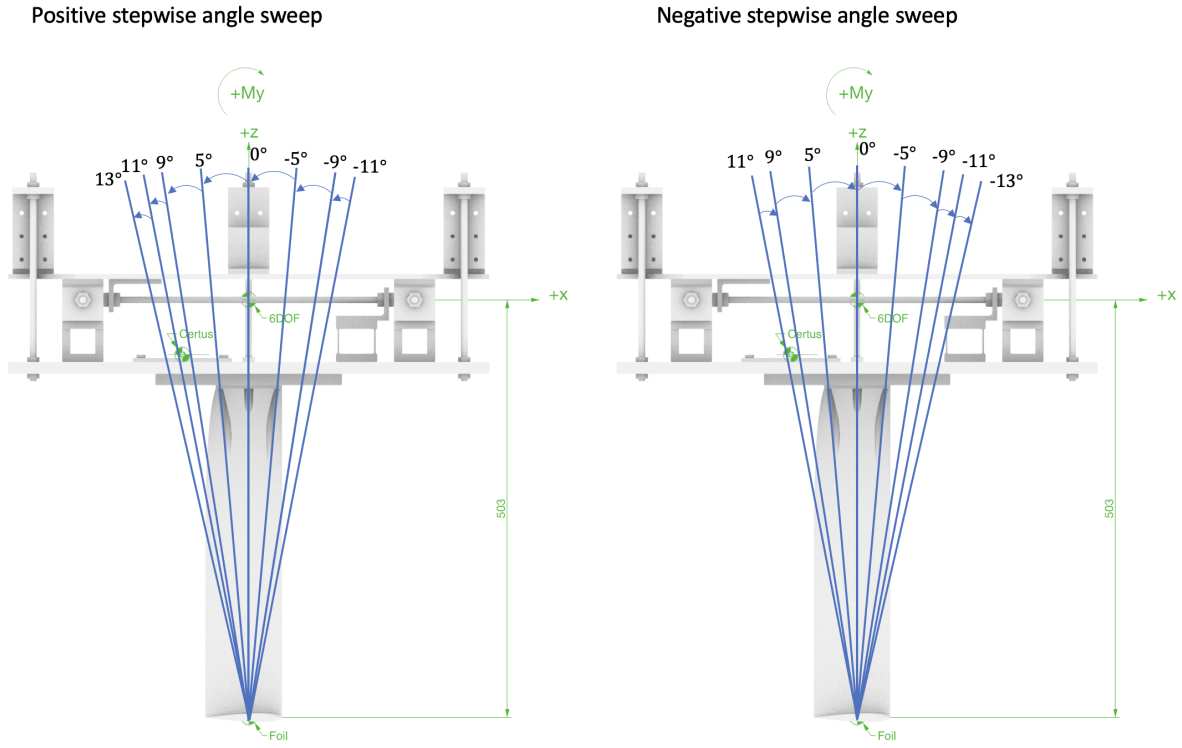

Figure 6.3: Illustration of stepwise angle sweep

The steady state results are plotted using + markers in the figures below. Translucent dot markers are used for each data point from the stepwise angle sweep where the absolute angular velocity is smaller than 0.001 $rads^{-1}$. The entire stepwise angle change is plotted using a thin line to amplify the effect of the motion.

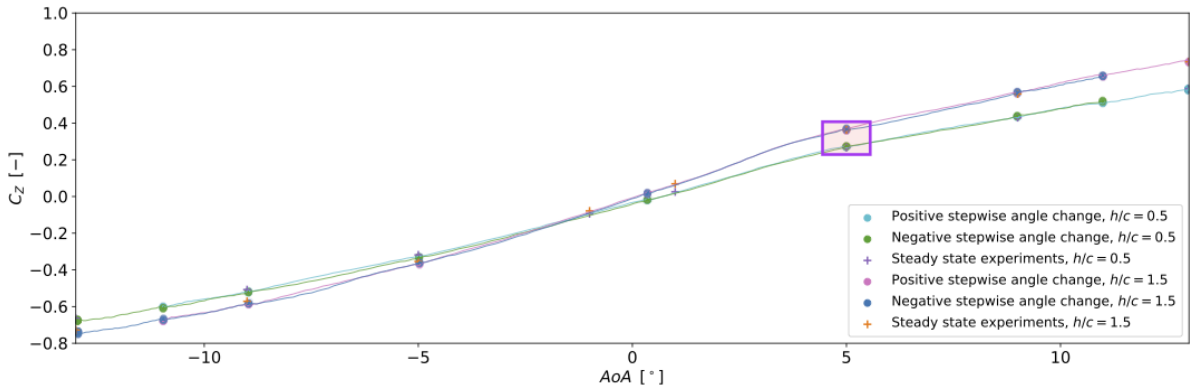

Figure 6.4: NACA 0012 T-foil ($AR = 5$), stepwise angle change $C_L = C_Z$ at $Re = 1.5 \cdot 10^5$, $v_\infty = 2\ ms^{-1}$

Figure 6.4 shows the results for the coefficient in z-direction for $h/c = 0.5$ and 1.5. $C_L = C_Z$ and $C_D = -C_X$ because there are no translations. The points from the experiments in steady state conditions comply with the results from the stepwise angle change. Figure 6.5 shows a zoomed version of figure 6.4 to amplify the method. In this figure the origin of the dots in figure 6.4 becomes clear. Each data point that complies with the criteria that the angular velocity is smaller than 0.001 $rads^{-1}$, is assigned with an translucent dot. The many dots in the same spot form the dots in figure 6.4. This way, the size of the dots directly relates to the certainty of the found point. This method is amplified in figure 6.5 where a zoomed version of figure 6.4 is given. An overview of the results for $h/c = 0.5$ is given in table 6.1

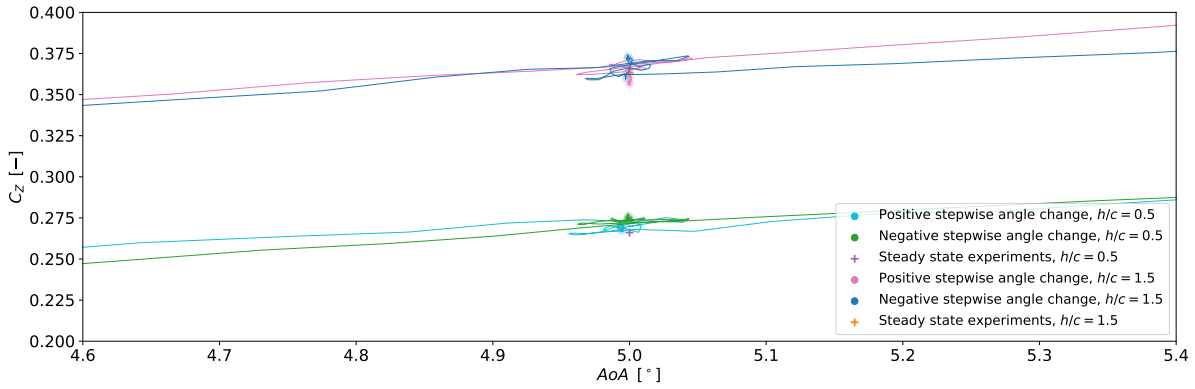

Figure 6.5: NACA 0012 T-foil ($AR = 5$), stepwise angle change $C_L = C_Z$ at $Re = 1.5 \cdot 10^5$, $v_\infty = 2\ ms^{-1}$

Even though a relatively short movement interval of 2 s was used between the pitch settings, the two plotted lines lie surprisingly close to each other. Larger separation of these lines was expected, due to the hypothesis that wake vorticity and thus induced angle of attack would lag the actual position of the foil. This led to further examination of the effects of flow settlement in a continuous angle sweep in section 6.2.2.

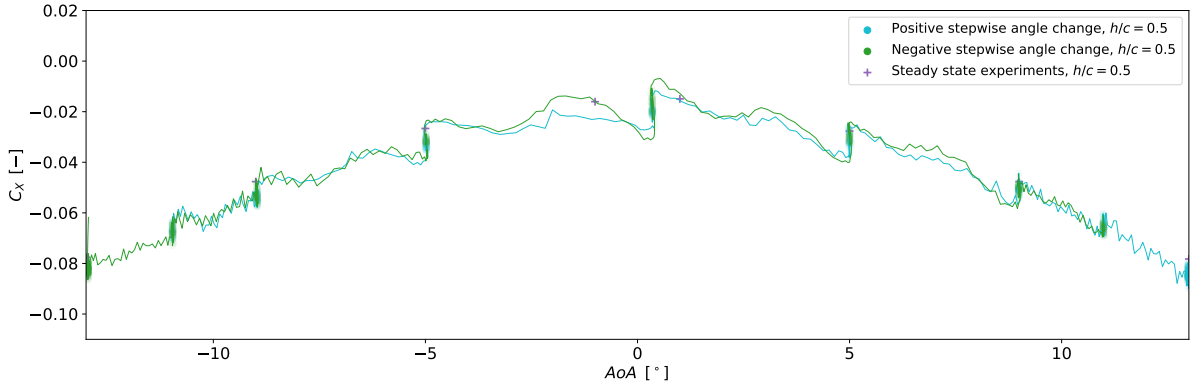

Figure 6.6: NACA 0012 T-foil ($AR = 5$), stepwise angle change $C_D = -C_X$ at $h/c = 0.5$, $Re = 1.5 \cdot 10^5$ and $v_\infty = 2\ ms^{-1}$

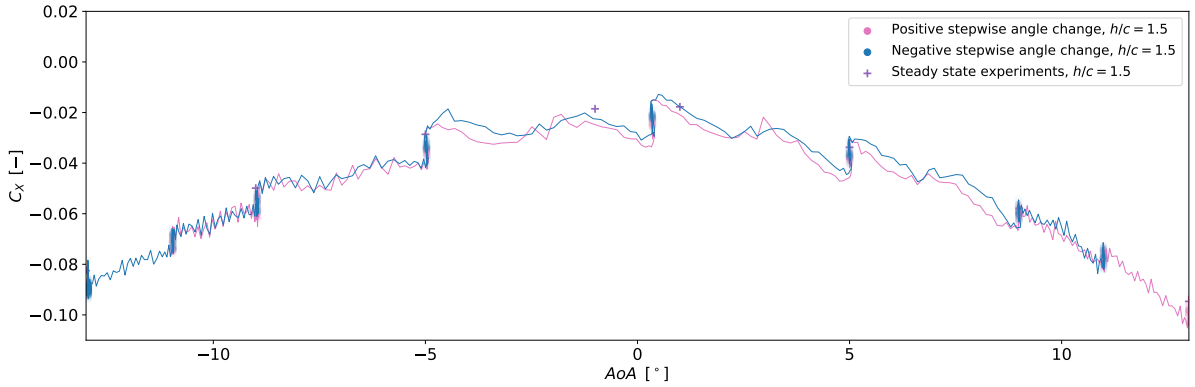

Figure 6.7: NACA 0012 T-foil ($AR = 5$), stepwise angle change $C_D = -C_X$ at $h/c = 1.5$, $Re = 1.5 \cdot 10^5$ and $v_\infty = 2\ ms^{-1}$

The stepwise angle sweeps show less distinct results for the drag coefficient in figure 6.6 and figure 6.7 where $h/c = 0.5$ and 1.5 respectively. As a result of the wake vorticity it can be expected that the induced drag, introduced in section 2.2.2, changes significantly. A continuous angle sweep would be more appropriate to reduce this effect because this would reduce sudden changes leading to unsteady vorticity. Also, it should be mentioned that forces in a range of 0.5 N to 4.5 N are measured. This means that measurements are made in a small region of the measurement domain, leading to increased noise in the signal.

An overview of the results and their range is given in 6.1. In this table the mean value of all the point cloud is given. The range is the distance between the highest value and lowest value of C_L in the point cloud. The results are given for each angle of attack.

	$h/c = 0.5$				$h/c = 1.5$			
AoA	$C_{L.stepwise}$	range	$C_{D.stepwise}$	range	$C_{L.stepwise}$	range	$C_{D.stepwise}$	range
-11	-0.61	0.022	-0.067	0.010	-0.67	0.045	-0.071	0.007
-9	-0.52	0.015	-0.054	0.010	-0.58	0.045	-0.056	0.006
-5	-0.33	0.011	-0.032	0.012	-0.36	0.019	-0.035	0.010
0	-0.02	0.010	-0.019	0.015	0.02	0.048	-0.023	0.008
5	0.27	0.012	-0.031	0.012	0.36	0.109	-0.037	0.007
9	0.44	0.014	-0.051	0.010	0.57	0.145	-0.060	0.001
11	0.52	0.021	-0.066	0.009	0.66	0.159	-0.077	0.003

Table 6.1: Hydrodynamic coefficients based on stepwise angle change for NACA 0012 T-foil ($AR = 5$), $h/c = 0.5$ and $v_\infty = 2$

From the results, it can be concluded that a relatively high accuracy is achieved.

6.2.2 Influence of changing rate on coefficients during angle sweep (AoA)

The results from figure 6.4 were promising in terms of flow stabilisation during movement causing the influence of the rate of angle change ($\frac{dAoA}{dt}$) to be examined in figure 6.9. It was expected that, at lower angular velocity, the plots would converge. Figure 6.8 illustrates the imposed motion to the foil. The foil rotates around the foil reference frame which corresponds with the centre of the horizontal.

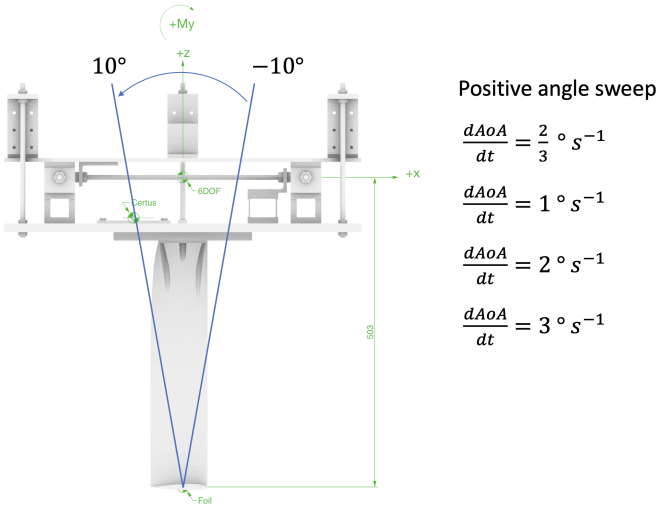

Figure 6.8: Illustration of positive angle sweep

Limited by the capabilities of the hexapod, periods of 5, 10, 20 and 30 s were investigated. In these periods the foil made a positive angle sweep from $-10\,^\circ$ to $10\,^\circ$ angle of attack which corresponds to a rate of change of $[4,\ 2,\ 1,\ 2/3]\,^\circ s^{-1}$. The results of these experiments are shown in figure 6.9.

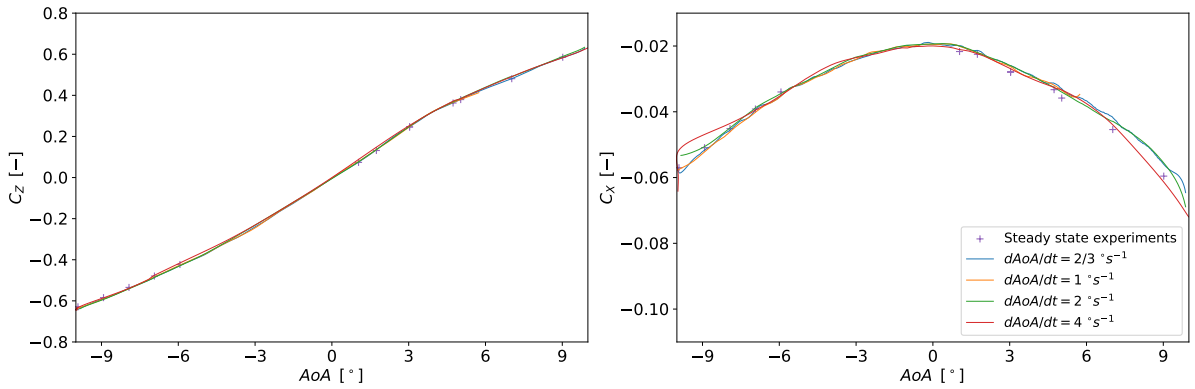

Figure 6.9: NACA 0012 T-foil ($AR = 5$), Positive angle sweeps at $h/c = 2$, $Re = 1.5 \cdot 10^5$, $v_\infty = 2\ ms^{-1}$

Figure 6.9 shows that the influence of the angular velocity is marginal. Only at an angular velocity of $4\,^\circ s^{-1}$ a difference can be distinguished. Larger differences are expected at higher angular velocities. From figure 6.9, it can be concluded that a rate of change of $2/3\,^\circ s^{-1}$ is a well converged angular velocity and therefore usable for examination of the performance of hydrofoils at a freestream velocity of $2\ ms^{-1}$.

6.2.3 Continuous angle sweep (AoA)

The converged angular velocity of $2/3\ ^{\circ}s^{-}1$ was used for a positive and a negative angle sweep. The foil pitched around the foil reference frame from an AoA of $-10\ ^{\circ}$ to $16\ ^{\circ}$ for the positive sweep and from $10\ ^{\circ}$ to $-16\ ^{\circ}$ for a negative sweep which is illustrated in figure 6.10.

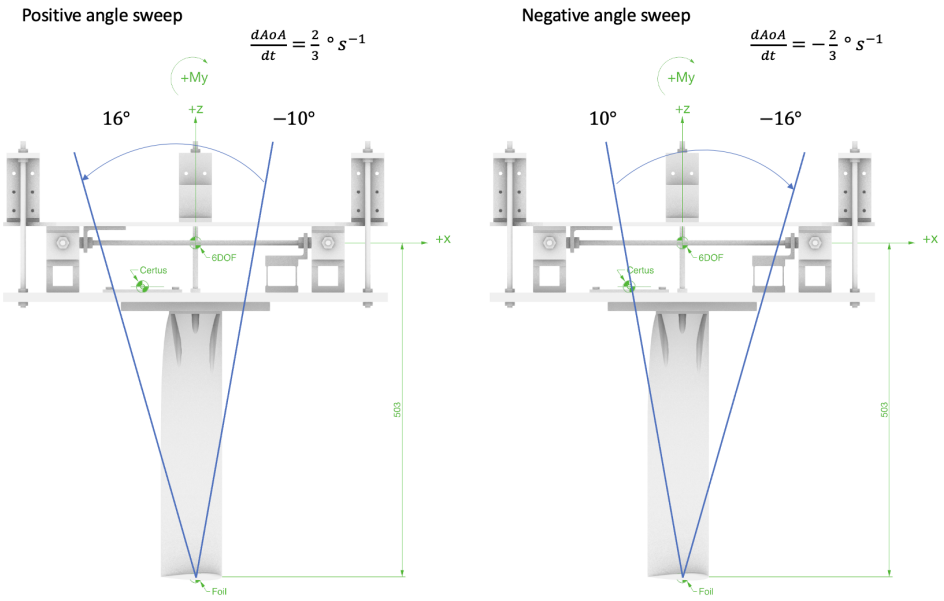

Figure 6.10: Illustration of positive and negative angle sweep

Starting the movement at these angles prevented turbulent flow which could remain attached to the foil during the pitching. The sweeps were performed at $h/c = 0.5$, 1.5 and 2.5 at a carriage velocity of 2 ms^{-1}. Figures 6.11, 6.12 and 6.13 show the resulting graphs for $h/c = 0.5$, 1.5 and 2.5 respectively.

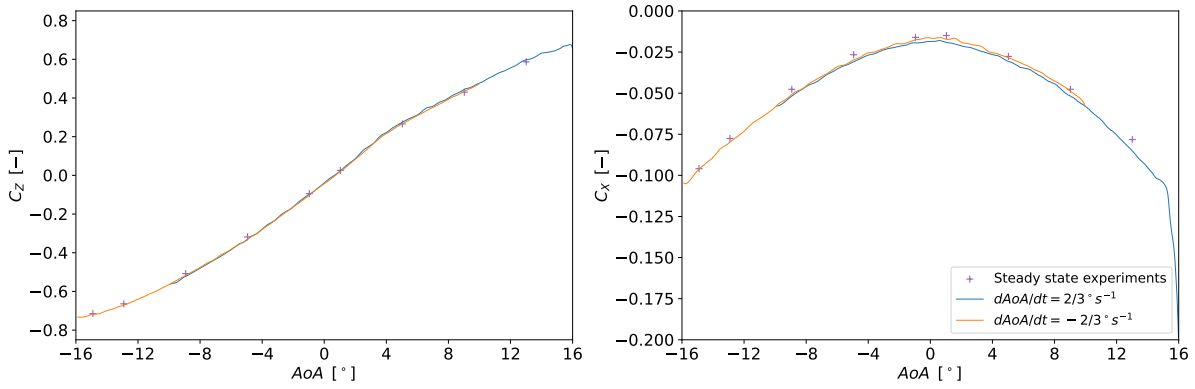

Figure 6.11: Lift and drag coefficient from positive and negative angle sweep at: $h/c = 0.5$, $Re = 1.5 \cdot 10^5$ and $v_\infty = 2\ ms^{-1}$

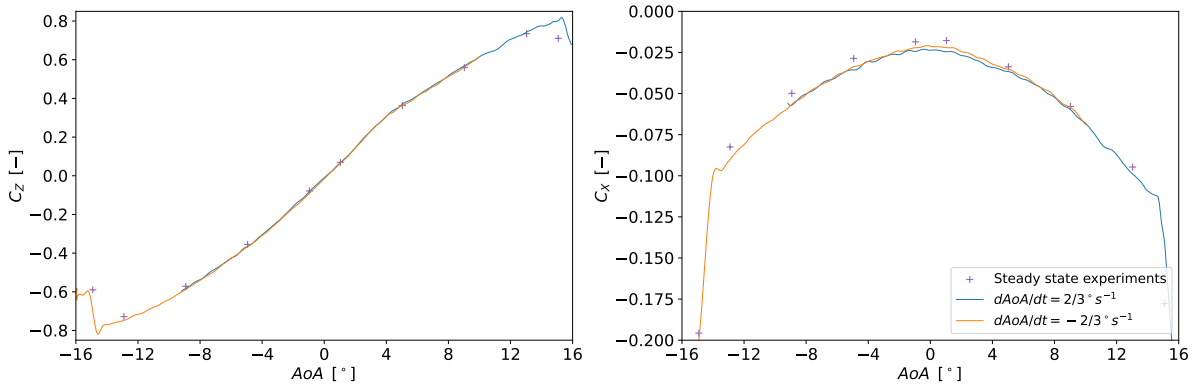

Figure 6.12: Lift and drag coefficient from positive and negative angle sweep at: $h/c = 1.5$, $Re = 1.5 \cdot 10^5$ and $v_\infty = 2\ ms^{-1}$

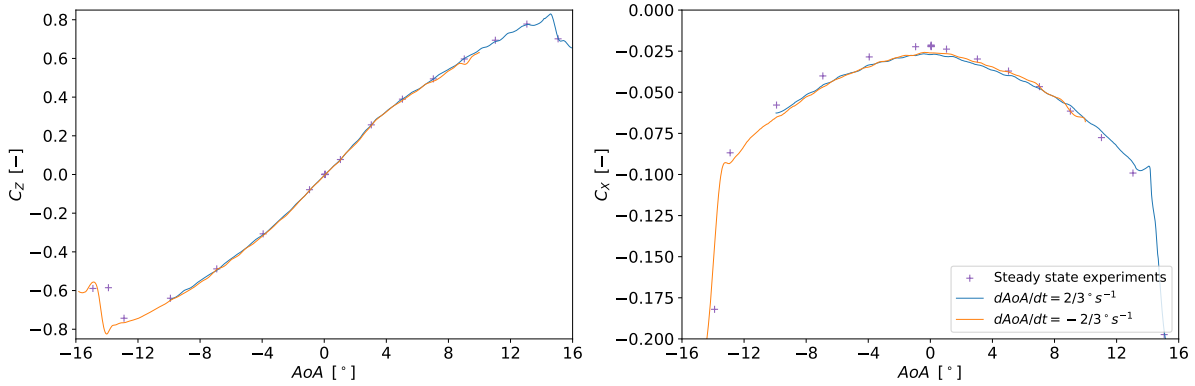

Figure 6.13: Lift and drag coefficient from positive and negative angle sweep at: $h/c = 2.5$, $Re = 1.5 \cdot 10^5$ and $v_\infty = 2\ ms^{-1}$

The angle sweep for lift, depicted in the left graphs of figures 6.11, 6.12 and 6.13 amplifies the value of this method. It shows that the steady state measurements fall within the envelope created by the two lines. Including the uncertainty of the steady state measurements, it can be stated that a better result is achieved with this method because the uncertainty of two experiments from two directions, is lower than that of steady state measurements. This is amplified in table 6.2 which is given at the end of this chapter. Additionally, the effects near the stall boundary are better captured using this method. Finally, depending on the grid of the steady state tests, the towing tank time can be reduced dramatically. For this particular example the towing tank time would be reduced by 78%.

The right graphs in figures 6.11, 6.12 and 6.13 show the resulting drag coefficients from the angle sweeps. The positive and negative angle sweep show a near to exact match while the steady state experiments show smaller absolute values for negative angles of attack. Looking at figure 5.6, the same difference can be seen. From this it can be concluded that the angle sweep corresponds better to the initial calculation than the steady state results. In section 5.2.2, this difference was attributed to surface effects. Because the continuous angle sweep method does not show this off-set, it can be concluded that the influence of surface effect is smaller.

An overview of the results and their range is given in 6.2. For each hydrodynamic coefficient the mean of the positive and the negative angle sweep is taken for a particular angle of attack. After the distance between the 2 points is given by the range to value the accuracy of the point. It is chosen to calculate this for the same angles as done for the stepwise angle sweep presented in table 6.1. The value of the angle sweep method is that this can be done for all angles within the range of -16 to 16 degrees. It should be noted that for values larger than 10 and smaller than -10 the result is based on 1 data set only and thus less accurate. To increase this range, a larger starting angle can be chosen. The effect can then be evaluated based on the sweep in the other direction.

	$h/c = 0.5$				$h/c = 1.5$				$h/c = 2.5$			
AoA	$C_{L.as}$	*range*	$C_{D.as}$	*range*	$C_{L.as}$	*range*	$C_{D.as}$	*range*	$C_{L.as}$	*range*	$C_{D.as}$	*range*
-11	-0.58	-	0.060	-	-0.64	-	0.063	-	-0.068	-	0.066	-
-9	-0.52	0.0064	0.052	0.0001	-0.59	0.0072	0.057	0.0003	-0.60	0.013	0.061	0.0032
-5	-0.33	0.0057	0.032	0.0004	-0.37	0.0004	0.035	0.0045	-0.38	0.0019	0.040	0.0035
0	-0.04	0.0013	0.017	0.0021	-0.01	0.0027	0.022	0.0007	-0.01	0.0045	0.025	0.0001
5	0.27	0.0053	0.030	0.0048	0.36	0.0018	0.036	0.0053	0.38	0.0058	0.039	0.0013
9	0.44	0.0083	0.050	0.0025	0.56	0.0050	0.060	0.0043	0.58	0.026	0.060	0.0010
11	0.50	-	0.062	-	0.63	-	0.076	-	0.66	-	0.070	-

Table 6.2: Hydrodynamic coefficients based on stepwise angle change for NACA 0012 T-foil ($AR = 5$), $h/c = 0.5$ and $v_\infty = 2$

From tables 6.1 and 6.2, it can be concluded that the accuracy of the continuous angle sweep is approximately 10 times better. Combined with the ability to find the results for any chosen angle, it makes the angle sweep a powerful method in experimental foil characterisation.

7 Behaviour of NACA 0012 T-foil in dynamic conditions

Based upon the calculations shown in section 6.1, the results of the dynamic experiments are presented. It is desired to compare the experimental results with a prediction to evaluate the results. In the first section of this chapter, multiple prediction models are presented. First, a prediction model using the steady state measurements from section 5.2.4 is presented, which is referred to as steady state interpolation model (model.ss). Another prediction model using X-foil data is discussed which, in contradiction to the steady state prediction model, is compensating for Reynolds number. This allows for more accurate prediction at higher freestream velocity. At the end of the first section a transfer function is presented which calculates the phase shift and modulus to express the difference between the steady state interpolation function and the measurements. This enables the comparison of the results with other research, such as Theodorsen & Mutchler (1935). Subsequently, the dynamic results are compared to the predictions in the second section of this chapter.

7.1 Calculations

This section will continue on the calculation method described in section 6.1 to evaluate dynamic conditions. The prediction method using the steady state experiments is compensated for the movement of the foil. Also, a prediction is made using the mathematical software X-foil. Then, a method to compare the predictions from the steady state interpolation function with the actual measurements, using modulus and phase shift is introduced. The calculations are made preparatory to the presented figures in section 7.2.

7.1.1 Prediction model using steady state measurements

Using the steady state results, a model was made in section 5.2.4. This model enables the calculation of the hydrodynamic properties as a function of h/c and AoA, which have been calculated in section 6.1.1. As previously mentioned, the decision was made to remain in the axis system of the carriage, which means that the lift and drag coefficient from the steady state interpolation model (model.ss) should be corrected for the direction of the flow velocity at the foil which has changed due to the motion. These steps are highlighted in blue in the flowchart presented in figure 6.1.

$$C_{Z.model.ss} = \cos(\alpha_{motion})\ Lift_{model.ss}(h/c,\ AoA) + \sin(\alpha_{motion})\ Drag_{model.ss}(h/c,\ AoA) \tag{7.1}$$

$$C_{X.model.ss} = -\sin(\alpha_{motion})\ Lift_{model.ss}(h/c,\ AoA) - \cos(\alpha_{motion})\ Drag_{model.ss}(h/c,\ AoA) \tag{7.2}$$

7.1.2 Prediction model using X-foil data

As in the prediction using the steady state measurements, a prediction is made using X-foil. The advantage of this prediction is that it takes into account the Reynolds number. The downside is that it is a numerical prediction which is less accurate than the steady state predictions, because assumptions are made for the compensation of certain effects such as finite wingspan, free surface interaction, T-joint interference and drag due to spray.

In section 3.1.1, a prediction model using X-foil was introduced. This method was used to calculate $C_{L.xfoil}$ and $C_{D.xfoil}$ as a function of AoA and Re for every time step in a dynamic experiment. The stream velocity at the foil (v_f) and angle of attack were used from section 6.1.1 to compensate for the movement of the foil. The coefficients were then compensated for surface effect using equation 5.4 and correction factors $K1_L$ (equation 5.5) and $K1_D$ (equation 5.6).

The new equations for $C_{L.xfoil}$ and $C_{D.xfoil}$ were constructed by simplifying these equations:

$$C_{L.xfoil} = K_1 \frac{AR}{AR+2} C_l(AoA,\ Re) \tag{7.3}$$

In which $AR = 5$ from equation 3.4:

$$C_{D.xfoil} = \frac{(C_d + C_{Di})\, A_{horizontal} + C_d\, A_{vertical}}{A_{horizontal}} + \frac{2\, D_{int}}{v_\infty^2\, \rho\, A_{horizontal}} \tag{7.4}$$

In this equation $A_{vertical}$ is calculated using the information provided in section 3.1 as follows :

$$A_{vertical} = 8538 \cdot 10^{-6}\ h/c \tag{7.5}$$

7.1.3 Transfer function C_{TF}

The difference between actual measurements and expectation using the steady state model is compared using the same format as used by Theodorsen & Mutchler (1935). Two sine shaped function fits are compared by modulus (M) and phase shift (ϕ) which are required to transform the steady state prediction to the actual measurement. This can be described by the transfer function $C_{TF.Z}$ and $C_{TF.X}$ for z and x-direction respectively.

$$C_{Z.measured} = C_{TF.Z}\, C_{Z.model.ss} = M\, e^{\phi i}\, C_{Z.model.ss} \tag{7.6}$$

$$C_{X.measured} = C_{TF.X}\, C_{X.model.ss} = M\, e^{\phi i}\, C_{X.model.ss} \tag{7.7}$$

The transfer functions are implemented in the flow chart presented in figure 6.1 and are highlighted in purple.

7.2 Analyses of dynamic conditions

This section presents an analyses of the results of the experiments in dynamic conditions, of which two series with a sinusoidal character were performed, with changing variables of heave and pitch respectively. Limited by maximum accelerations, four experiments were performed, using the full capability of the hexapod. During these experiments, the model velocity was changed between 2 ms^{-1} and 5 ms^{-1}.

Figures showing the data for C_Z, C_X and C_Z/C_X are presented. C_Z and C_X are discussed using a time trace and a combined figure depicting C_Z vs. h/c and a fraction of the time trace showing the particular behaviour over a few oscillations.

7.2.1 NACA 0012 T-foil subjected to a sinusoidal heaving motion

The oscillation imposed to the setup during a sinusoidal heaving experiment is illustrated in figure 7.1

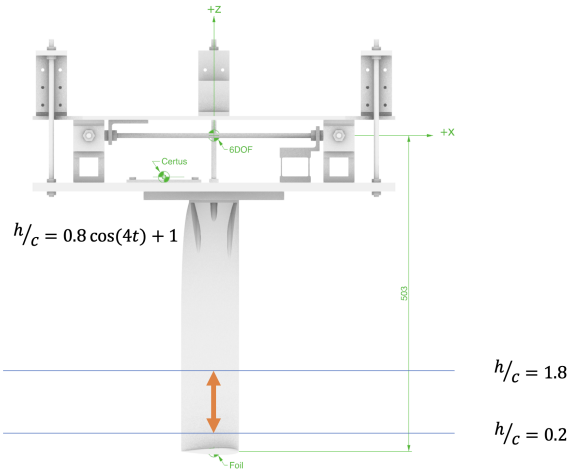

Figure 7.1: Illustration of the sinusoidal heaving motion

Time traces for the imposed motions are presented in figure 7.2 in which C_Z, and figure 7.3 in which C_X is depicted on the left axis.

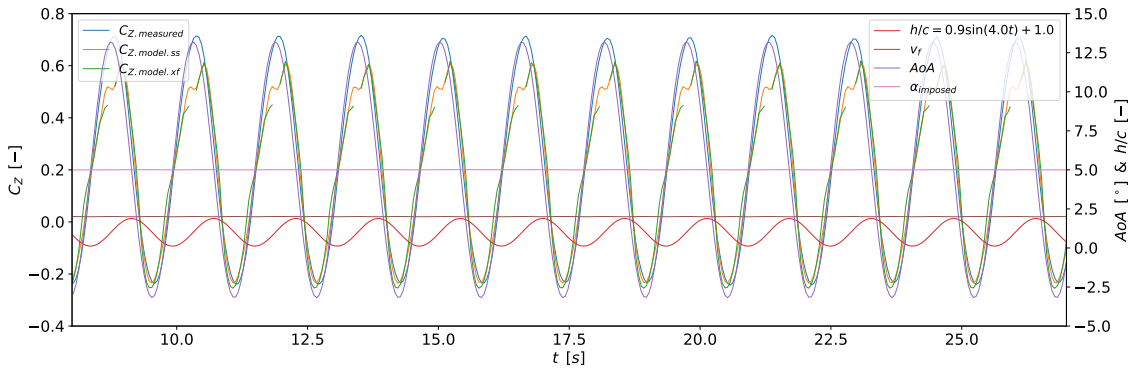

Figure 7.2: Timetrace of measurements and predictions of C_Z, v_f, AoA and $\alpha_{imposed}$ for NACA 0012 T-foil ($AR = 5$) subjected to sinusoidal heave at: $Re = 1.5 \cdot 10^5$, $v_\infty = 2\ ms^{-1}$

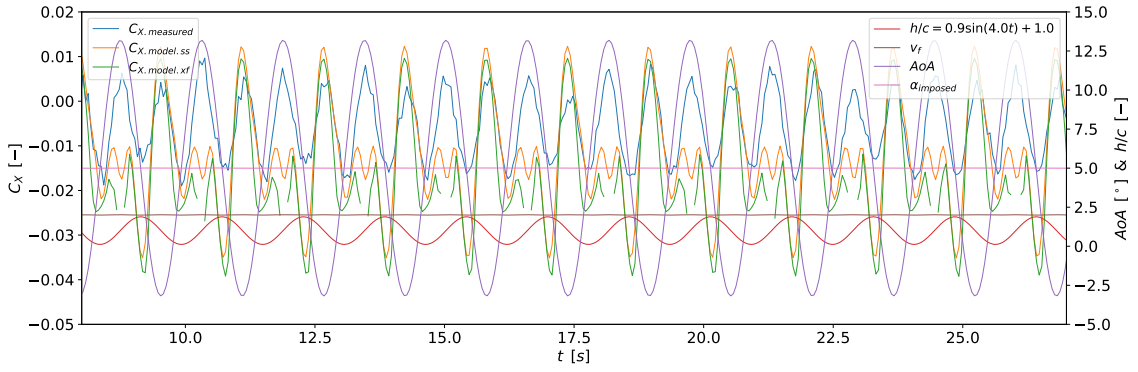

Figure 7.3: Timetrace of measurements and predictions of C_X, v_f, AoA and $\alpha_{imposed}$ for NACA 0012 T-foil ($AR = 5$) subjected to sinusoidal heave at: $Re = 1.5 \cdot 10^5$, $v_\infty = 2\ ms^{-1}$

In response to the sinusoidal heaving, a periodic behaviour is observed in both time traces. The response lags the imposed location h/c by half a period. Equation 6.4 and 6.5 show that the angle of attack and stream velocity at the foil depend on the imposed velocity of the foil in x and z-direction. A half period lag is found when the imposed velocity in z-direction is calculated using the function for h/c given in figure 7.1. Note that h/c is defined as the submergence of the foil and that z is defined positive upwards. As a result the minus sign occurs in the following equation:

$$\dot{z} = -\dot{h/c} = 3.2\sin(4t) = 3.2\cos(4t - \pi/2) \tag{7.8}$$

In figures 7.3 and 7.2, a gap occurs in the data by X-foil. This gap occurs due to the large angle of attack which is a result of the imposed motion. To gain a better comprehension of the actual differences, this and other findings are discussed using enriching figures 7.4, 7.5, 7.6 and 7.7 which show C_Z vs. h/c over the entire time trace in a graph on the left. In this manner the difference between the periods becomes visible, providing a better understanding of the differences between measured data, results from the steady state interpolation function and predictions from X-foil. To understand the location in the time trace, a fraction of the time trace is shown in the graph on the right. The time trace presented in figure 7.2 corresponds to figure 7.4.

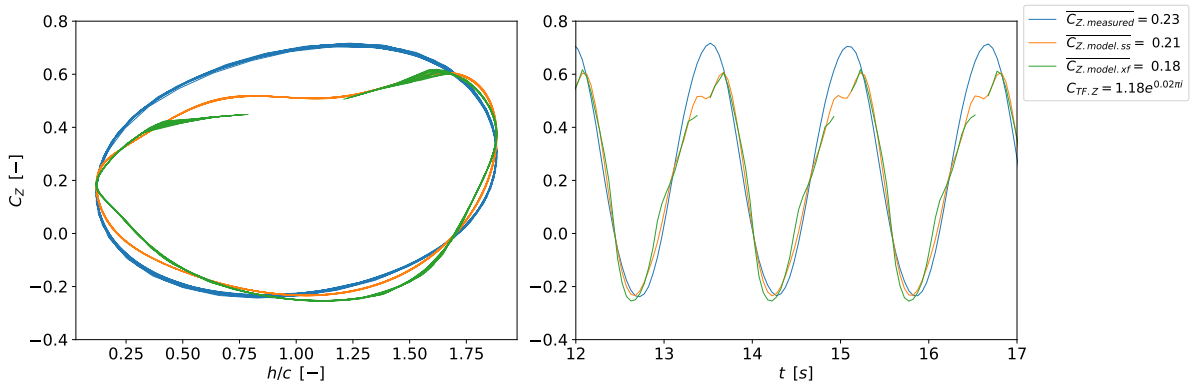

Figure 7.4: NACA 0012 T-foil ($AR = 5$) subjected to sinusoidal heave, comparison of C_Z for measured, model.ss and model.xf at: $\alpha_{imposed} = 5\ ^\circ$, $h/c = 0.8\cos(4t) + 1$, $v_\infty = 2\ ms^{-1}$, $Re = 1.5 \cdot 10^5$

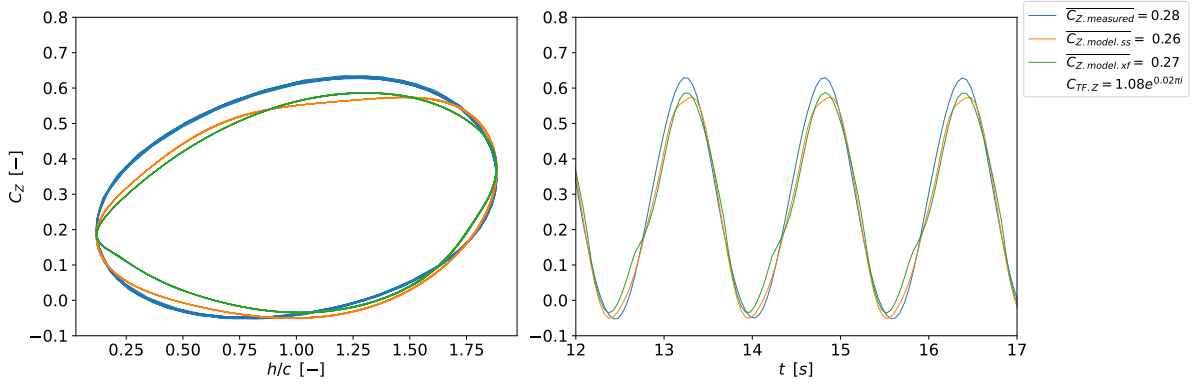

Figure 7.5: NACA 0012 T-foil ($AR = 5$) subjected to sinusoidal heave, comparison of C_Z for measured, model.ss and model.xf at: $\alpha_{imposed} = 5\ ^\circ$, $h/c = 0.8\cos(4t) + 1$, $v_\infty = 3\ ms^{-1}$, $Re = 2.3 \cdot 10^5$

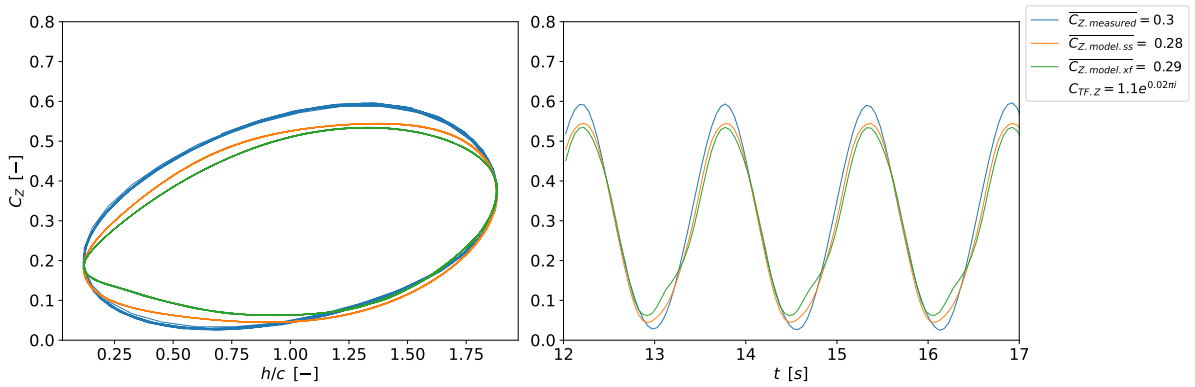

Figure 7.6: NACA 0012 T-foil ($AR = 5$) subjected to sinusoidal heave, comparison of C_Z for measured, model.ss and model.xf at: $\alpha_{imposed} = 5\ ^\circ$, $h/c = 0.8\cos(4t) + 1$, $v_\infty = 4\ ms^{-1}$, $Re = 3.1 \cdot 10^5$

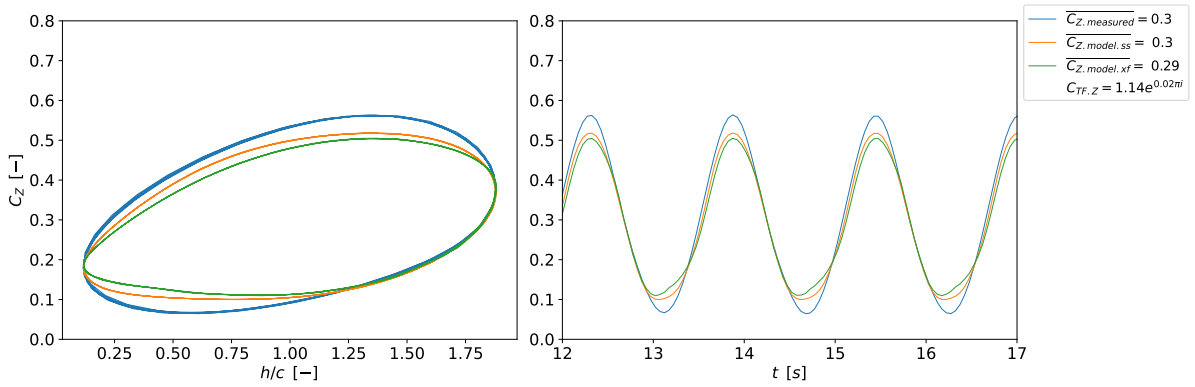

Figure 7.7: NACA 0012 T-foil ($AR = 5$) subjected to sinusoidal heave, comparison of C_Z for measured, model.ss and model.xf at: $\alpha_{imposed} = 5\ ^\circ$, $h/c = 0.8\cos(4t) + 1$, $v_\infty = 5\ ms^{-1}$, $Re = 3.8 \cdot 10^5$

In the first figure, 7.4, a gap in the model from X-foil occurs. The steady state model shows a similar dent in the top of the C_Z curve, which disappears in figures 7.6 and 7.7. Due to the relatively small velocity of the carriage, large angles of attack occur when the foil is pushed down. As a result, the angle of attack consists of an imposed angle of 5 ° and a relatively large angle due to the motion described by equation 6.4. The angle of attack during heave at v_∞ can be extracted from figure 7.2 and equals 13 °. At this angle, flow stalled during the steady state experiments. Also, the interpolation function of X-foil is not provided with data for these large angles, because numerical software is unable to make a prediction when the flow is no longer attached to the foil. The measured signal does not show any of this. It can be concluded that either flow remains attached longer or the angle of attack is influenced by the wake vorticity.

Looking at the measurements and the steady state interpolation function in figures 7.4, 7.5, 7.6 and 7.7, a constant surplus can be seen in the top of the "eggs". To achieve this, the angle of attack must be high and thus flow must remain attached at higher angles.

Finally, over all experiments a very small lag of about 0.05 *rad* is identified between the measured and steady state interpolation function.

The above analyses for C_Z is repeated for C_X and presented in figures 7.8, 7.9, 7.10 and 7.11. The time trace presented in figure 7.3, corresponds to figure 7.8.

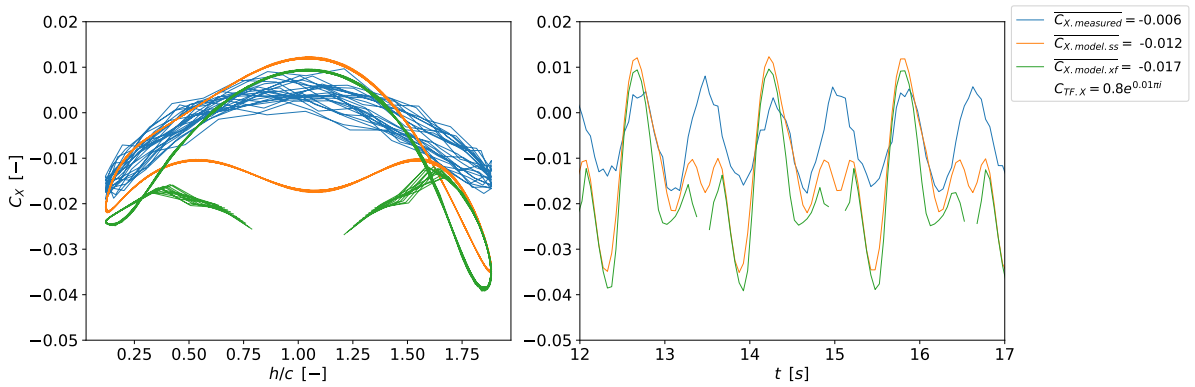

Figure 7.8: NACA 0012 T-foil ($AR = 5$) subjected to sinusoidal heave, comparison of C_X for measured, model.ss and model.xf at: $\alpha_{imposed} = 5\ ^\circ$, $h/c = 0.8\cos(4t) + 1$, $v_\infty = 2\ ms^{-1}$, $Re = 1.5 \cdot 10^5$

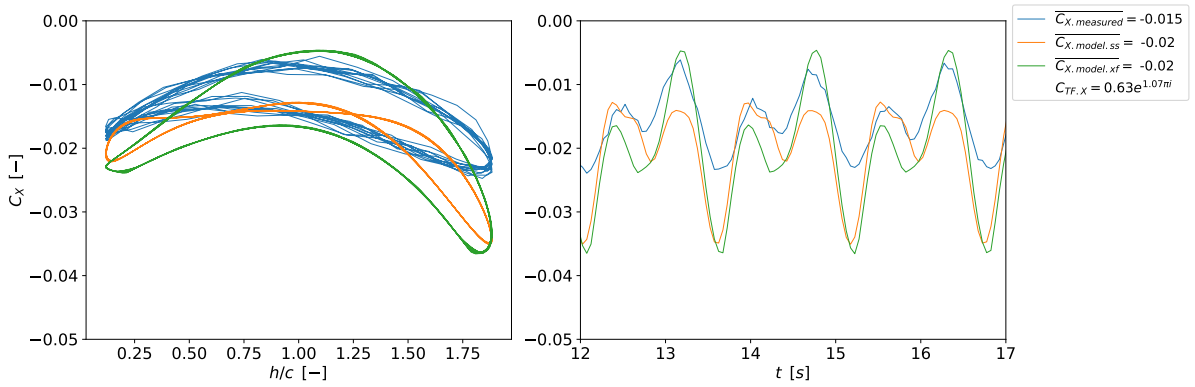

Figure 7.9: NACA 0012 T-foil ($AR = 5$) subjected to sinusoidal heave, comparison of C_X for measured, model.ss and model.xf at: $\alpha_{imposed} = 5\ ^\circ$, $h/c = 0.8\cos(4t) + 1$, $v_\infty = 3\ ms^{-1}$, $Re = 2.3 \cdot 10^5$

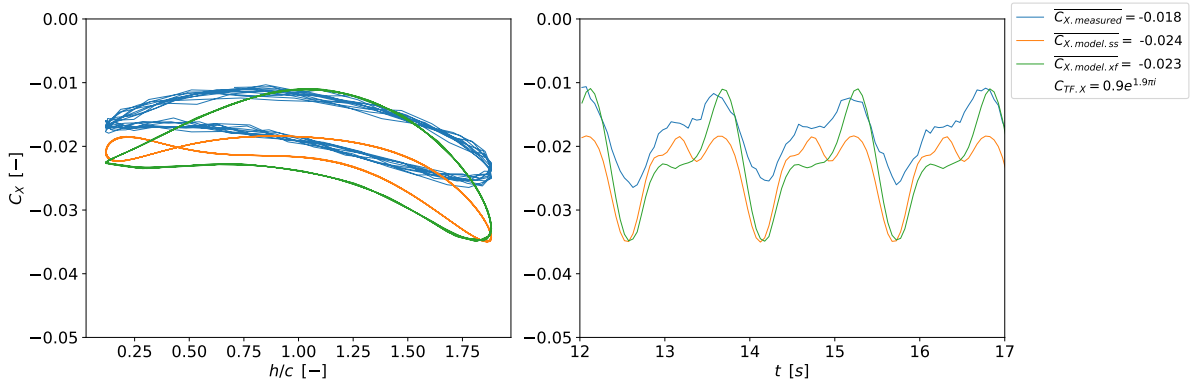

Figure 7.10: NACA 0012 T-foil ($AR = 5$) subjected to sinusoidal heave, comparison of C_X for measured, model.ss and model.xf at: $\alpha_{imposed} = 5\ ^\circ$, $h/c = 0.8\cos(4t) + 1$, $v_\infty = 4\ ms^{-1}$, $Re = 3.1 \cdot 10^5$

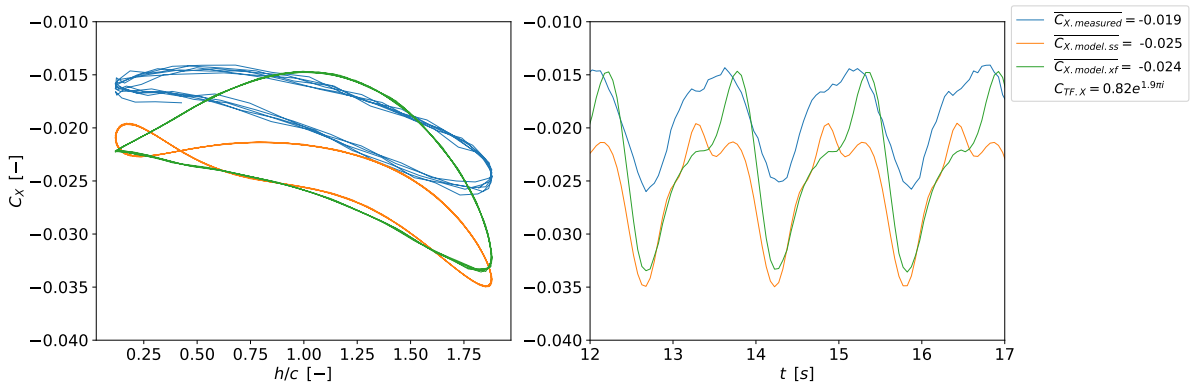

Figure 7.11: NACA 0012 T-foil ($AR = 5$) subjected to sinusoidal heave, comparison of C_X for measured, model.ss and model.xf at: $\alpha_{imposed} = 5\ ^\circ$, $h/c = 0.8\cos(4t) + 1$, $v_\infty = 5\ ms^{-1}$, $Re = 3.8 \cdot 10^5$

Where at $v_\infty = 2\ ms^{-1}$ (figure 7.3) predictions describe a voluminous "egg" shaped plot, the measurements report a close to similar drag in both the trajectory upwards and downwards. Having a constant imposed angle of 5 $^\circ$, it is expected that when pushing down, higher angles of attack will result in higher drag compared to lifting the foil up. This is amplified in equation 7.8.

The figures for C_X show more noise in the signal. This is due to the order of magnitude of these forces. It is chosen not to filter the data again to preserve all the effects.

Looking at the magnitude of C_X, the average is moving from -0.005 to -0.0015 to -0.0018 to -0.0019. Note that in the first figure almost a propulsive force is achieved by the heaving motion. At increasing velocity, the induced motion becomes less relevant, resulting in drag dominated C_X. It is interesting to discover that all the predictions, where no flow separation occurs, show a 33% larger prediction than measurement. From chapter 5, a drag coefficient (C_D) of 0.027 is found in steady state conditions where $AoA = 5$, $h/c = 1$ and $v_\infty = 4$. The mean drag coefficient corresponding to these settings in dynamic behaviour is 0.024. It can be concluded that less drag is measured in dynamic conditions.

The performance of hydrofoils is often presented as C_L vs C_D. The value of this presentation is that foils can easily be compared in terms of overall performance. To obtain knowledge of the overall performance of this hydrofoil in dynamic conditions compared with the steady state and X-foil predictions, C_Z vs C_X is presented in figures 7.12, 7.13, 7.14 and 7.15.

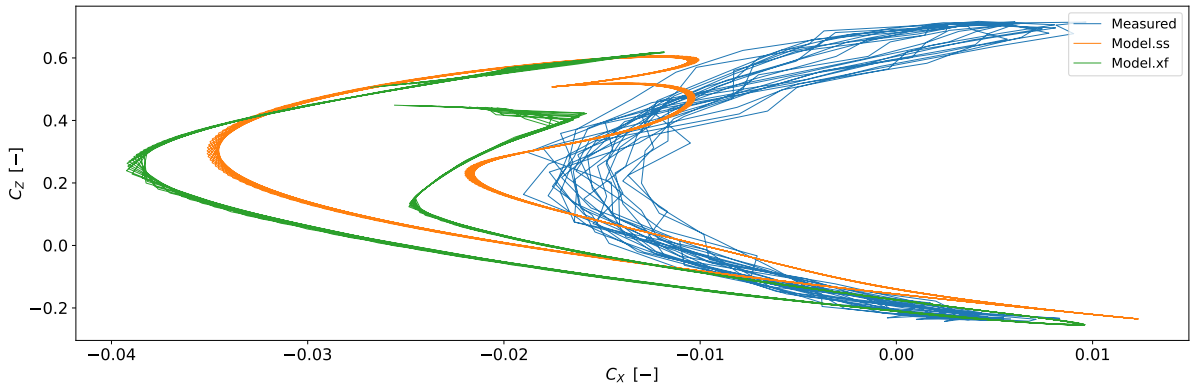

Figure 7.12: NACA 0012 T-foil ($AR = 5$) subjected to sinusoidal heave C_Z vs. C_X at: $\alpha_{imposed} = 5\ ^\circ$, $h/c = 0.8\cos(4t) + 1$, $v_\infty = 2\ ms^{-1}$, $Re = 1.5 \cdot 10^5$

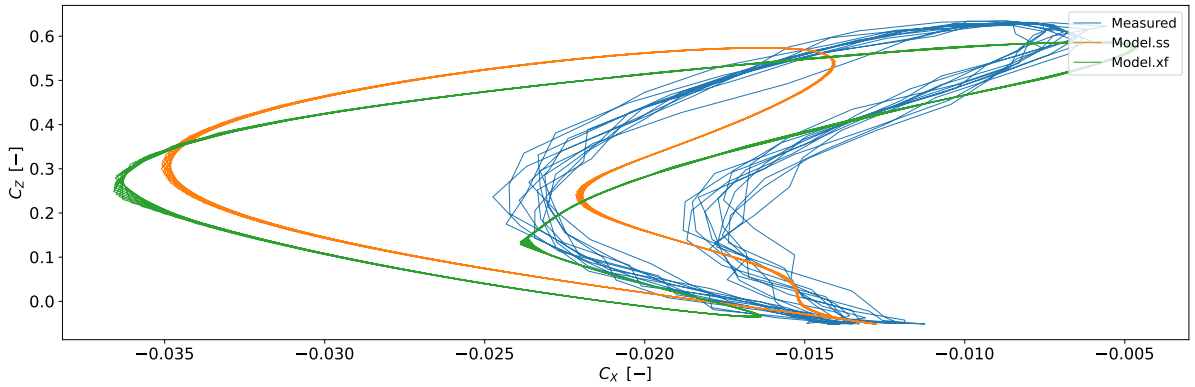

Figure 7.13: NACA 0012 T-foil ($AR = 5$) subjected to sinusoidal heave C_Z vs. C_X at: $\alpha_{imposed} = 5\ ^\circ$, $h/c = 0.8\cos(4t) + 1$, $v_\infty = 3\ ms^{-1}$, $Re = 2.3 \cdot 10^5$

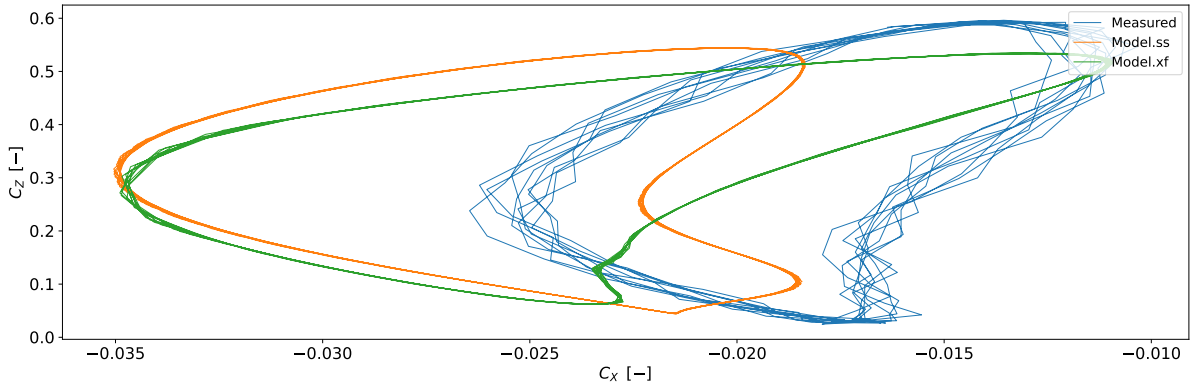

Figure 7.14: NACA 0012 T-foil ($AR = 5$) subjected to sinusoidal heave C_Z vs. C_X at: $\alpha_{imposed} = 5\ ^\circ$, $h/c = 0.8\cos(4t) + 1$, $v_\infty = 4\ ms^{-1}$, $Re = 3.1 \cdot 10^5$

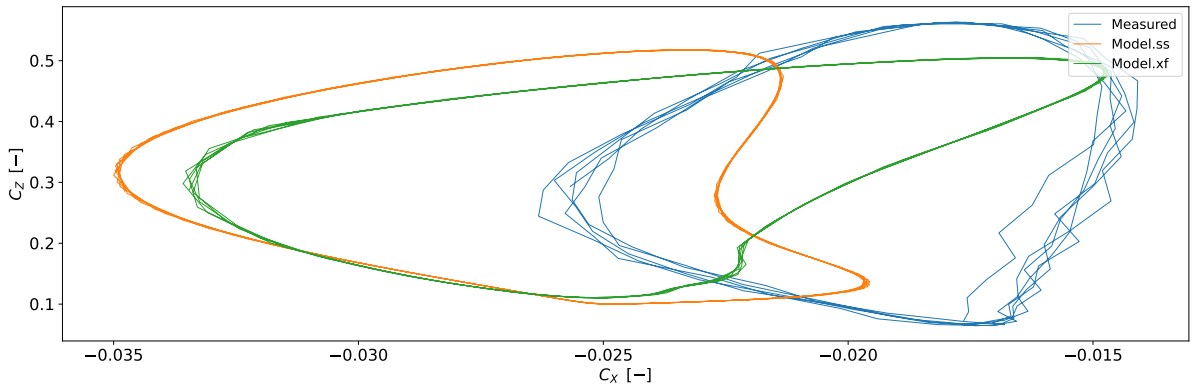

Figure 7.15: NACA 0012 T-foil ($AR = 5$) subjected to sinusoidal heave C_Z vs. C_X at: $\alpha_{imposed} = 5\ ^\circ$, $h/c = 0.8\cos(4t) + 1$, $v_\infty = 5\ ms^{-1}$, $Re = 3.8 \cdot 10^5$

At low freestream velocity the trajectory is very similar trajectory moving up and moving down while the trajectory becomes almost triangular at higher freestream velocity. All figures have a common turning point on the right-top and right-bottom. The top turning point on the right corresponds with $h/c = 1$ while pushing the foil downwards. The bottom right turning point corresponds with $h/c = 1$ while lifting the foil up. Due to the

imposed angle of attack, high lift is achieved when pushing down compared to negative or low lift while moving the foil up.

From the first figures, it can be concluded that positive values of C_X are achieved during the imposed motion which means propulsive force is created.

In all figures except figure 7.12, the point of curvature in the middle-left remains in a similar position. The point of curvature on the middle-right slowly disappears when freestream velocity is increased over the figures. The curvatures correspond to the moment in time where the imposed velocity is zero. The curvature on the left corresponds with $h/c = 1.8$ and the curvature on the right with $h/c = 0.2$. From this, it can be concluded that significantly less drag can be expected near the surface. This can be attributed to surface effects which has also been seen in figure 5.8 presented in section 5.2.3.

It is interesting to see that the shape of the prediction using the steady state results corresponds to that of the measured results in dynamic conditions. The largest difference is in C_X where all predictions predict higher resistance than actually measured.

For increasing model velocity, the prediction from X-foil increases in C_X direction compared to the steady state interpolation function. This amplifies the effect of Reynolds number where drag reduces at higher Re. Nonetheless, the steady state results remain the better representation. An enlarged database allowing for expansion of the steady state interpolation function with Re would add value and minimise the difference between the measured performance in dynamic conditions and the results from the steady state interpolation function even more.

7.2.2 NACA 0012 T-foil subjected to a sinusoidal pitching motion

The oscillation imposed to the setup during a sinusoidal pitching experiment is illustrated in figure 7.16.

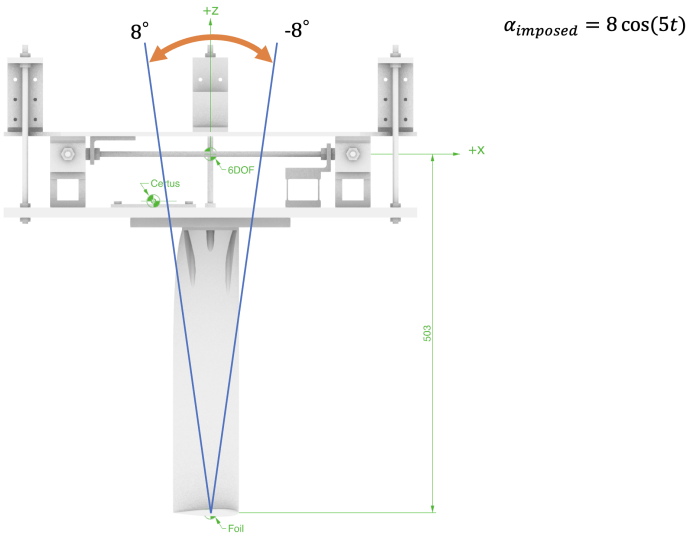

Figure 7.16: Illustration of the sinusoidal pitching motion

The foil rotates around a point located at 50% of the chord of the horizontal wing. As a result, both the angle of attack and stream velocity at the foil remain unchanged. Thus $AoA = \alpha_{imposed}$ and $v_f = v_\infty$ for the sinusoidal pitching motion.

Time traces for the sinusoidal motion are presented in figure 7.17 in which C_Z, and figure 7.18 in which C_X is depicted on the left axis.

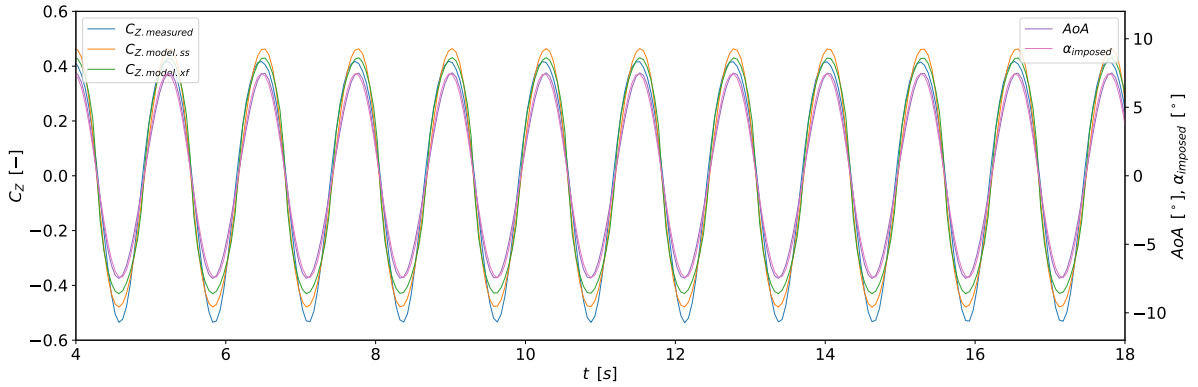

Figure 7.17: NACA 0012 T-foil ($AR = 5$) subjected to sinusoidal pitch time traces at: $v_\infty = 2\ ms^{-1}$, $Re = 1.5 \cdot 10^5$

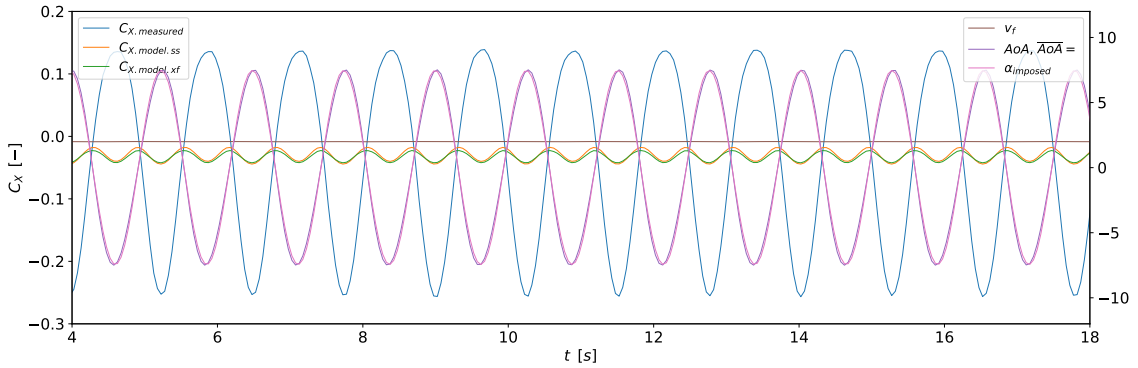

Figure 7.18: NACA 0012 T-foil ($AR = 5$) subjected to sinusoidal pitch time traces at: $v_\infty = 2\ ms^{-1}$, $Re = 1.5 \cdot 10^5$

In response to the sinusoidal pitching, a periodic behaviour is seen in both the C_Z and C_X time trace. Figure 7.18 shows a big difference between the measurement and prediction of C_X. This and other findings will be discussed based on figures similar to the ones used for the heaving motion. In these figures graphs of C_Z vs. AoA are combined with a fraction of the time trace. In this way the difference between the periods becomes visual and a clearer understanding of the differences between measured data, results from the steady state interpolation function and results from X-foil is provided. This is done for all sinusoidal pitching motions and given in figures 7.19, 7.20, 7.21 and 7.22. The time trace presented in figure 7.17 corresponds to figure 7.19.

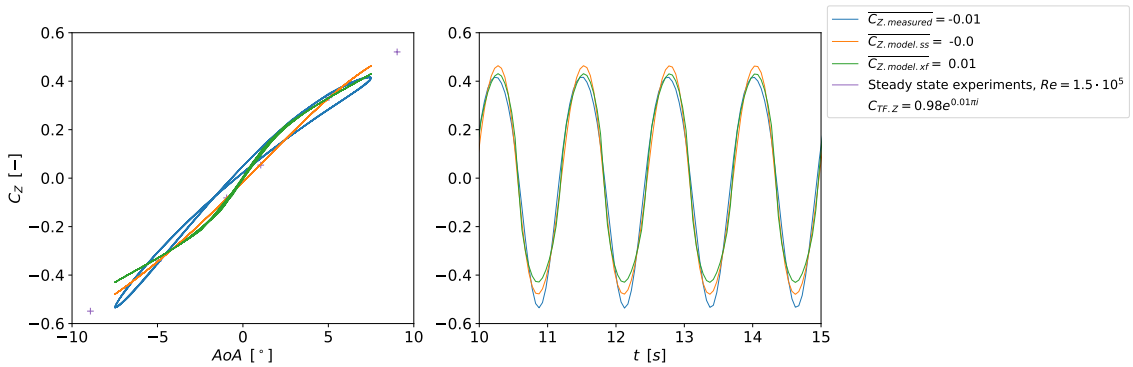

Figure 7.19: NACA 0012 T-foil ($AR = 5$) subjected to sinusoidal pitch, comparison of C_Z for measured, model.ss and model.xf at: $h/c = 1$, $\alpha_{imposed} = 8\cos(5t)$, $v_\infty = 2\ ms^{-1}$, $Re = 1.5 \cdot 10^5$

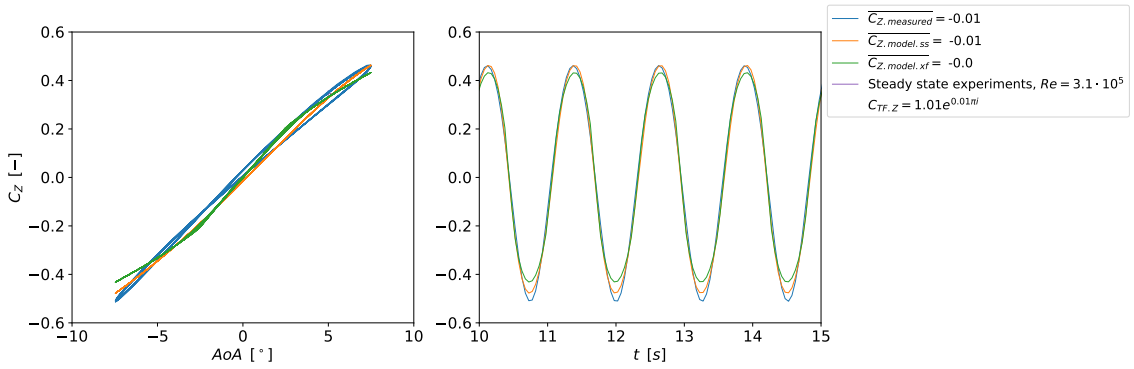

Figure 7.20: NACA 0012 T-foil ($AR = 5$) subjected to sinusoidal pitch, comparison of C_Z for measured, model.ss and model.xf at: $h/c = 1$, $\alpha_{imposed} = 8\cos(5t)$, $v_\infty = 3\ ms^{-1}$, $Re = 2.3 \cdot 10^5$

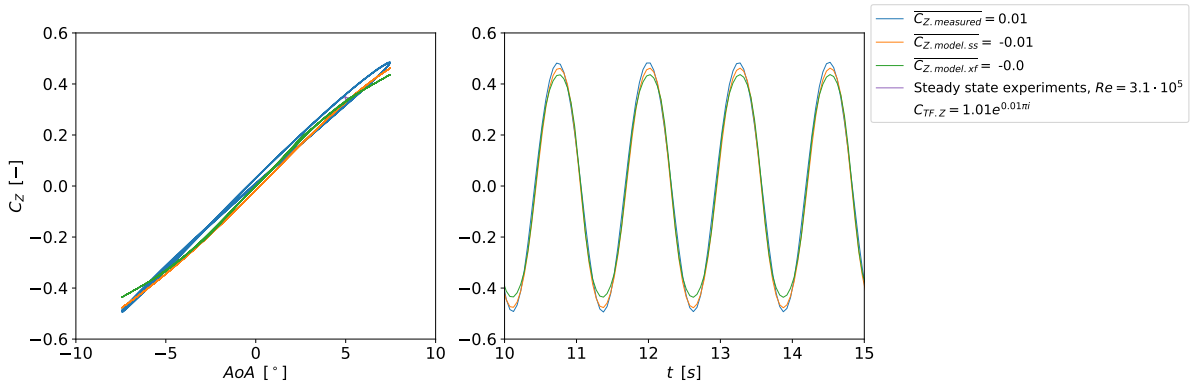

Figure 7.21: NACA 0012 T-foil ($AR = 5$) subjected to sinusoidal pitch, comparison of C_Z for measured, model.ss and model.xf at: $h/c = 1$, $\alpha_{imposed} = 8\cos(5t)$, $v_\infty = 4\ ms^{-1}$, $Re = 3.1 \cdot 10^5$

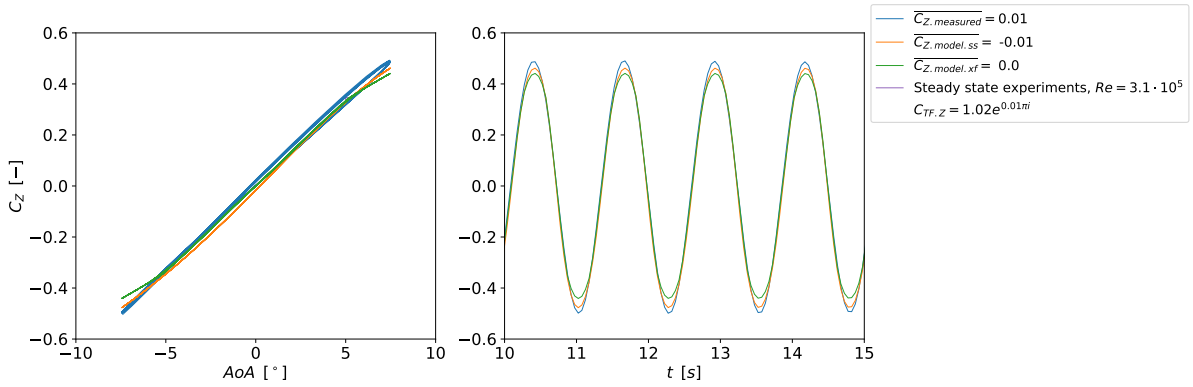

Figure 7.22: NACA 0012 T-foil ($AR = 5$) subjected to sinusoidal pitch, comparison of C_Z for measured, model.ss and model.xf at: $h/c = 1$, $\alpha_{imposed} = 8\cos(5t)$, $v_\infty = 5\ ms^{-1}$, $Re = 3.8 \cdot 10^5$

In the first figure 7.19, the largest difference is seen between measurements and predictions. The steady state experiments performed at $v_\infty = 2\ ms^{-1}$ and $h/c = 1$ have also been plotted. The usual s-curve that occurs in the lift as depicted in figure 5.2 can not be recognised in the measurements from the dynamic motion during which, higher lift coefficients are achieved around $AoA = 0\ °$. It is expected that this increase around 0 is caused by the surface interaction of the wake vorticity.

Looking at the difference between the measurements and the steady state interpolation function a tendency can be seen. The modulus increases with the freestream velocity from 0.98 ms^{-1} to 1.02 ms^{-1} while the phase shift remains constant at about 0.025 *rad*. This tendency is plotted in figure 7.23. In future research this plot could be expanded with more data to find a better representation of this relation.

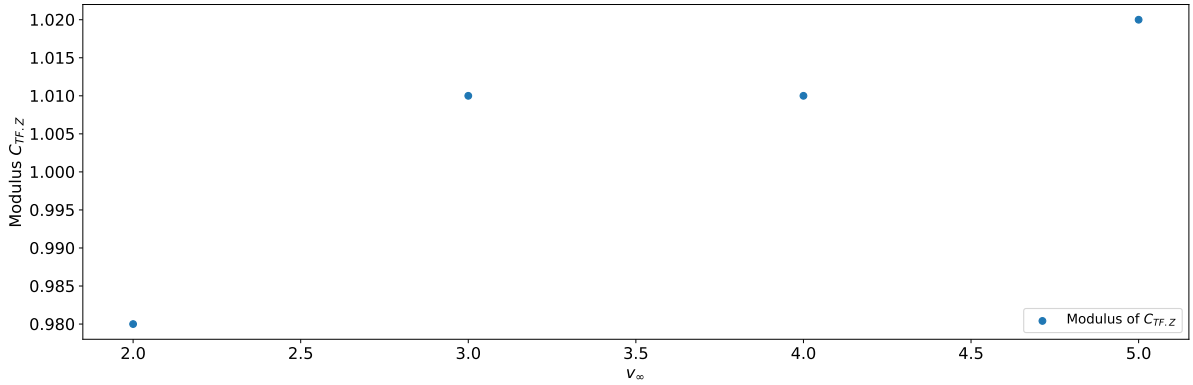

Figure 7.23: Modulus of $C_{TF.Z}$ vs. v_∞ for $h/c = 1$, $\alpha_{imposed} = 8\cos(5t)$

Also, the curve itself moves up slightly with increasing velocity. It can be concluded that larger fluctuation at higher average lift can be expected during sinusoidal pitching at higher velocity. Also a lag occurs with respect to the prediction.

As for C_Z, the same is done for C_X. This is visualised in figure 7.24, 7.25, 7.26 and 7.27. The time trace presented in figure 7.18, corresponds to figure 7.24.

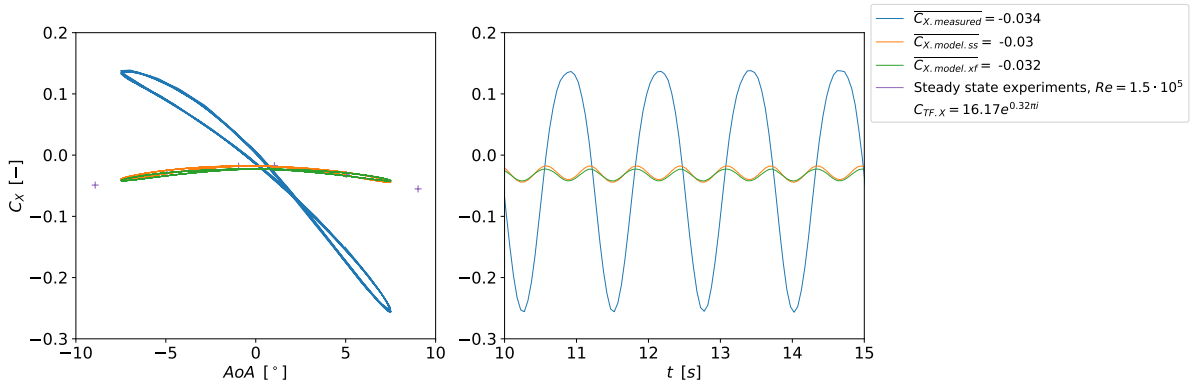

Figure 7.24: NACA 0012 T-foil ($AR = 5$) subjected to sinusoidal pitch, comparison of C_X for measured, model.ss and model.xf at: $h/c = 1$, $\alpha_{imposed} = 8\cos(5t)$, $v_\infty = 2\ ms^{-1}$, $Re = 1.5 \cdot 10^5$

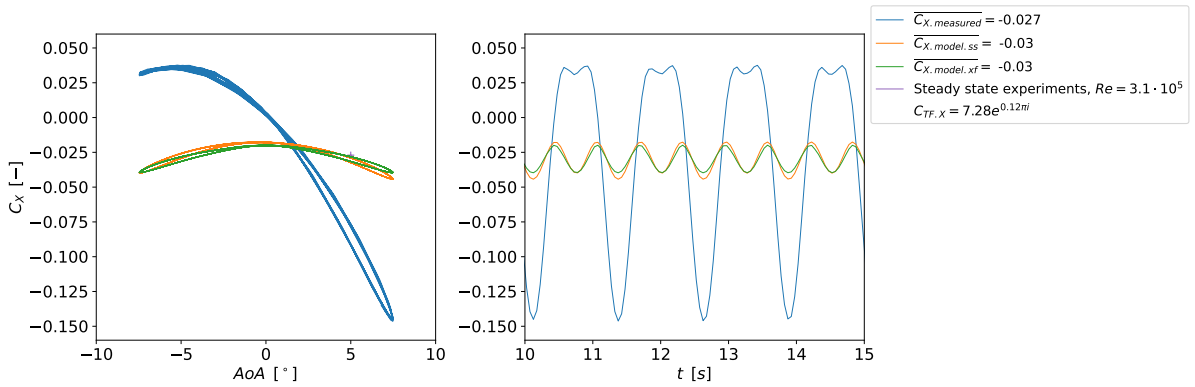

Figure 7.25: NACA 0012 T-foil ($AR = 5$) subjected to sinusoidal pitch, comparison of C_X for measured, model.ss and model.xf at: $h/c = 1$, $\alpha_{imposed} = 8\cos(5t)$, $v_\infty = 3\ ms^{-1}$, $Re = 2.3 \cdot 10^5$

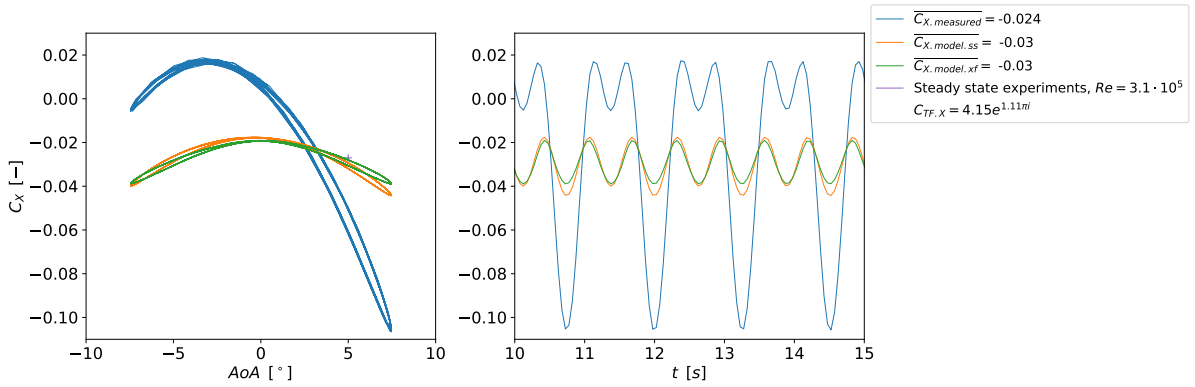

Figure 7.26: NACA 0012 T-foil ($AR = 5$) subjected to sinusoidal pitch, comparison of C_X for measured, model.ss and model.xf at: $h/c = 1$, $\alpha_{imposed} = 8\cos(5t)$, $v_\infty = 4\ ms^{-1}$, $Re = 3.1 \cdot 10^5$

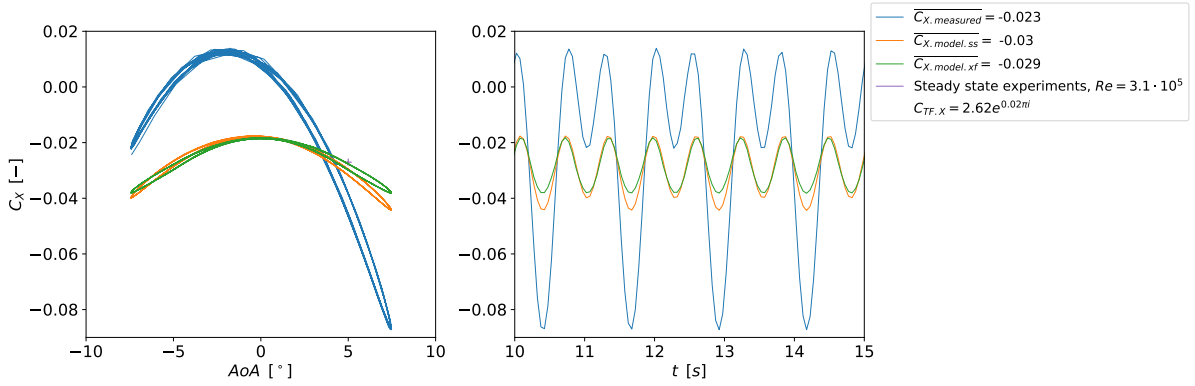

Figure 7.27: NACA 0012 T-foil ($AR = 5$) subjected to sinusoidal pitch, comparison of C_X for measured, model.ss and model.xf at: $h/c = 1$, $\alpha_{imposed} = 8\cos(5t)$, $v_\infty = 5\ ms^{-1}$, $Re = 3.8 \cdot 10^5$

Looking at the figures, a large difference occurs between the measured and the predicted results. In the first figure, the two prediction are almost identical and correspond with the steady state measurements while the dynamic measurements show a very different behaviour. The time traces show that, with increasing model velocity, the measurements start to show a similar double frequency. In the first figure, the peaks of the measured results are flat, while the troughs are sharp. Therefore it is expected that during the sinusoidal pitching another component acts on the resistance of the foil. This component has a frequency which is equal to the frequency of the sinusoidal movement while usually a double frequency is expected. This could be caused by induced drag which is directly related to the lift and which thus has a frequency equal to the pitching frequency (equation 2.7). This theory is confirmed when looking at figure 7.17 and 7.18 where the drag or negative C_X corresponds to C_Z.

After reexamination of the setup, an undesired component acting on the drag arises. When the pitch is changed, the foil's vertical is moving through the water resulting in an addition to the drag. This motion is depicted in figure 7.28 as $v_{induced}$.

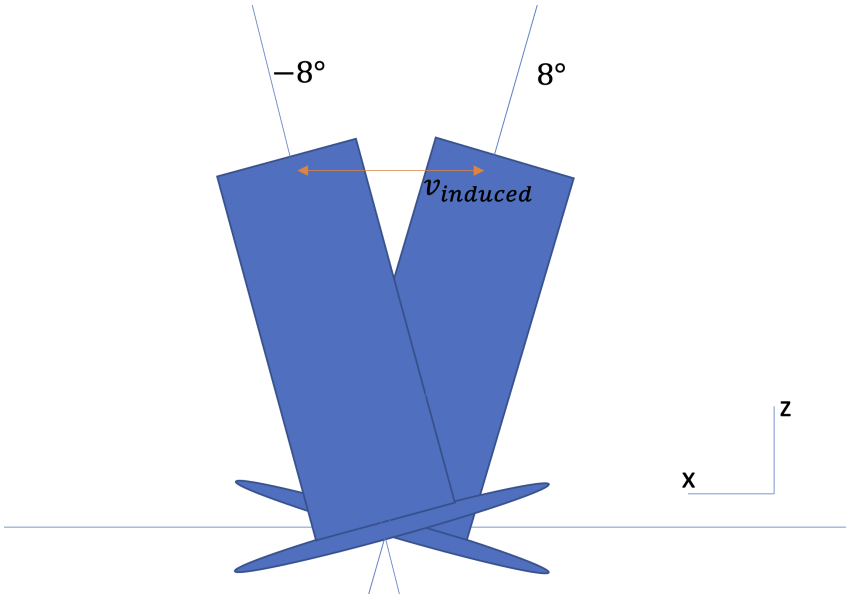

Figure 7.28: Induced motion of the vertical due to pitching motion

When the foil is pitching positive, the vertical is moving forward through the water. When the foil is pitching negative the vertical is moving backwards. This results in increased drag when decreasing the angle of attack and decreased drag when increasing the angle of attack. Looking at figure 7.24, this hypothesis is not confirmed. If true, an egg shaped figure would occur because passing through $AoA = 0\,^\circ$ one way, would result in an additional drag while moving through $AoA = 0\,^\circ$ the other way would result in a subtraction of drag.

From the analyses of the figures, it expected that the difference between the prediction and the measurement in dynamic conditions has a sinusoidal character. Therefore the difference between $C_{X.measured}$ and $C_{X.model.ss}$ is plotted as δC_X in figure 7.29 for all experiments.

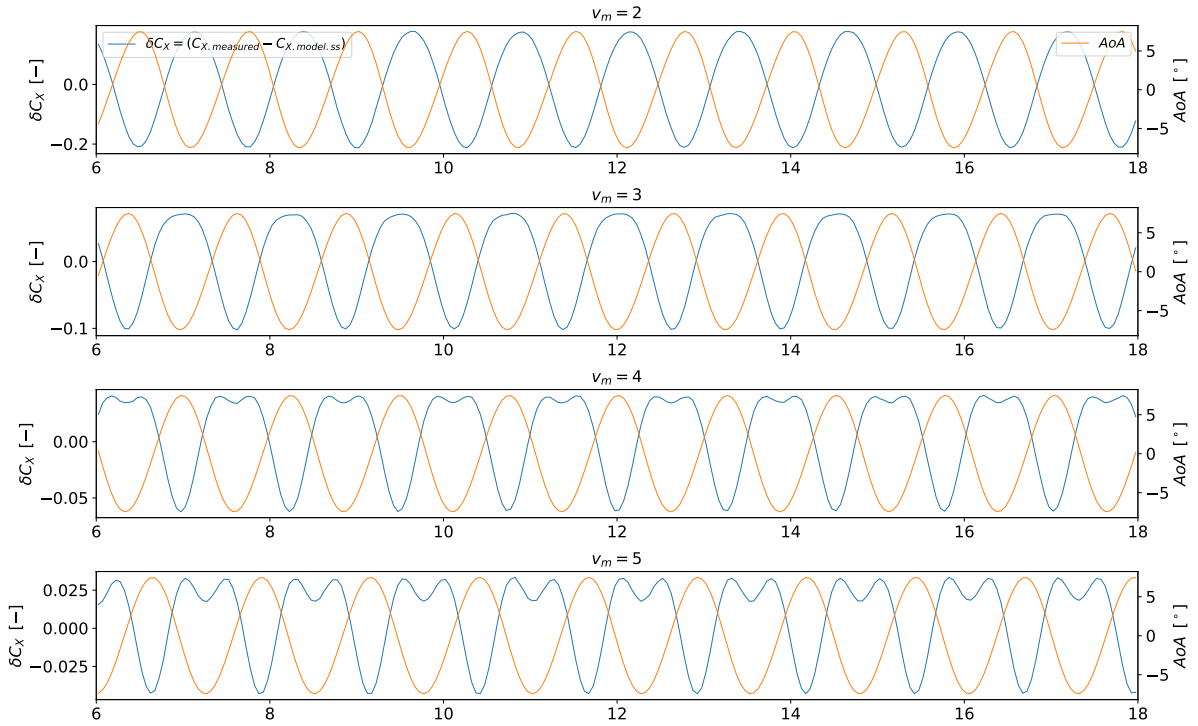

Figure 7.29: Difference between prediction and measurement for a NACA 0012 T-foil ($AR = 5$) subjected to sinusoidal pitch

During the first test a sinusoidal difference can be distinguished. For the other test a second sine wave can be seen. It can be assumed that this falls within the Reynolds error of the steady state interpolation function because this sine corresponds to the results.

In section 7.2.1, the difference in performance is discussed using C_Z vs. C_X. From the figures 7.24, 7.25, 7.26 and 7.27 depicting C_X vs. AoA, large differences in the C_Z vs. C_X figures are expected. The resulting figures are presented in figure 7.30, 7.31, 7.32 and 7.33.

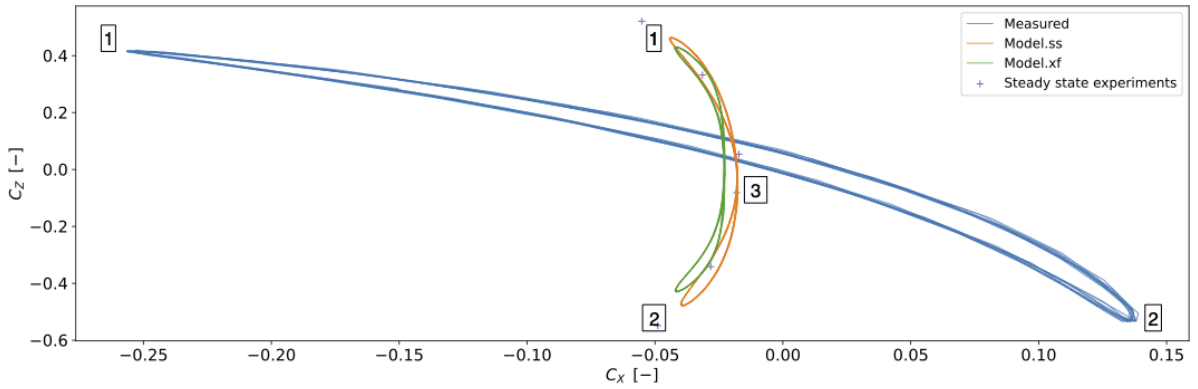

Figure 7.30: NACA 0012 T-foil ($AR = 5$) subjected to sinusoidal pitch C_Z vs. C_X at: $h/c = 1$, $\alpha_{imposed} = 8\cos(5t)$, $v_\infty = 2\ ms^{-1}$, $Re = 1.5 \cdot 10^5$

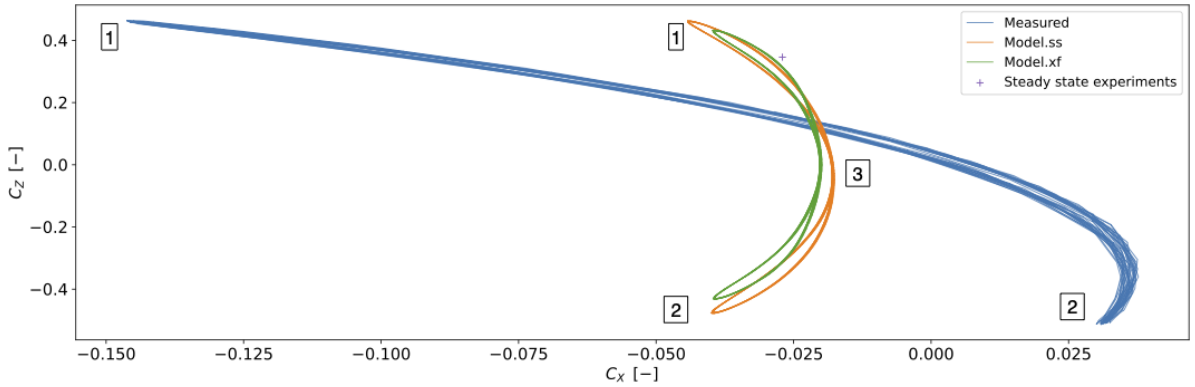

Figure 7.31: NACA 0012 T-foil ($AR = 5$) subjected to sinusoidal pitch C_Z vs. C_X at: $h/c = 1$, $\alpha_{imposed} = 8\cos(5t)$, $v_\infty = 3\ ms^{-1}$, $Re = 2.3 \cdot 10^5$

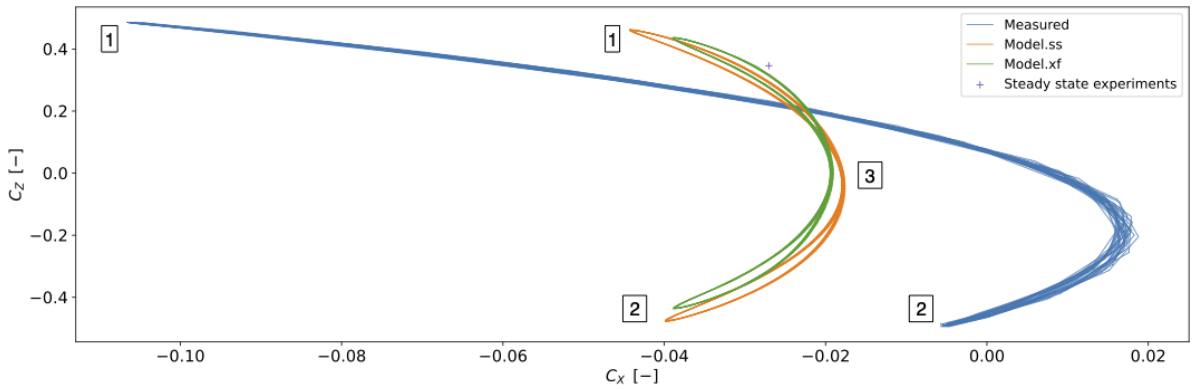

Figure 7.32: NACA 0012 T-foil ($AR = 5$) subjected to sinusoidal pitch C_Z vs. C_X at: $h/c = 1$, $\alpha_{imposed} = 8\cos(5t)$, $v_\infty = 4\ ms^{-1}$, $Re = 3.1 \cdot 10^5$

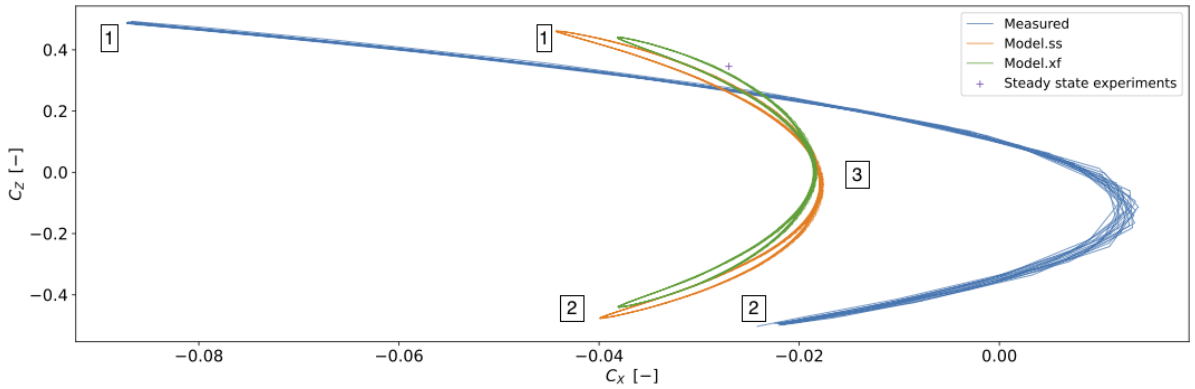

Figure 7.33: NACA 0012 T-foil ($AR = 5$) subjected to sinusoidal pitch C_Z vs. C_X at: $h/c = 1$, $\alpha_{imposed} = 8\cos(5t)$, $v_\infty = 5\ ms^{-1}$, $Re = 3.8 \cdot 10^5$

In the figures 7.30, 7.31, 7.32 and 7.33, the predicted difference between measured and predicted becomes visible. It becomes clear that some propulsive force is measured at negative C_Z. At higher values of C_Z very low values of C_X are measured.

For all figures 7.30, 7.31, 7.32 and 7.33, the turning point on the top-left (1) corresponds to the point where the $AoA = 8\ ^\circ$. The turning point on the bottom-left (2) corresponds to the turning point at $AoA = -8\ ^\circ$. For the predictions, the point of curvature on the middle-right (3) depicts the point of lowest drag and highest rate of angle change. Also, this is the point where the pressure side switches from bottom to top or top to bottom depending on the direction of the motion. The point of lowest drag lies lower in the measured signal this is only the point of lowest drag and lies lower in the figure. From previous analyses it is expected that this can be attributed to induced drag.

8 Behaviour of NACA 0012 T-foil in wave conditions

In this chapter the response of the NACA 0012 T-foil, parameterised in chapter 3, to waves is investigated. During the experiments the foil is moving at constant speed and is subjected to regular waves which are induced on the water by the wave maker. Figure 8.2 gives a schematic representation of the experimental setup. The response is compared to a similar prediction model as introduced in chapter 7 which compensates for the movements that are introduced to simulate dynamic behaviour. The prediction used in this chapter differs as the angle of attack and stream velocity are influenced by the incoming wave. The prediction method in waves will be explained in the first part of this chapter. In the second part of this chapter, the results from the experiments in waves are compared with the steady state prediction model.

8.1 Calculation in waves

This first part of the chapter focuses on calculations to predict the conditions in waves. Multiple calculation steps are made with the aim of making the steady state interpolation prediction. First, the measured wave is described by a wave function. This wave function is then used to calculate the particle velocity. With this particle velocity, the angle of attack and freestream velocity experienced by the foil are approximated. This data is used in the steady state interpolation function described in section 5.2.4. Similar to section 7.1.1, the force prediction is made in directions x and z.

8.1.1 Wave equation

The waves excited by the towing tank wavemaker have a sinusoidal character and can be described by the following cosine function:

$$Whm = \zeta_a \cos(\omega_{encounter}\, t + p) + c \tag{8.1}$$

A non-linear least squares fit was made for the encountering wave measured by the carriage and is depicted in figure 8.1 for one of the wave experiments.

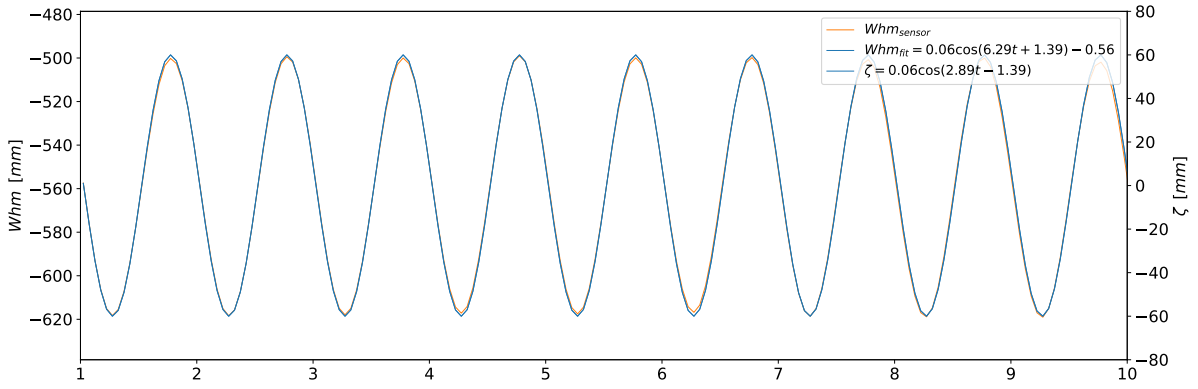

Figure 8.1: Non-linear least squares function fit of encountering wave by carriage at: $v_\infty = 4\ ms^{-1}$

In the legend of figure 8.1 both the fit in the form of equation 8.1 and the desired function for the wave ζ are depicted. The wave equation is calculated using the following methodology.

The found function, by the non-linear least squares fit, describes the encountering wave with respect to the carriage. The carriage is moving so the carriage velocity has to be implemented to find the actual equation for the wave height (ζ). The function of a wave 2.19, is rewritten so that ω can be written as a function of $\omega_{encounter}$, g and v_∞. For this $x_{carriage} = v_\infty \cdot t$ is used.

$$\zeta = \zeta_a \cos(k\,x - \omega\,t + p) = \zeta_a \cos k\,v_\infty\,t - \omega\,t = \zeta_a \cos((k\,v_\infty - \omega)\,t) \tag{8.2}$$

If equation 8.1 and 8.2 are compared, $\omega_{encounter}$ can be written as $kv - \omega$. Using the deep water dispersion relation (equation 2.20) the following steps can be made:

$$\omega_{encounter} = k\,v_\infty - \omega = \frac{\omega^2}{g}\,v_\infty - \omega \Rightarrow \frac{v_\infty}{g}\,\omega^2 - \omega - \omega_{encounter} = 0 \tag{8.3}$$

This equation can now be solved for ω:

$$\omega = \frac{1 \pm \sqrt{1 + 4\frac{v_\infty}{g}\,\omega_{encounter}}}{2\,\frac{v_\infty}{g}} \tag{8.4}$$

The phase shift p has to be implemented to compensate for the start of the measurement compared to the location of the wave. The offset c can be neglected since all the other variables of the foil are expressed with respect to the water surface which for a wave corresponds with $c = 0$.

8.1.2 Particle velocity

For the next step the particle velocities need to be calculated. It is necessary to rewrite the equations 2.22 and 2.23 using the phase shift p. The new equation for the particle velocity becomes:

$$u = \frac{\delta\phi}{\delta x} = \zeta_a\,\omega\,\frac{\cosh(k\,(h+z))}{\sinh(k\,h)}\cos((k\,x - \omega\,t) + p) \tag{8.5}$$

$$w = \frac{\delta\phi}{\delta z} = \zeta_a\,\omega\,\frac{\sinh(k\,(h+z))}{\sinh(k\,h)}\sin((k\,x - \omega\,t) + p) \tag{8.6}$$

8.1.3 Calculation h/c, AoA and v_f

Similar to the method discussed in section 6.1.1, the submergence, angle of attack and freestream velocity have to be calculated to make the static force compensation and predictions.

The submergence of the foil is measured by the wave height measurement sensor. The wave height calculated in section 8.1.1 is considered very accurate, therefore it is used together with the z-location of the foil to determine the submergence expressed in h/c which is calculated using the following equation:

$$h/c = -\frac{Z_{foil} + \zeta}{c} \tag{8.7}$$

The model remained in the same position, thus the compensation for motion can be neglected. Due to the motion of the particles in waves, another two components of velocity (u and w) were induced to the foil. A sketch was made showing the coordinate systems and direction of components because waves were moving in negative x direction.

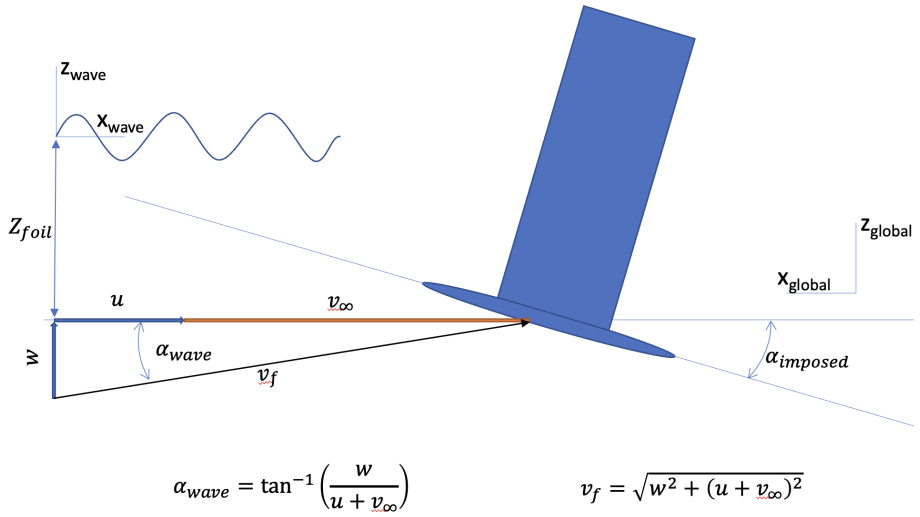

Figure 8.2: Calculation of v_f and α_{wave}

From the figure, the equations for α_{wave}, v_f and AoA can be derived. α_{wave} is derived using the law of tangents:

$$\alpha_{wave} = \tan^{-1}\left(w/(u+v_\infty)\right) \tag{8.8}$$

Using Pythagoras, v_f is derived from the schematic representation given in figure 8.2:

$$v_f = \sqrt{(w^2 + (u+v_\infty)^2)} \tag{8.9}$$

With α_{wave} and the imposed angle known, the AoA is calculated:

$$AoA = \alpha_{imposed} + \alpha_{wave} \tag{8.10}$$

8.1.4 Prediction using steady state interpolation model

Using the steady state interpolation function, described in section 5.2.4, the above gathered values for AoA, v_f and h/c are used to predict the lift and drag coefficient of the foil subjected to waves.

Similar to chapter 7, the force prediction is made in directions x and z. The lift and drag coefficient are expressed perpendicular and parallel to the freestream velocity respectively. Therefore the prediction for lift and drag requires rotation to the foil-global reference frame. This is done similarly to section 7.1.1, using the following equations:

$$C_{Z.model.ss} = \cos(\alpha_{wave})\, L_{model.ss}(h/c,\, AoA) \;+\; \sin(\alpha_{wave})\, D_{model.ss}(h/c,\, AoA) \tag{8.11}$$

$$C_{X.model.ss} = \sin(\alpha_{wave})\, L_{model.ss}(h/c,\, AoA) \;-\; \cos(\alpha_{wave})\, D_{model.ss}(h/c,\, AoA) \tag{8.12}$$

8.2 Wave Analyses

The measured forces are compared with the prediction using the theoretical model based on the steady state measurements. From the observations made in chapter 7, it is expected that higher absolute values for C_X are predicted in waves. Figures illustrating the dynamic effects are given for each changed variable. All tests were executed with $AoA = 5\,^\circ$ and $h/c = 1$. The parameters v_∞, ζ_a and ω were varied.

8.2.1 Variation of freestream velocity

This section gives a visual representation of the NACA 0012 T-foil responding to waves. In four figures, the response is presented for $v_\infty = 2\ ms^{-1}$ and $v_\infty = 6\ ms^{-1}$, $h/c = 1$ and $AoA = 5\,^\circ$. The measured force coefficient and force prediction are plotted alongside each other to make comparison possible.

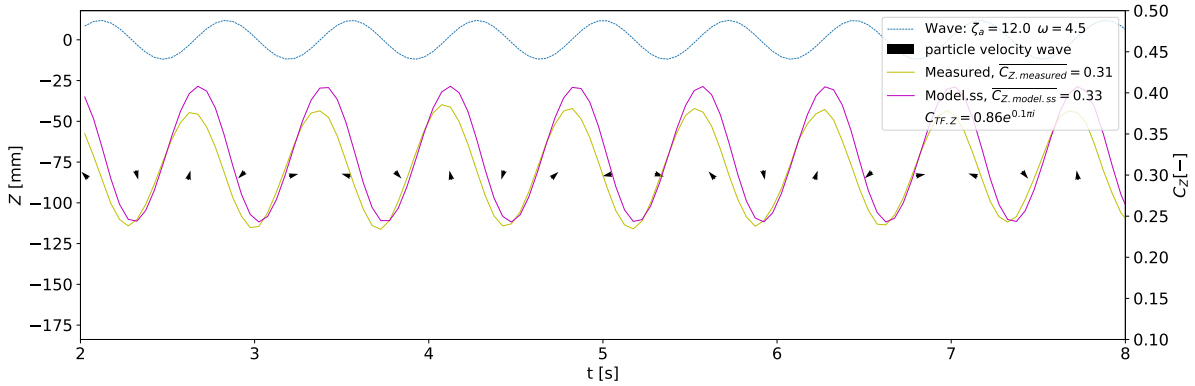

Figure 8.3: NACA 0012 T-foil ($AR = 5$) response in waves of $\zeta_a = 12\ mm$ and $\omega = 4.5$ at: $v_\infty = 2\ ms^{-1}$, $AoA = 5\,^\circ$, $h/c = 1$

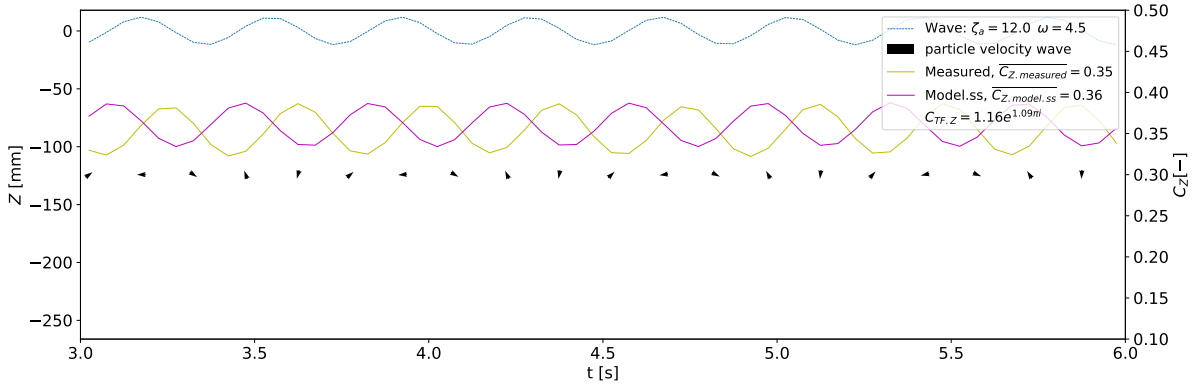

Figure 8.4: NACA 0012 T-foil ($AR = 5$) response in waves of $\zeta_a = 12\ mm$ and $\omega = 4.5$ at: $v_\infty = 6\ ms^{-1}$, $AoA = 5\,^\circ$, $h/c = 1$

The figures presented above, figure 8.3 and 8.4, show the foil response in z-direction where velocity is varied. Due to the increased velocity, a phase lag occurs. The increase in phase lag due to an increase in $v_\infty = 4\ ms^{-1}$, corresponds to half a period. For increasing velocity, the modulus has increased by 35%. It is expected that the phase lag occurs due to delayed wake vorticity because the encounter frequency has increased with the wave speed. As a result of the higher encounter frequency, troughs pass the foil at a higher rate giving the vortices no chance to interact with the surface this theory is endorsed by the video analyses in which the influence of the vorticity becomes visible when the trough has passed the foil. It can be noted that the lag, in this case, is remarkably large. From the perspective of the control system this would result in a self stabilising behaviour.

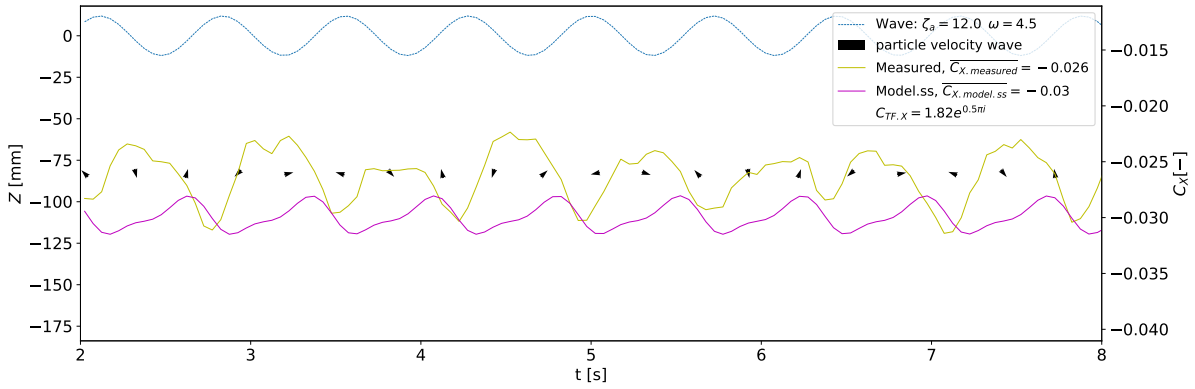

Figure 8.5: NACA 0012 T-foil ($AR = 5$) response in waves of $\zeta_a = 12\ mm$ and $\omega = 4.5$ at: $v_\infty = 2\ ms^{-1}$, $AoA = 5\ °$, $h/c = 1$

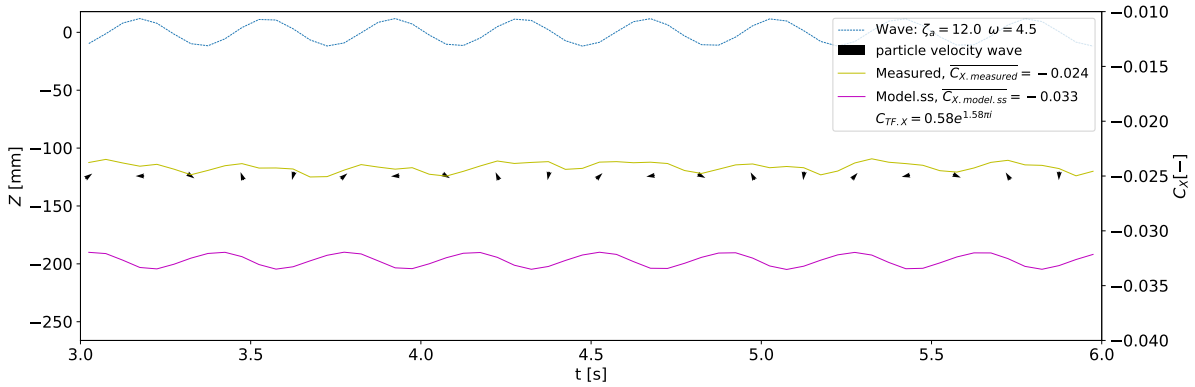

Figure 8.6: NACA 0012 T-foil ($AR = 5$) response in waves of $\zeta_a = 12\ mm$ and $\omega = 4.5$ at: $v_\infty = 6\ ms^{-1}$, $AoA = 5\ °$, $h/c = 1$

Figure 8.5 and 8.6 show the force in x-direction for the same experiments as depicted in figure 8.3 and 8.4. A similar phase lag of 1.1π can be distinguished for increasing velocity. While for C_Z the modulus increases with the velocity, the modulus for C_X has decreased with 68%. Also, the prediction of the coefficient in x-direction increased while the measured coefficient remained comparable. It is expected that the vector of freestream velocity increased such that the wave influence became less dominant.

8.2.2 Variation of wave height

In figures 8.7 and 8.8, wave height was varied. The freestream velocity and wave period remained constant at $v_\infty = 2\ ms^{-1}$ and $\omega = 4.5\ rads^{-1}$.

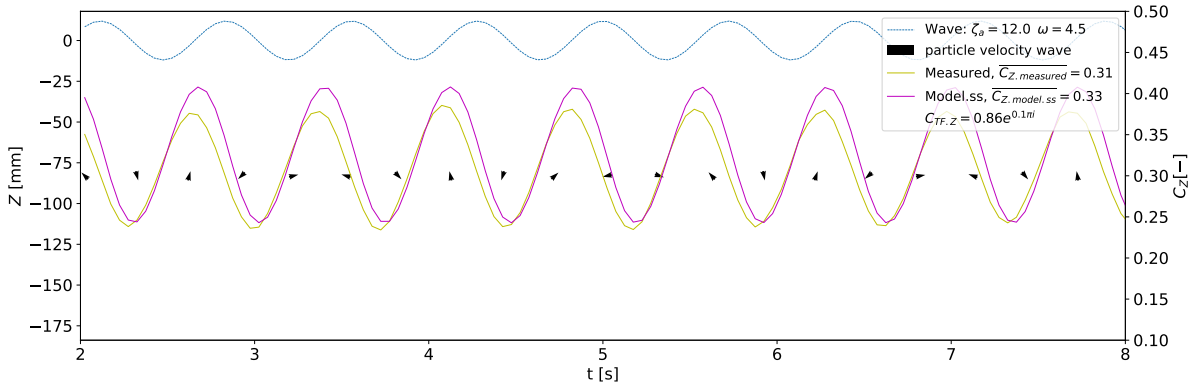

Figure 8.7: NACA 0012 T-foil ($AR = 5$) response in waves of $\zeta_a = 12\ mm$ and $\omega = 4.5$ at: $v_\infty = 2\ ms^{-1}$, $AoA = 5\ °$, $h/c = 1$

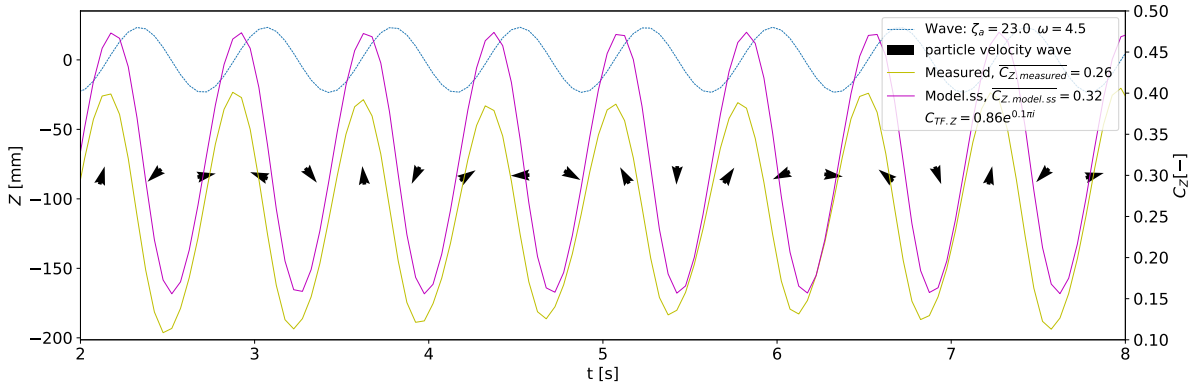

Figure 8.8: NACA 0012 T-foil ($AR = 5$) response in waves of $\zeta_a = 23\ mm$ and $\omega = 4.5$ at: $v_\infty = 2\ ms^{-1}$, $AoA = 5\ °$, $h/c = 1$

From figures 8.7 and 8.8, it can be concluded that with increasing wave height, the modulus remains and phase shift increase slightly while the overall predictions increase compared to the actual measurements. From equation 2.22 and 2.23, it can be concluded that the particle velocity in the wave increases linearly with the wave height. As a result, the fluctuations in the flow field increase. This is visualised in figure 8.8 where the size of the quiver increases compared to figure 8.7. It was concluded that a correction as function of wave height is required to make a correct prediction. For figure 8.7, this correction equals -0.02 while for figure 8.8 this correction equals -0.06. Lacking function, more data points are required.

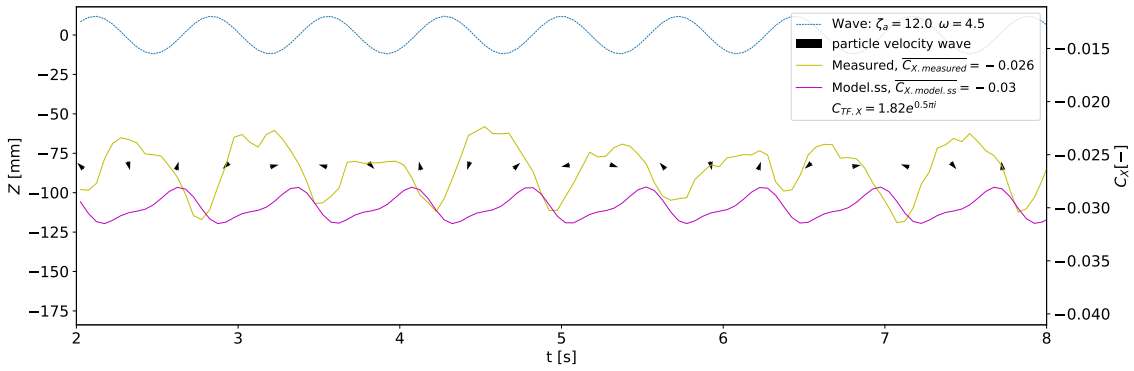

Figure 8.9: NACA 0012 T-foil ($AR = 5$) response in waves of $\zeta_a = 12\ mm$ and $\omega = 4.5$ at: $v_\infty = 2\ ms^{-1}$, $AoA = 5\ °$, $h/c = 1$

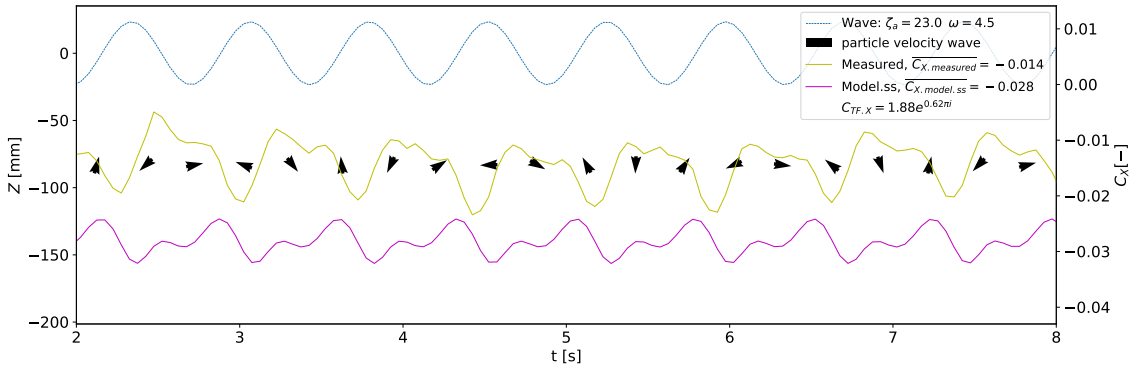

Figure 8.10: NACA 0012 T-foil ($AR = 5$) response in waves of $\zeta_a = 23\ mm$ and $\omega = 4.5$ at: $v_\infty = 2\ ms^{-1}$, $AoA = 5\ °$, $h/c = 1$

In the figures 8.9 and 8.10 the phase shift and modulus are comparable. The measured force in the negative x-direction decreased by 43%. Similar to the force in z-direction presented in figure 8.7 and 8.8, the prediction makes an over estimation of the force. This time a correction of $+0.04$ for $\zeta = 12$ and $+0.13$ for $\zeta = 23$ is required. An increase in waves can here be related to decreased drag on the hydrofoils. This is visualised in figure 8.11.

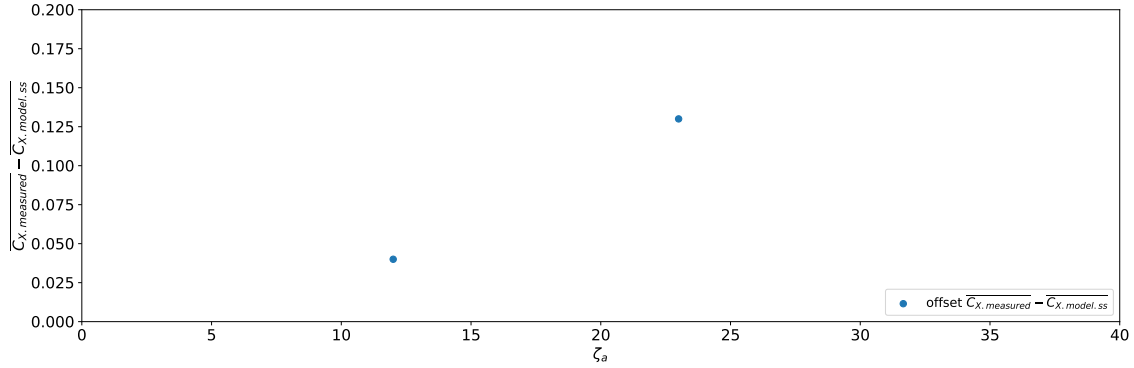

Figure 8.11: Distance between $\overline{C_{X.measured}} - \overline{C_{X.model.ss}}$ for various ζ_a

It is expected that the wake vorticity stabilises the behaviour because it does not get the opportunity to settle.

9 Conclusion

Research into the dynamic behaviour of T-foils broadens our comprehension of their performance in waves which will contribute to the innovation of their control systems. Improved control systems may result in increased passenger comfort, reduced drag and therefore an increase in fuel efficiency. Furthermore, these improvements have the potential to facilitate a more extensive application of hydrofoiling across the marine industry.

This research focuses on conducting experimental research into the hydrodynamic properties of a foil in dynamic conditions. The research question of this thesis is: How does the performance of a T-foil in steady state conditions compare to the performance of the same T-foil in dynamic conditions? To answer this question experimental research was conducted in the Towing tank at the TU Delft. A NACA 0012 T-foil was used which could be oriented within certain limits. Force and location were measured in 6 degrees. Even though, velocity and acceleration were calculated using the location data and gave good results, it is advised to use an accelerometer for future research. The mass of the setup measured by the load gauge was relatively heavy compared to the forces. It is therefore recommended to build the components of this section as light as possible, without compromising the stiffness. At last, it is recommended to use a different coordinate system. In this research, positive pitch corresponded with negative AoA and force in x-direction corresponded with negative drag. If the coordinate system is rotated, the simplicity of the calculations would increase.

First the hydrodynamic properties were determined by conducting experiments simulating steady state conditions. Combining all steady state experiments, the lift and drag coefficient on the foil were expressed as a function of angle of attack, and submergence for a certain Reynolds number. As a sidetrack, the performance of a RAW 3D printed foil was examined. It was found that due to the surface finish, the critical Reynolds number lies around $3.5 \cdot 10^5$ while for the finished foil, it is expected to be around $4.5 \cdot 10^5$. This results in different characteristics at higher velocity.

Before this study, research had been conducted into the effects of dynamic behaviour on the application of lifting surfaces. A need for further study into three dimensional oscillating foils was recognised and expected to demonstrate a phase shift and modulus change according to Von Karman theory. It was expected that the unsteady flow field would add a component to lift and drag for dynamic flow conditions, due to hysteresis effects of the vortices. Dynamic flow conditions were simulated in experiments where the setup was subjected to either: a sinusoidal motion in pitch direction, a sinusoidal motion in heave direction or waves.

While simulating dynamic conditions, the setup was subjected to motions. As a result of these motions, the static forces on the setup changed and inertial forces occurred. A function of static measurements, which were made before the steady state experiments, was made. Expressed as a function of AoA and h/c, it was used to compensate for the static forces on the setup which varied during a dynamic experiment. The inertial forces were compensated by applying the mass/inertia matrix M, which was composed by subjecting the setup to motions. During these motions the setup was lifted out of the water and thus free from hydrostatic and hydrodynamic forces.

From the steady state results a model was created which calculates a prediction of the hydrodynamic coefficients in x and z-direction (C_X and C_Z). It was decided to enrich the comparison with a prediction model using X-foil compensated for induced drag, finite foil and free surface effects because the steady state model is limited to $Re = 1.5 \cdot 10^5$. The compensation for free surface effect was created using the steady state data for $AoA = 5\ ^\circ$. According to Patterson & Binns (2021), the correction factor is constant for any AoA and Re. Therefore the decision was made to obtain the correction factor $K1$ as function of h/c only. The difference between the measurements and the steady state prediction model was valued using a transfer function. This function describes the difference by a modulus and a phase shift similar to Von Karman theory. This method can be applied as a consequence of the sinusoidal character of the dynamic experiments.

By comparing the measurements in sinusoidal heave with the steady state prediction model, it can be concluded that flow remains attached at higher angles. Experiments in dynamic conditions show no signs of separation while flow separation occurs at $\pm 12\ ^\circ$ in steady state conditions. Due to delayed wake vorticity, a lag of $0.02\pi\ rad$ can be distinguished between the measurements and the prediction of C_Z. The predictions in drag direction showed a 33% larger prediction than measurement. Also compared to the steady state measurements a decrease of 9% was noted.

Increased fluctuations at higher average lift were observed in sinusoidal pitching motions. For the drag, an additional component occurs. This additional component has a period equal to the subjected motion while the predicted C_X has a double period. It is expected that the additional component is caused by induced resistance because it has a period which equals the period of the imposed motion. Further investigation is recommended because this component has a very large influence on the drag in while pitching the foil. The steady state prediction model gives an accurate prediction of C_L during sinusoidal pitch. For future research, the model could be extended with a 4^{th} dimension namely Re. More data points or a numerical prediction of the influence of Re are required to do so.

When the freestream velocity is increased from 2 to 6 ms^{-1} in similar waves, it is found that the sinusoidal response of the hydrodynamic forces shifts by $\pm\pi$. Similar to sinusoidal heave, predictions show larger values for drag. A relation between wave height and this offset is found. When wave height is increased, the drag is reduced. It is expected that this is caused by free surface effects acting more severe in the throughs of the wave.

In addition to steady state experiments, an effort was made to describe the steady state behaviour of a T-foil using a novel method based on dynamic experiments. The new method included two angle sweeps, one positive and one negative. The rate of change proved to be sufficiently slow at $2/3\ ^\circ\ s^{-1}$ for $v_\infty = 2\ ms^{-1}$. This method was proven to be efficient, by producing reliable results while towing tank time could be reduced by 78%. It is expected that the rate of change has to be increased for experiments at higher freestream velocity. Future research would allow for a description of the rate of change as function of Reynolds number or freestream velocity.

During this research the possibility of using machine learning for developing a predictive control system arose. Machine learning approaches the problem of controlling the foil in a different way and is therefore a solution which could be further explored in future research. Machine learning can be split into three categories: supervised, unsupervised and reinforcement learning. Supervised and unsupervised learning use static datasets, making it non applicable. Reinforcement learning has the goal to find the best sequence of actions that will generate the outcome with the highest reward. It is expected that this can be applied to the control system.

References

Acker, D. (1999, april). Building the Bell-Baldwin Hydrofoil HD-4. *Model Ship Builder*, *188*, 41–50.

Ackroyd, J., & Riley, N. (2011). Hermann glauert frs, fraes (1892 - 1934). *Journal of Aeronautical History*, *1*, 22-73.

Acosta, A. (1973). Hydrofoils and hydrofoil craft. *Annual Review of Fluid Mechanics*, *5*(1), 161–184.

Acoustics, G. (n.d.). *Lab wave gauge.* Retrieved from `https://www.generalacoustics.com/products/lab-wave-gauge`

Alben, S., Witt, C., Baker, T., E., A., & Lauder, G. (2012). Dynamics of freely swimming flexible foils. *Physics of Fluids*, *24*(5).

Anderson, J. M., Streitlien, K., Barrett, D. S., & Triantafyllou, M. S. (1998). Oscillating foils of high propulsive efficiency. *Journal of Fluid Mechanics*, *360*, 41–72. doi: 10.1017/S0022112097008392

Ashworth Briggs, A., Binns, J., Duffy, J., & Fleming, A. (2018). *Free surface interaction of a 't-foil' hydrofoil* (Unpublished doctoral dissertation). University of Tasmania, Austalian Maritime College.

Binns, J., Brandner, P., & Plouhinec, J. (2008, 12). The effect of heel angle and free-surface proximity on the performance and strut wake of a moth sailing dinghy rudder t-foil. In (p. 121-129).

Borlenghi, C. (2020). *America's cup 2020.* Retrieved from `https://www.studioborlenghi.it`

Butterworth, S. (1930, october). On the theory of filter amplifiers. *Experimental wireless & the wireless engineer*.

Chapman, R. (1971). Spray drag of surface-piercing struts. *Naval undersea and development centre.*

Cleaver, D., Calderon, D., Wang, Z., & Gursul, I. (2016, july). Lift enhancement through flexibility of plunging wings at low reynolds numbers. *Journal of Fluids and Structures*, *64*.

Dewey, P., Boschitsch, B., Moored, K., Stone, H., & Smits, A. (2013). Scaling laws for the thrust production of flexible pitching panels. *Journal of Fluid Mechanics*, *732*.

Dobes, J., & Kozubková, M. (2014, 02). The influence of numerical models on determining the drag coefficient. *EPJ Web of Conferences*, *67*. doi: 10.1051/epjconf/20146702019

Drela, M. (1989). Xfoil: An analysis and design system for low reynolds number airfoils. In T. J. Mueller (Ed.), *Low reynolds number aerodynamics* (pp. 1–12). Berlin, Heidelberg: Springer Berlin Heidelberg.

Drela, M. (1998, july). MISES Implementation of Modified Abu-Ghannam/Shaw Transition Criterion. *MIT Aero-Astro.*

Euler, L. (1776). Formulae generales pro translatione quacunque corporum rigidorum. *Novi Commentarii academiae scientiarum Petropolitanae*, *20*, 189-207.

Gerritsma, J. (2015). *Hydromechanica 4 - golven* [Dictation].

Graig, W. (1974). Comment on" canadian advances in surface-piercing hydrofoils". *Journal of Hydronautics*, *8*(2), 74–76.

Helmbold, H. (1957). Theory of the finite-span blowing wing. *Journal of the Aeronautical Sciences*, *24*(5), 339–344.

Hoerner, S. (1965). *Fluid-dynamic drag: Practical information on aerodynamic drag and hydrodynamic resistance.* Hoerner Fluid Dynamics.

J.W. Chang, J., & Yoon, Y. (2015). Camber effects on the near wake of oscillating airfoils. *Journal of Aircraft*, *39*(4).

Kundu, P. K., Cohen, I. M., & Dowling, D. R. (2016). Chapter 14 - aerodynamics. In P. K. Kundu, I. M. Cohen, & D. R. Dowling (Eds.), *Fluid mechanics (sixth edition)* (Sixth Edition ed., p. 773-817). Boston: Academic Press. doi: https://doi.org/10.1016/B978-0-12-405935-1.00014-9

Lanchester, F. (1907). *Aerial flight: Part 1.* Aerodynamics.

Lorentz, G. G. (1953). *Bernstein polynomials.* University Press.

Monsonnec, F. (2014). The foil alphabet. *Foilers.*

Mueller, T., & Torres, G. (2004, may). Low aspect ratio aerodynamics at low reynolds numbers. *AIAA Journal*, *42*, 865–873.

Nava, J., Kosheleva, O., & Kreinovich, V. (2012). Why bernstein polynomials are better: Fuzzy-inspired justification. In *2012 ieee international conference on fuzzy systems* (p. 1-6). doi: 10.1109/FUZZ-IEEE.2012.6251341

Neilson Bonikowsky, L. (2009, 03). *Hydrofoil.* Retrieved from `https://www.thecanadianencyclopedia.ca/en/article/hydrofoil`

Patterson, N., & Binns, J. (2021). *Development of a six degree of freedom velocity prediction program for the foiling ac50 catamaran and ac75 monohull* (Unpublished doctoral dissertation). AMC University of Tasmania.

Prandtl, L. (1936). Theorie des flugzeugtragflügels im zusammendrückbaren medium. *Luftfahrtforsch*, *13*, 313.

Rawson, K., & Tupper, E. (2001). 10 - powering of ships: general principles. In K. Rawson & E. Tupper (Eds.), *Basic ship theory (fifth edition)* (Fifth Edition ed., p. 365-410). Oxford: Butterworth-Heinemann.

Savitzky, A., & Golay, M. J. E. (1964). Smoothing and differentiation of data by simplified least squares procedures. *Analytical Chemistry*, *36*(8), 1627-1639. doi: 10.1021/ac60214a047

Smith, A., & Gamberoni, N. (1956). Pressure gradient and stability theory. *Report no. ES*, *26388*.

Stapersma, D., Keuning, L., Frouws, J., & Grimmelius, H. (2000). *Design of advanced marine vehicles.* TU Delft.

Stokes, G. (1851, January). On the Effect of the Internal Friction of Fluids on the Motion of Pendulums. *Transactions of the Cambridge Philosophical Society*, *9*, 8.

Theodorsen, T., & Mutchler, W. H. (1935). *General theory of aerodynamic instability and the mechanism of flutter.* National Advisory Committee for Aeronautics.

Van Ingen, J. (n.d.). The en method for transition prediction. historical review of work at tu delft. In *38th fluid dynamics conference and exhibit* (p. 3830).

Von Karman, T., & Gabrielli, G. (1950). What price speed? specific power required for propulsion of vehicles. *Mechanical Engineering*, *72*, 775-781.

Wadlin, K., McGehee, J., & Shuford, C. (1952). *A theoretical and experimental investigation of the lift and drag characteristics of a hydrofoil at subcritical and supercritical speeds.* NACA.

Wadlin, K. L., Ramsen, J. A., & Mcgehee, J. R. (1950). Tank tests at subcavitation speeds of an aspect-ratio-10 hydrofoil with a single strut..

Wang, Y., Sun, X., Huang, D., & Zheng, Z. (2016). Numerical investigation on energy extraction of flapping hydrofoils with different series foil shapes. *Energy*, *112*.

Wu, X., Zhang, X., Tian, X., Li, X., & Lu, W. (2020). A review on fluid dynamics of flapping foils. *Ocean Engineering*, *195*, 106712.

Young, Y. L., Brizzolara, S., Binns, J., Brown, R., & Bose, N. (2013). Numerical and physical investigation of a surface-piercing hydrofoil. In *Third international symposium on marine propulsors smp* (Vol. 13, pp. 1–8).

A | Data X-foil

A.1 Dimensionless hydrodynamic properties for $Re = 0.5 \cdot 10^5$

AoA	C_l	C_d	N_{crit}	$Mach$
-8	-0.72	0.065	9	0
-7	-0.74	0.046	9	0
-6	-0.68	0.038	9	0
-5	-0.61	0.031	9	0
-4	-0.53	0.026	9	0
-3	-0.44	0.023	9	0
-2	-0.35	0.020	9	0
-1	0.02	0.022	9	0
0	0.0	0.021	9	0
1	-0.02	0.022	9	0
2	0.35	0.020	9	0
3	0.44	0.023	9	0
4	0.53	0.026	9	0
5	0.61	0.031	9	0
6	0.68	0.038	9	0
7	0.74	0.046	9	0
8	0.72	0.065	9	0

A.2 Dimensionless hydrodynamic properties for $Re = 1 \cdot 10^5$

AoA	C_l	C_d	N_{crit}	$Mach$
-12	-0.77	0.095	9	0
-11	-0.98	0.059	9	0
-10	-0.97	0.046	9	0
-9	-0.92	0.035	9	0
-8	-0.85	0.029	9	0
-7	-0.76	0.023	9	0
-6	-0.69	0.020	9	0
-5	-0.61	0.017	9	0
-4	-0.54	0.015	9	0
-3	-0.45	0.014	9	0
-2	-0.37	0.014	9	0
-1	-0.26	0.016	9	0
0	0	0.017	9	0
1	0.26	0.016	9	0
2	0.37	0.014	9	0
3	0.45	0.014	9	0
4	0.54	0.015	9	0
5	0.61	0.017	9	0
6	0.69	0.020	9	0
7	0.76	0.023	9	0
8	0.85	0.029	9	0
9	0.92	0.035	9	0
10	0.97	0.046	9	0
11	0.98	0.059	9	0
12	0.77	0.095	9	0

A.3 Dimensionless hydrodynamic properties $Re = 2 \cdot 10^5$

AoA	C_l	C_d	N_{crit}	$Mach$
-14	-0.96	0.080	9	0
-13	-1.06	0.056	9	0
-12	-1.11	0.044	9	0
-11	-1.07	0.036	9	0
-10	-1.07	0.030	9	0
-9	-0.93	0.025	9	0
-8	-0.85	0.021	9	0
-7	-0.77	0.018	9	0
-6	-0.70	0.015	9	0
-5	-0.62	0.013	9	0
-4	-0.54	0.012	9	0
-3	-0.45	0.011	9	0
-2	-0.31	0.011	9	0
-1	-0.15	0.010	9	0
0	0	0.010	9	0
1	0.15	0.010	9	0
2	0.31	0.011	9	0
3	0.45	0.011	9	0
4	0.54	0.012	9	0
5	0.62	0.013	9	0
6	0.70	0.015	9	0
7	0.77	0.018	9	0
8	0.85	0.021	9	0
9	0.93	0.025	9	0
10	1.01	0.030	9	0
11	1.07	0.036	9	0
12	1.11	0.044	9	0
13	1.06	0.056	9	0
14	0.96	0.080	9	0

A.4 Dimensionless hydrodynamic properties for $Re = 5 \cdot 10^5$

AoA	C_l	C_d	N_{crit}	$Mach$
-14	-1.23	0.038	9	0
-13	-1.21	0.031	9	0
-12	-1.17	0.026	9	0
-11	-1.11	0.023	9	0
-10	-1.04	0.020	9	0
-9	-0.96	0.017	9	0
-8	-0.89	0.015	9	0
-7	-0.80	0.013	9	0
-6	-0.72	0.012	9	0
-5	-0.63	0.010	9	0
-4	-0.48	0.009	9	0
-3	-0.33	0.008	9	0
-2	-0.21	0.007	9	0
-1	-0.10	0.006	9	0
0	0	0.006	9	0
1	0.10	0.006	9	0
2	0.21	0.007	9	0
3	0.33	0.008	9	0
4	0.48	0.009	9	0
5	0.63	0.010	9	0
6	0.72	0.012	9	0
7	0.80	0.013	9	0
8	0.89	0.015	9	0
9	0.96	0.017	9	0
10	1.04	0.020	9	0
11	1.11	0.023	9	0
12	1.18	0.026	9	0
13	1.21	0.031	9	0
14	1.23	0.038	9	0

A.5 Dimensionless hydrodynamic properties for $Re = 10 \cdot 10^5$

AoA	C_l	C_d	N_{crit}	$Mach$
-19	-1.44	0.080	9	0
-18	-1.55	0.048	9	0
-17	-1.56	0.035	9	0
-16	-1.55	0.028	9	0
-15	-1.50	0.024	9	0
-14	-1.45	0.021	9	0
-13	-1.38	0.019	9	0
-12	-1.29	0.017	9	0
-11	-1.20	0.015	9	0
-10	-1.10	0.014	9	0
-9	-1.01	0.012	9	0
-8	-0.92	0.011	9	0
-7	-0.84	0.011	9	0
-6	-0.70	0.010	9	0
-5	-0.56	0.009	9	0
-4	-0.43	0.008	9	0
-3	-0.32	0.008	9	0
-2	-0.21	0.007	9	0
-1	-0.10	0.007	9	0
0	0.0	0.007	9	0
1	0.10	0.007	9	0
2	0.21	0.007	9	0
3	0.32	0.008	9	0
4	0.43	0.008	9	0
5	0.56	0.009	9	0
6	0.70	0.010	9	0
7	0.84	0.011	9	0
8	0.92	0.011	9	0
9	1.01	0.012	9	0
10	1.10	0.014	9	0
11	1.20	0.015	9	0
12	1.29	0.017	9	0
13	1.38	0.019	9	0
14	1.45	0.021	9	0
15	1.50	0.024	9	0
16	1.55	0.028	9	0
17	1.56	0.035	9	0
18	1.55	0.048	9	0
19	1.44	0.080	9	0

B | Inertia analyses

B.1 Inertia analyses x-direction

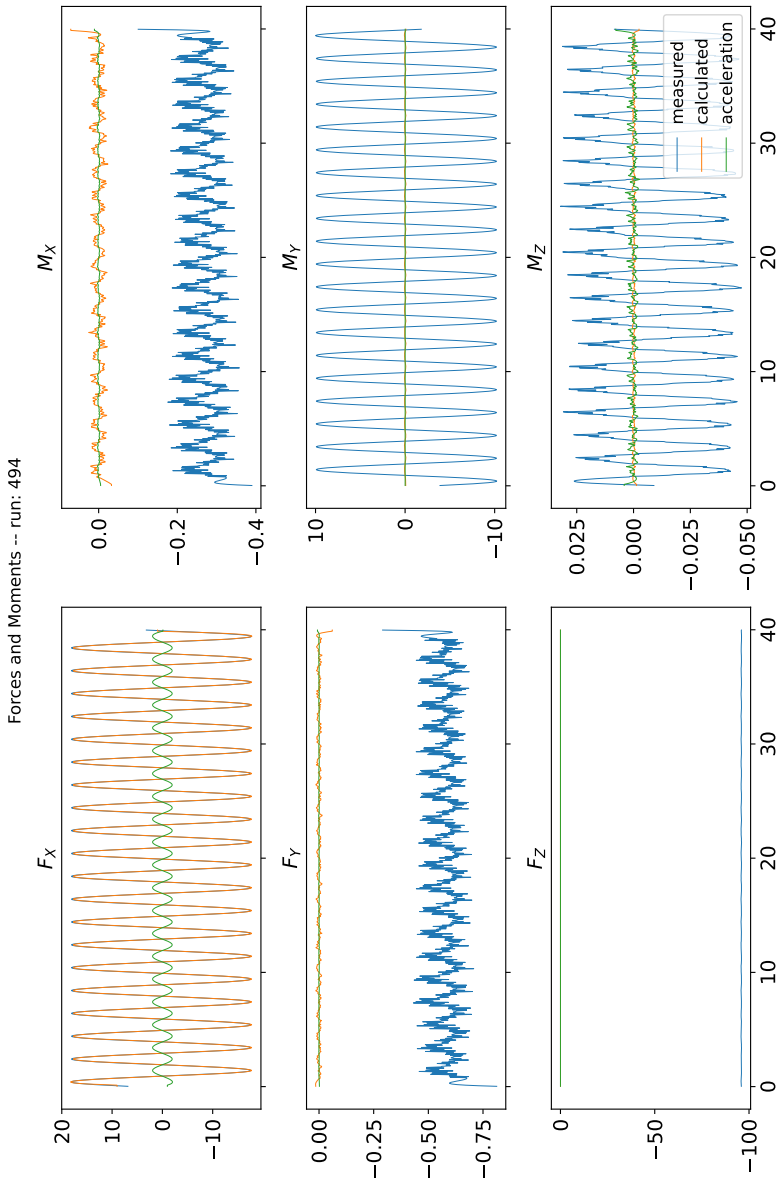

B.2 Inertia analyses y-direction

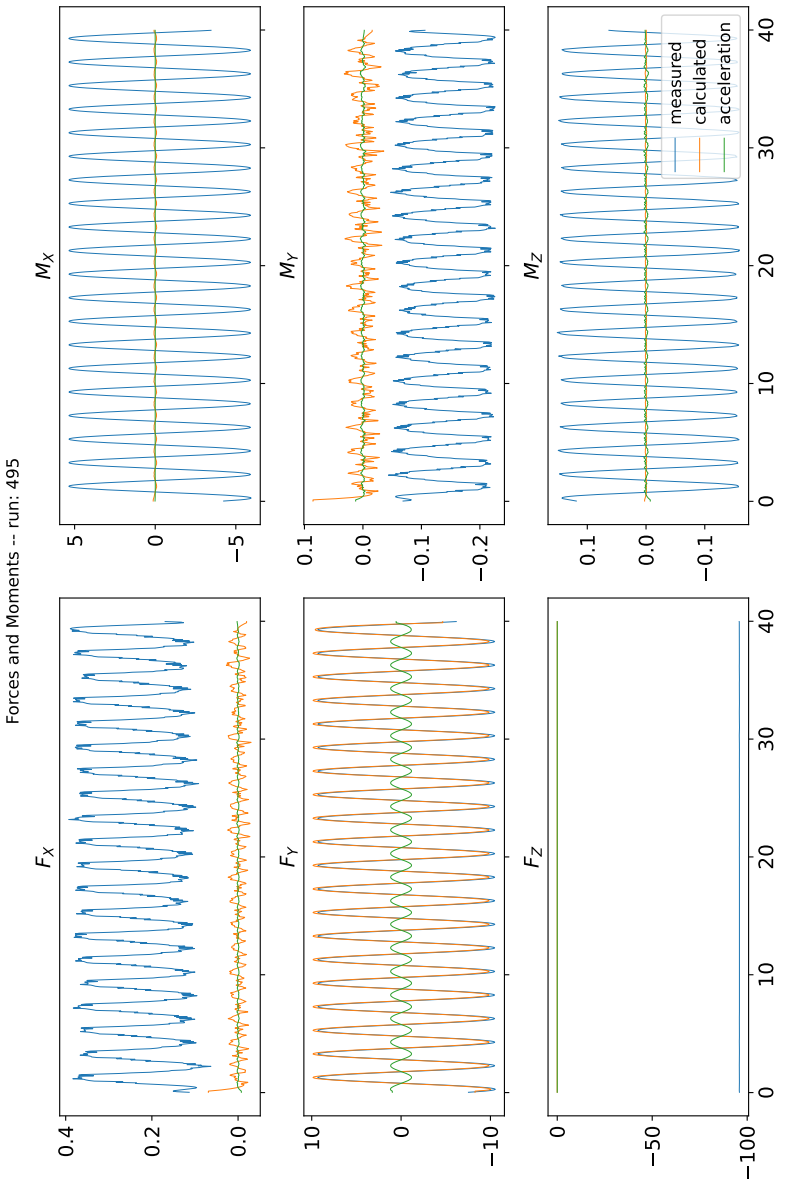

B.3 Inertia analyses z-direction

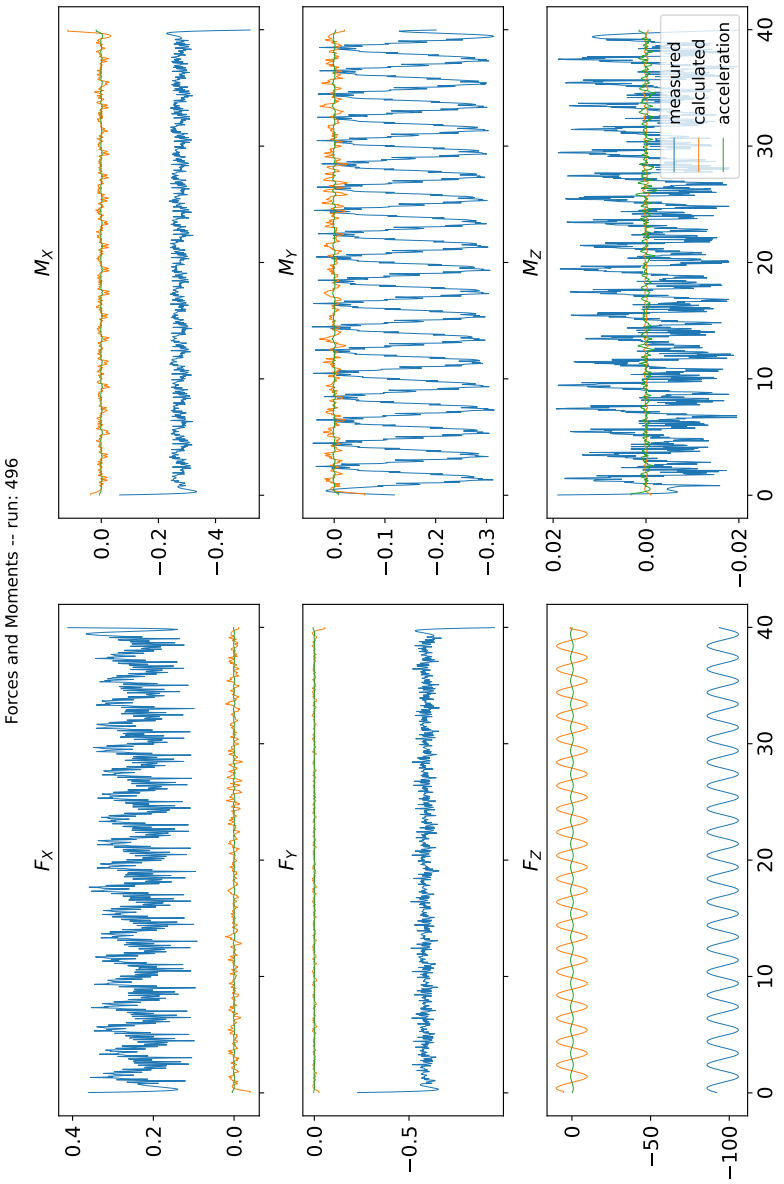

B.4 Inertia analyses roll-direction

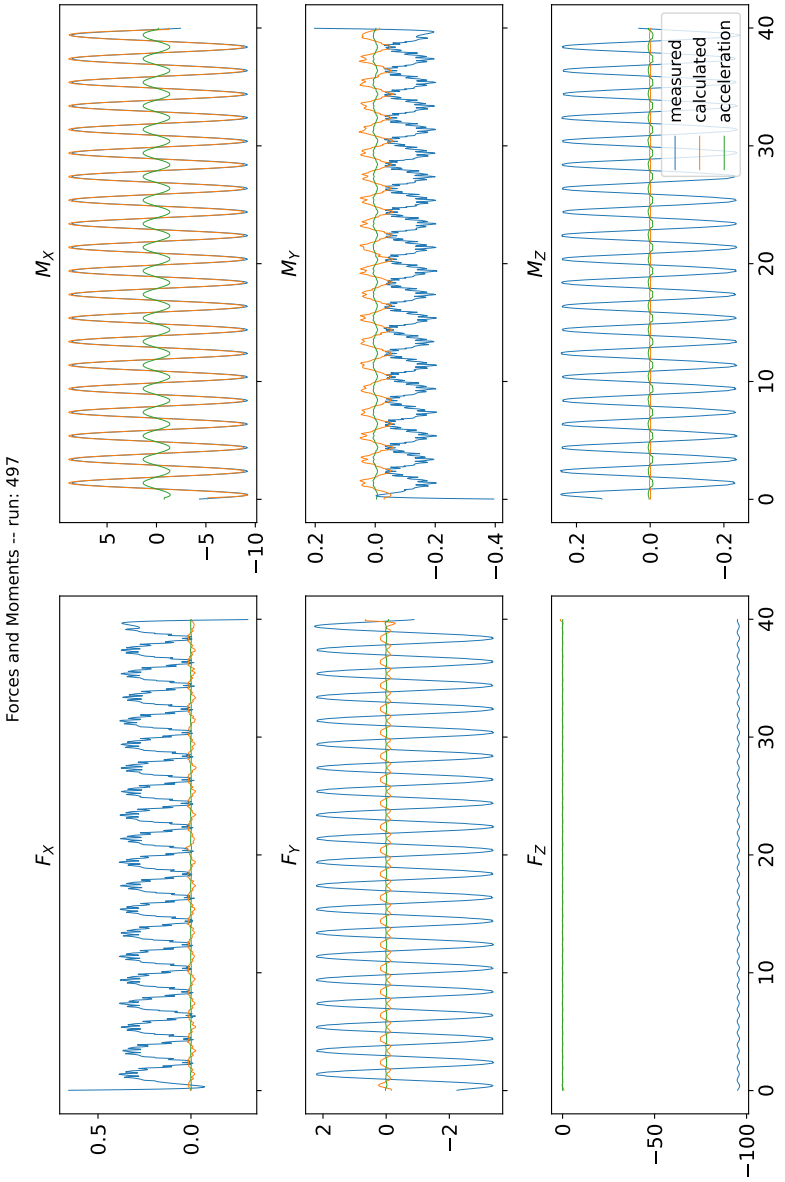

B.5 Inertia analyses pitch-direction

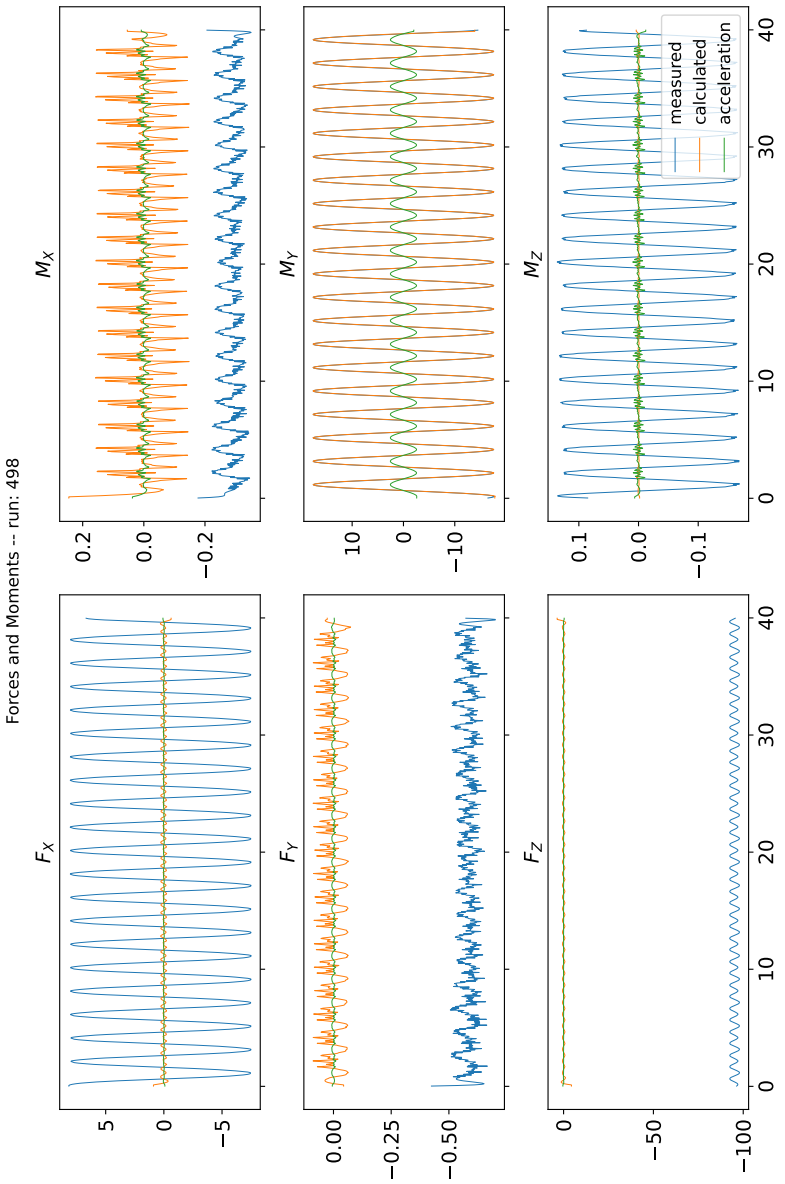

B.6 Inertia analyses yaw-direction

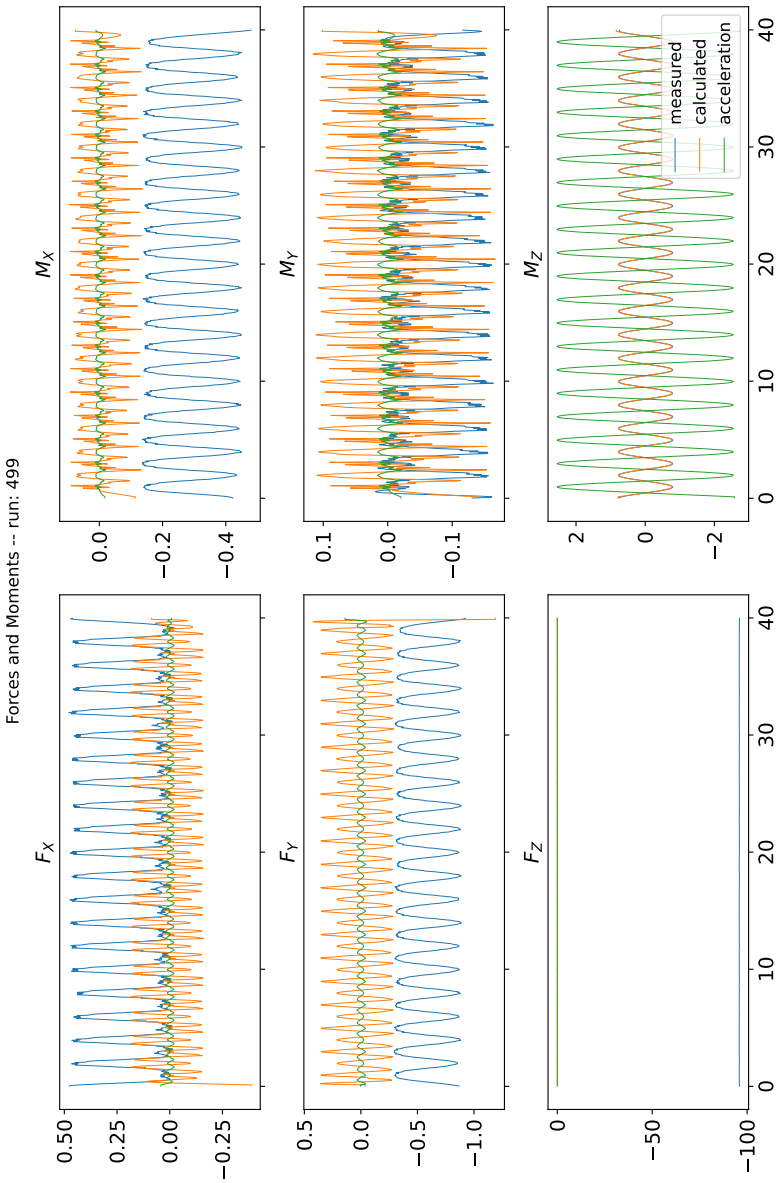

C | Test matrix

Supplementary Data File Description:

The accompanying Excel spreadsheet shows the test matrix of the experiments. The first tab named "overview" shows the properties of the foil. The second tab shows actual test matrix. In this test matrix estimations of the forces are made using the settings of the experiments. To make these predictions, tab "X-foil" is required to extract the foil characteristics which are produced by X-foil.

Filename:

"Test matrix T-foil characterisation_v4.xls"

D | Python code and supplementary files

Supplementary Python code for all calculations and supplementary files:

The calculations in this study were run in Python. the code used is added in the files in this appendix. The code is split in separate files and listed in the table below. A second list is providing the supplementary files used by the code.

Python code files:

filename	description
"everything.py"	Script to run all python script subsequently
"cfg2netcdf.py"	Script to interpret the raw data
"correct_raw.py"	Script to make measurement specific corrections
"raw2filter.py"	Script to filter the raw data
"filter2pdf.py"	Script to make a pdf of all filtered time traces
"filter2foil.py"	Script to translate all filtered data to foil reference frame
"foil2pdf.py"	Script to make a pdf of all filtered and translated time traces
"foil2mass.py"	Script to determine the mass inertia matrix
"foil2nulfunc.py"	Script to determine static forces on the setup
"foil2ss.py"	Script to calculate steady state results
"foil2ssfunc.py"	Script to determine the function of steady state measurements
"ss2pdf.py"	Script to make a pdf of all steady state results
"foil2dynamic.py"	Script to calculate dynamic results
"dynamic2pdf.py"	Script to make a pdf of all dynamic results
"foil2waves.py"	Script to calculate results in wave conditions
"waves2pdf.py"	Script to make a pdf of all wave conditions

Supplementary files:

filename	description
"rundata.xlsx"	Run specific parameters and settings
"Xfoil.csv"	Data file containing all X-foil data

The measurement data can be made available upon requested by the TU Delft Towing Tank

E | Overview of documents with graphs

Supplementary figures from all experiments and calculations:

Not all figures were used in the content of this research to guarantee readability. All figures that were created in the process of this study can be found in this appendix.

filename	description
"202104_filter.pdf"	contains all filtered signals
"202104_foil.pdf"	contains all time traces in foil reference frame
"202104_mass.pdf"	contains all figures of inertia experiments
"202104_nulfunc.pdf"	contains the function fit of all static measurements
"202104_ss.pdf"	contains all figures of steady state experiments
"202104_dynamic.pdf"	contains all figures from dynamic experiments except waves
"202104_waves.pdf"	contains all figures from wave experiments